Diss. ETH No. 16362

Numerical and Experimental Study of Flame Propagation and Knock in a Compressed Natural Gas Engine

Christian Lämmle

2005

Diss. ETH No. 16362

Numerical and Experimental Study of Flame Propagation and Knock in a Compressed Natural Gas Engine

A dissertation submitted to the
SWISS FEDERAL INSTITUTE OF TECHNOLOGY ZURICH

for the degree of
Doctor of Technical Sciences

presented by
CHRISTIAN LÄMMLE
Dipl. Masch.-Ing. ETH

born November 21, 1974
citizen of Russikon, ZH and St. Gallen-Rotmonten, SG

accepted on the recommendation of
Prof. Dr. K. Boulouchos, examiner
Prof. Dr. U. Spicher, co-examiner

2005

Prediction is very difficult, especially about the future.
Niels Bohr

To my family

Preface

Abstract

One of the major objectives during the development process of new products is to reduce costs and time to market. Increasing computational power and continuous improvements of models for internal combustion engine applications show promise with respect to replacement of some optimisation steps by computer simulations. A prerequisite for such a substitution is that trends can be reasonably predicted and that calculations adequately incorporate the physics.

The flame propagation and the knock behaviour of compressed natural gas engines have been studied in the present work. The aim is to improve the physical understanding on one hand and to develop physically based models for cycle simulation tools on the other hand. These models have been used to optimise a new engine concept which combines ultra-low emissions, high efficiency and driveability.

An empirical combustion model based on experimentally determined burn rate curves has been developed to predict the engine behaviour for a wide range of operating conditions. It was found that global qualitative trends can be predicted quite well. Some relevant parameters characterising the combustion process - the crank angle at 5% burned, the crank angle at 50% burned and the burn duration defined as 5% to 90% burned - have been computed and compared with experimental data. The limitations of such a model have been shown by evaluating this model for a different combustion chamber geometry and various operating conditions.

Therefore, a new model based on physical formulations has been developed. The phenomenological combustion model dedicated to compressed natural gas engines developed in this work can be used for projections and additionally to support the understanding of experimental results. A characteristic mean flame front area has been defined by applying some submodels describing the laminar flame speed, the turbulent flame speed and the turbulence intensity. Furthermore, the expansion factor describing the flame propagation due to the ratio of the densities of burned and unburned mixture has been considered. Good agreements between experimental data and computed results have been observed by applying this model

to a different combustion chamber geometry. The characteristic mean flame front area was redefined for these new geometrical properties. It was shown, that the new flame front area can be approximated based on considerations concerning flame propagation and based on the known mean flame front area.

Research and development activities often focus on increasing the efficiency of spark ignited engines, but many modifications leading to higher engine efficiency in part load operation lead to higher risk of knock occurrence at full load operation. These contradictory requirements clearly indicate the necessity of accurate physical formulations of the knock phenomena. The model developed in this work is based on a one step chemistry approach leading to the so called knock integral method. Due to the varying gas composition of compressed natural gas five well-defined compositions of synthetic gases have been tested to investigate the influence of the individual components. Furthermore, the model considers different operating conditions of an engine meaning that intake pressure, intake temperature, engine speed and spark timing have been varied. The differentiation between non-knocking and knocking combustion has been found to be a key factor for the quality of the model and has been thoroughly investigated. The widely used analysis of the maximum amplitudes of the pressure oscillations has been replaced by the analysis of the burn rate, where a new knock detection method has been developed. A clearly defined initiation of knocking combustion was observed. The parameters of the knock model determined finally can adequately describe the dependencies on the gas composition.

Zusammenfassung

Eines der Hauptziele beim Entwicklungsprozess von neuen Produkten ist die Reduktion der Kosten und der Entwicklungszeit. Die zunehmende Leistungsfähigkeit moderner Prozessoren und die kontinuierliche Weiterentwicklung bestehender Modelle für Verbrennungsmotoren erlauben es, einzelne Entwicklungsschritte durch Computersimulationen zu ersetzen. Eine Voraussetzung dafür ist aber, dass Trends vernünftig vorausgesagt werden können und dass Berechnungen die Physik adäquat wiedergeben.

In der vorliegenden Arbeit wurden die Verbrennung und das Klopfverhalten bei Gasmotoren untersucht. Dadurch sollen einerseits das physikalische Verständnis verbessert und andererseits Modelle für den Einsatz in thermodynamischen Prozessrechenpaketen entwickelt werden. Diese Modelle wurden erfolgreich für die Optimierung eines neuen Motorkonzeptes eingesetzt, das niedrigste Emissionen, einen hohen Wirkungsgrad und gute Fahrbarkeit vereint.

Basierend auf experimentell bestimmten Brennverläufen wurde ein empirisches Verbrennungsmodell entwickelt, um das Betriebsverhalten des Motors für verschiedene Betriebspunkte vorauszusagen. Es wurde beobachtet, dass globale, qualitative Trends gut vorausgesagt werden können. Einige charakteristische Parameter des Verbrennungsprozesses - der Kurbelwinkel bei 5% umgesetzter Brennstoffmasse, der Kurbelwinkel bei 50% umgesetzter Brennstoffmasse sowie die Brenndauer definiert als 5% bis 90% umgesetzter Brennstoffmasse - wurden berechnet und mit experimentellen Daten verglichen. Die Grenzen des empirischen Verbrennungsmodells wurden bei der Übertragung auf eine andere Brennraumgeometrie und diverse Betriebsbedingungen aufgezeigt.

Deshalb wurde ein neues Modell entwickelt, das auf physikalischen Formulierungen basiert. Das für Gasmotoren entwickelte phänomenologische Verbrennungsmodell kann für die Vorausberechnung verwendet werden und unterstützte zudem die Interpretation von experimentellen Ergebnissen. Eine charakteristische gemittelte Flammfrontfläche wurde unter Verwendung von Untermodellen definiert. Diese Untermodelle beschreiben die laminare Flamm-

geschwindigkeit, die turbulente Flammgeschwindigkeit sowie die Turbulenzintensität. Des Weiteren wurde der Expansionsfaktor, der die Flammausbreitung aufgrund des Verhältnisses der Dichten von verbranntem und unverbranntem Gemisch beschreibt, berücksichtigt. Es konnte eine gute Übereinstimmung von experimentellen Daten und Berechnungen unter Verwendung dieses Modelles für andere Brennraumgeometrien beobachtet werden. Die charakteristische gemittelte Flammfronfläche wurde für die neuen geometrischen Verhältnisse angepasst. Es konnte jedoch gezeigt werden, dass die neue Flammfrontfläche durch Überlegungen zur Flammausbreitung basierend auf der ursprünglichen Flammfrontfläche approximiert werden kann.

In der Forschung und Entwicklung wird häufig auf die Verbesserung des Wirkungsgrades im Teillastbetrieb bei Ottomotoren fokussiert, wobei Modifikationen, die zu einer Verbesserung des Wirkungsgrades bei Teillast führen, das Klopfrisiko beim Volllastbetrieb erhöhen können. Diese gegenläufigen Anforderungen zeigen eindeutig, dass präzise physikalische Beschreibungen des Klopfphänomens nötig sind. Das in dieser Arbeit entwickelte Modell basiert auf einem Ein-Schritt-Chemie Ansatz und führt zum so genannten Klopfintegral. Aufgrund der variierenden Zusammensetzung von Erdgas wurden fünf exakt definierte synthetische Gasgemische getestet, um den Einfluss der einzelnen Komponenten zu untersuchen. Des Weiteren berücksichtigt das Modell verschiedene Betriebsbedingungen eines Verbrennungsmotors, wobei der Einlassdruck, die Einlasstemperatur, die Drehzahl und der Zündwinkel verändert wurden. Es wurde beobachtet, dass die Unterscheidung zwischen klopfender und nicht klopfender Verbrennung ein Schlüsselfaktor für die Qualität des Modells darstellt, weshalb diese Unterscheidung gründlich untersucht wurde. Die häufig verwendete Analyse der Druckamplituden wurde durch eine Analyse des Brennverlaufs ersetzt, wobei eine neue Klopfdetektionsmethode entwickelt wurde. Ein eindeutig definierter Klopfbeginn konnte dadurch beobachtet werden. Die schlussendlich gefundenen Parameter des Klopfmodells beschreiben die Abhängigkeiten von den Einzelkomponenten adäquat.

Table of Contents

4 Study of Knock Behaviour and Knock Model Approach 79

5 Summary and Conclusions 135

6 References 139

Chapter 1

Introduction

One of the major challenges for the future will be to reduce global emissions and crude oil consumption. All industries have to contribute to minimise emissions and to use energy more efficient. For transportation binding emission standards have been introduced in 1974 in Europe and agreements have been made to reduce CO_2 emissions between public authorities and car manufacturers [1] and between public authorities and importers [8] some years ago. The European Automobile Manufacturers Association ACEA defined $140gCO_2$/km as target in 2008, while the average specific emissions achieved $165gCO_2$/km in 2002. In Switzerland the association of the importers agreed in February 2002 to reduce fuel consumption by about 3% per year to 6.4 litres/100km in 2008 based on the year 2000 where the average fuel consumption was 8.4 litres/100km.

Increasing safety, performance and comfort demands leaded to larger and heavier passenger cars. From 1995 to 2002 the average weight of the vehicles in Europe increased by 10% and the mean power increased by 22 % [1]. In the mean time average CO_2 emissions decreased by 12%.

Furthermore, investigations of the mobility behaviour [96] for various countries show an increasing share in final energy for transportation with increasing incoming. Taking Switzerland as an example, the car fleet at the end of 2004 achieved 3.8 Mio. passenger cars by a population of 7.4 Mio.

These customer wishes are in contrast to the environmental compatibility and contrary to the political efforts to reduce fuel consumption. Therefore, new engine concepts are necessary. Actual research and development activities focus on exhaust gas aftertreatment to reduce NOx emissions and particulate matters for diesel engines what will lead in increasing fuel consumption. For gasoline engines the objectives will mainly be to increase the efficiency and to further develop 3-way-catalyst technology.

New engine technologies like direct injected gasoline engines and hybrids have been launched during the last years.

A promising way to reduce CO_2 emissions is to use Compressed Natural Gas (CNG) as fuel. The compressed natural gas vehicle has a high potential for improvement of air quality and for significant reductions in CO_2 emissions. Compared to gasoline engines CO_2 emissions are reduced by 25% if the efficiency is assumed to be equal. Due to its high knock resistance CNG engines offer the possibility for continuous optimisations. The fuel scenario of the European Commission until 2020 [2] includes the promotion of natural gas for transportation. Furthermore, compressed natural gas will help to reduce the dependence on crude oil.

1.1   Technology and Actual Market Situation for CNG Passenger Cars

All car manufacturers have launched CNG cars during the last five years. In general, CNG engines work similar to gasoline engines. Nowadays, there are two groups of natural gas vehicles, where it can be distinguished by the degree of optimisation.

Bi-Fuel vehicles are equipped with a gasoline and a CNG fuel injection system and have the capability to drive with both fuels. These cars have two engine control units and do not fully take advantage of the knock resistance of compressed natural gas, meaning that CO_2-reductions of about 22% for most vehicles on the market can be achieved. The cruising range in gasoline operation is equal to a gasoline vehicle and additionally about 250 to 450km in CNG operation.

Monovalent CNG vehicles have an engine optimised for CNG operation and in maximum a 15 litres gasoline fuel tank, whereas the gasoline operation is only in case of emergency. The cruising range is lower for the monovalent CNG cars and the potential to reduce CO_2 emission is higher than for Bi-Fuel vehicles.

The gas is stored in bottles with 200bar and a pressure reduction valve, which must be heated with the engine water, is used to ensure 8.3bar in the fuel rail. Multipoint injection is used, where the injectors have a larger nozzle diameter compared to gasoline injectors. All of the production engines are port injected.

The software of the engine control unit has to be adjusted for CNG operation. The partial pressure of CNG in the intake manifold and the pressure and temperature

of the gaseous fuel in the rail have to be taken into account to ensure the correct calculation of the fuel mass to be injected for the pilot control. Due to the different combustion behaviour compared to gasoline engines several maps have to be adapted for CNG operation.

The reliability of the components and technologies used for CNG vehicles has been demonstrated during the last few years. A key factor for the market penetration is the availability of fuelling stations. The following figure gives an overview of the CNG fuelling stations installed in some selected countries:
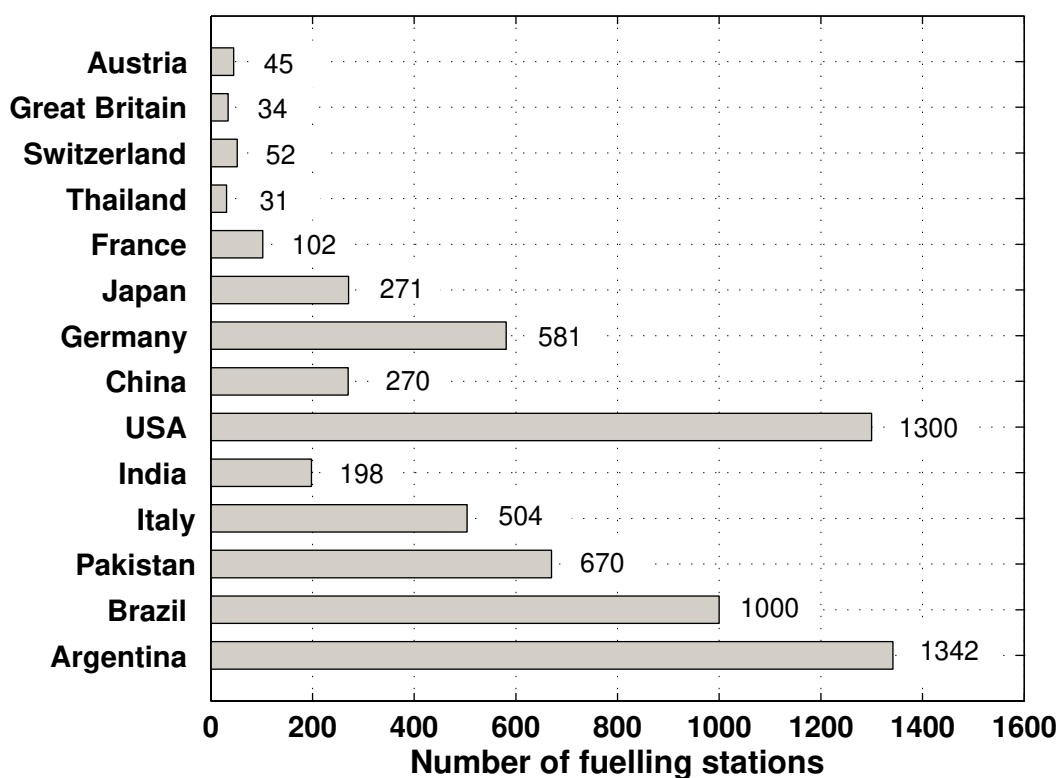
Figure 1.1: Worldwide CNG fuelling stations in some selected countries (source: International Association for Natural Gas Vehicles IANGV, June 2005)

The number of CNG fuelling stations is still much lower compared to gasoline. Associations are founded to enhance CNG availability which is necessary to increase market share of CNG vehicles.

Figure 1.2 shows the car fleet in several countries. The numbers include both OEM and converted NGVs. In Western Europe, except Italy, only a few cars are fuelled with CNG, where a lot of CNG vehicles can be found in South America.
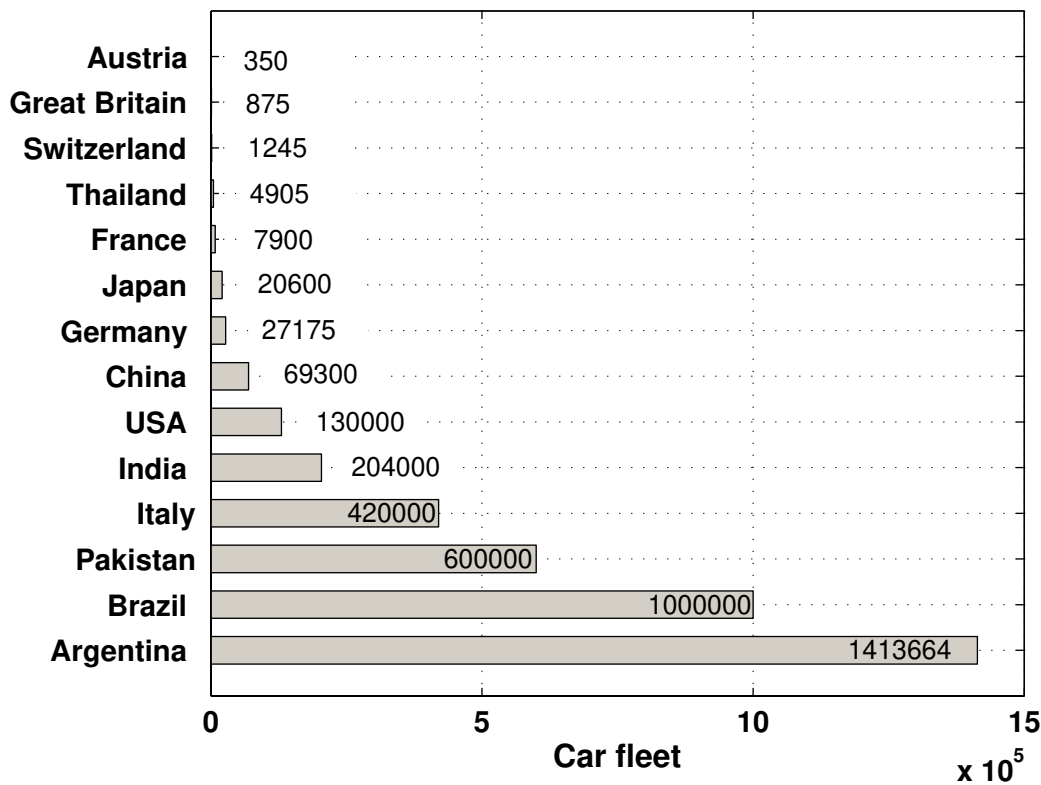
Figure 1.2: Worldwide car fleet in some selected countries (source: International Association for Natural Gas Vehicles IANGV, June 2005)

To support the technical progress and to sensitise people to the possibilities of CNG cars the Clean Engine Vehicle project (see chapter 1.2) was started. The aim of the Clean Engine Vehicle (CEV) project [9] was to demonstrate the potential of a monovalent Compressed Natural Gas vehicle.

1.2   The Clean Engine Vehicle Project

The development process started with the 1.0-litre production engine fuelled with gasoline in may 2000. The engine specifications are described in chapter 2. Several modifications were carried out to use CNG as fuel, to reduce fuel consumption and tail pipe emissions. In November 2003, a prototype based on the Volkswagen Polo (model year 2000) fulfilling the ambitious objectives was presented.

The objectives can be summarised as follows. The CO_2 emissions had to be reduced by 30% in monovalent CNG operation compared to the Volkswagen Polo (model year 2000) with 1.4-litre, 44kW gasoline engine. The NEDC (New European Driving Cycle) was chosen to compare CO_2 emissions. Furthermore, the CEV had to fulfil the European Euro 4 in the NEDC and the Californian Super-Ultra-Low-Emission-Vehicles (SULEV) emission standards in the FTP-75 cycle.

This project was a collaboration among the Swiss Federal Laboratories for Materials Testing and Research (EMPA) in Dübendorf and the The Swiss Federal Institute of Technology (ETH) in Zurich. The Internal Combustion Engines Laboratory at EMPA was the project leader, made the entire tests on the roller test bench and on the engine dyno, investigated different catalyst converters and built up the prototype. The Aerothermochemistry and Combustion Systems Laboratory LAV at ETH was responsible for the optimisation of the thermodynamic system and together with EMPA for the implementation on the engine. The Measurement and Control Laboratory IMRT at ETH supported application work for the engine control unit and the λ-regulation.

VW Wolfsburg, Bosch, Corning and Engelhard were the industrial partners. The project was funded by the Swiss Gas and Water Industry Association SVGW, the German Technical and Scientific Association for Gas and Water DVGW, the Austrian Gas and Water Industry Association ÖVGW and the Swiss Federal Office of Energy (BFE).

The overall strategy of the CEV focussed on one hand on increasing the part load efficiency by optimising thermodynamics and realising downsizing and on the other hand on reducing tail pipe emissions by applying new catalyst converters including sophisticated controls dedicated to compressed natural gas. The engine was driven with λ=1 in the whole map, where the regulation strategy has been improved for natural gas application.

In this work, the aim was to optimise the thermodynamic process by increasing the compression ratio and driving the engine with high uncooled EGR rates to reduce pumping mean effective pressure and engine out NOx emissions. Due to the power loss in full load operation with CNG compared to the gasoline fuelled production engine an adequate turbocharger had to be found. Furthermore, a new transmission was installed to drive the engine in operating points with higher efficiencies.

These modifications offer various possible driving options, whereon simulation tools have been used successfully to find the optimal strategy and to accelerate the development process. A new empirical combustion model was used to predict the fuel consumption for different stages during the development process. The phenomenological model supported the understanding of the combustion behaviour and 3-Dimensional calculations have been performed to confirm the findings [70]. The combustion models are described in chapter 3.

For all the modifications mentioned above the process of development was to predict the potential by simulation tools first, to test the modifications on the engine test bench afterwards and finally to examine the effects on the roller test bench.

The effect of higher compression ratios on fuel consumption was investigated applying the empirical model. Figure 1.3 shows the determination of the compression ratio for one operating point, where the spark timing was varied to optimise fuel consumption for each of the investigated compression ratios.
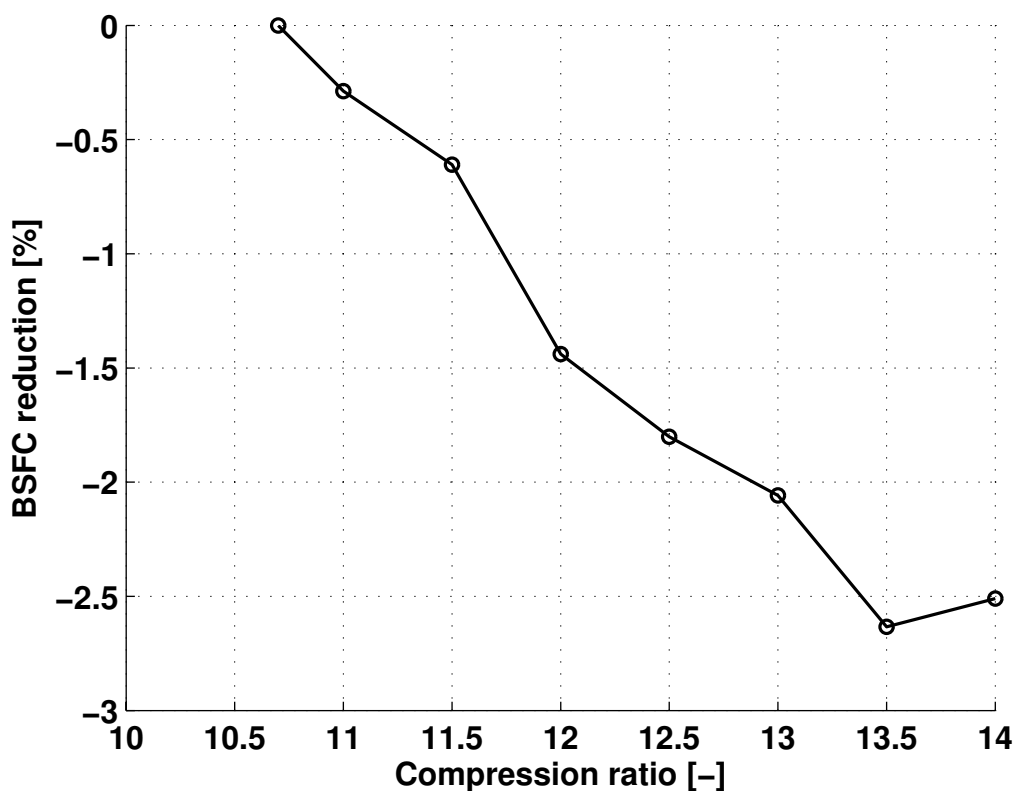
Figure 1.3: Reduction of brake specific fuel consumption BSFC as a function of compression ratio based on n=2000rpm, bmep=2bar, ε=10.7

Based on the actual stored maps in the engine control unit for ε=10.7 a maximum potential of -2.6% was observed for reducing fuel consumption. Starting from this calculation, it was found, that the compression ratio should be increased as high as possible. From the combustion chamber design it was known, that a compression ratio up to ε=13.5 was practicable by changing the piston bowl. Based on these calculations flat pistons were installed (see figure 3.20, chapter 3.7) to change the compression ratio of the engine to ε=13.5. Figure 1.4 shows the comparison for four operating points for the prediction of the change in fuel consumption with the empirical model and the engine test bench results based on the measurements with ε=10.7. The numbers on the x-axis indicate the engine speed in rpm and bmep in bar, respectively.
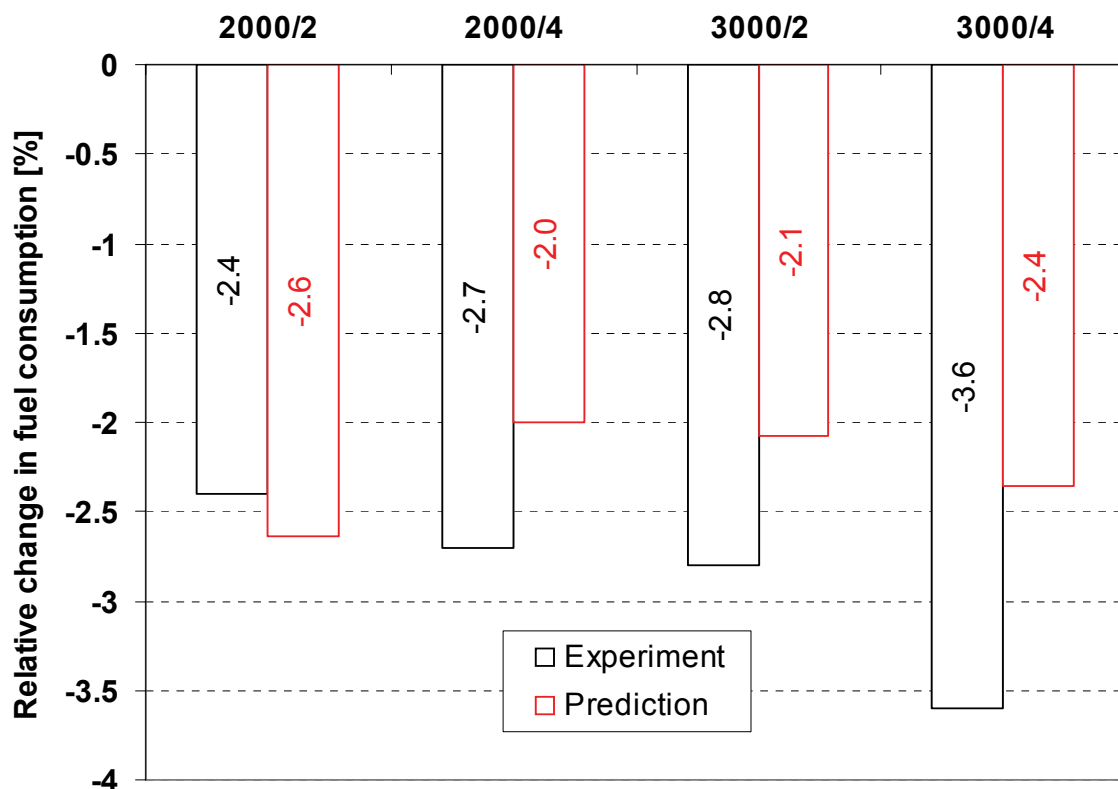
Figure 1.4: Comparison between prediction and experiment for the reduction of fuel consumption for ε=13.5 based on ε=10.7

For the objectives defined in the project two possible turbochargers were found and have been tested using simulation tools. The full load operating behaviour of the engine was defined to achieve torque and power of the next bigger 1.4-litre gasoline engine which has a torque of 116Nm from n=2000rpm to 3500rpm and a maximum power of 44kW power at n=5000rpm.

Figure 1.5 compares the simulation results for both turbochargers and the naturally aspirated engines for full load operating conditions. The power loss of about 15% in the $\varepsilon=10.7$ case and of about 10% in the $\varepsilon=13.5$ case compared to the gasoline engine is also observable.
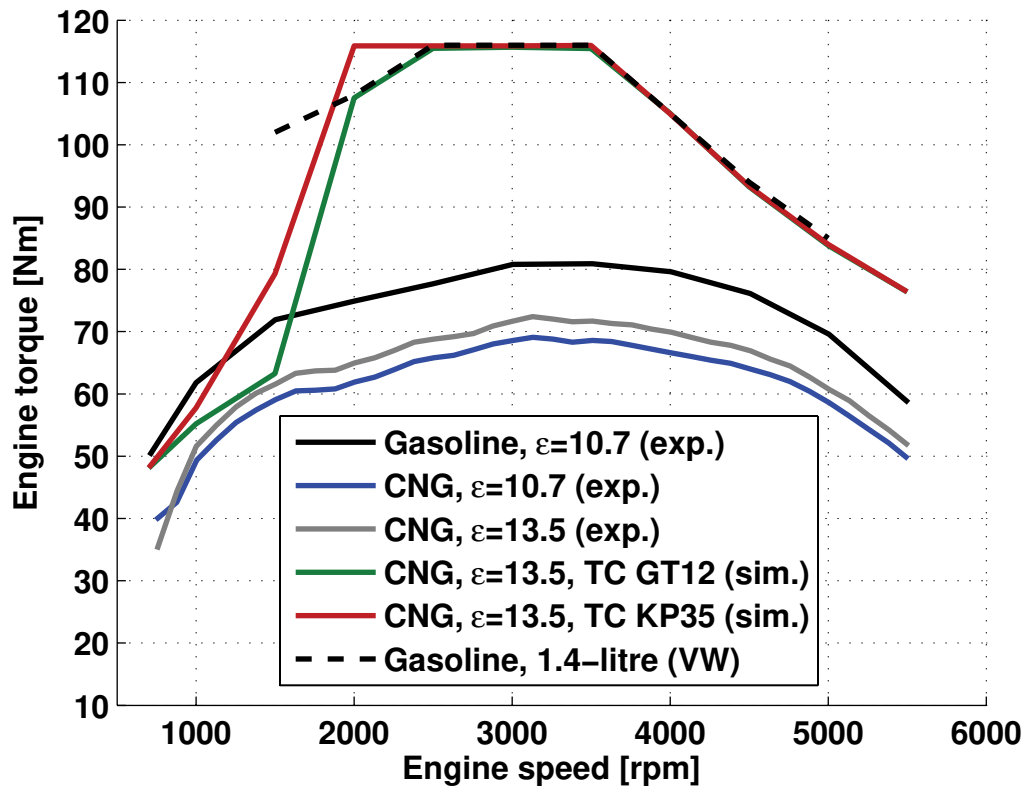
Figure 1.5: Full load performance for different fuels and concepts, experiment (exp.) and simulation (sim.)

Although both turbochargers fulfilled the objectives the KP35 turbocharger was selected to be installed due to the higher resulting torque at low engine speeds.

For the part load operation two waste-gate strategies were tested to determine the effect on the fuel consumption. While the waste-gate remains open in part load operation for the „waste-gate open" strategy, the waste-gate is only opened if the boost pressure had to be limited for the „waste-gate closed" strategy.

The following figure shows the isolines of the relative increase in brake specific fuel consumption with turbocharger compared to the naturally aspirated engine with $\varepsilon=13.5$:
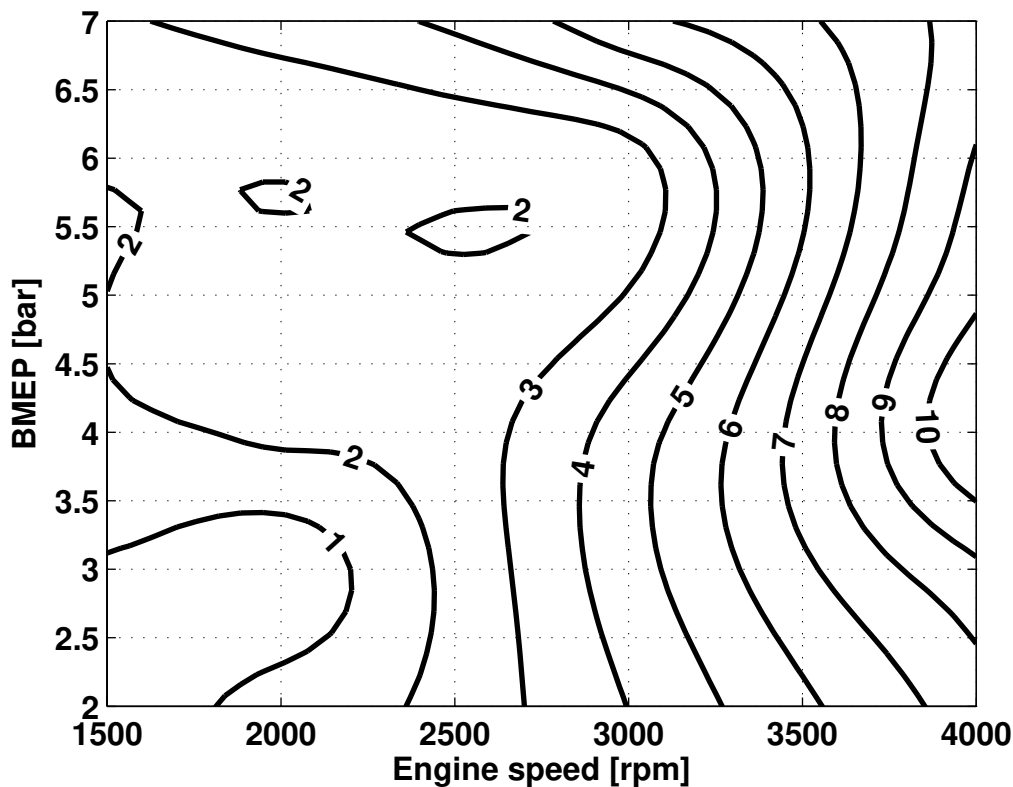
Figure 1.6: Percentage increase in brake specific fuel consumption for the engine with turbocharger and „waste-gate closed" strategy compared to the naurally aspirated engine, ε=13.5

The fuel consumption increases in the entire map, where for higher mass flow rates the back pressure increases for the turbocharged engine and therefore a higher fuel consumption disadvantage can be observed. The increased back pressure is responsible for higher EGR rates, where the valve opening for the turbocharged engine was chosen equivalent to the EGR valve position of the naturally aspirated engine. For medium load (BMEP 4 to 6 bar) it can be observed, that the increase in fuel consumption is reduced due to the high EGR rates leading to reduced throttle losses. The EGR valve is closed at bmep=7bar and therefore the fuel consumption increases rapidly.

The „waste-gate open" strategy has led to slightly higher fuel consumptions. It has to be mentioned that for these small changes uncertainties in the simulation lead to relatively high variations.
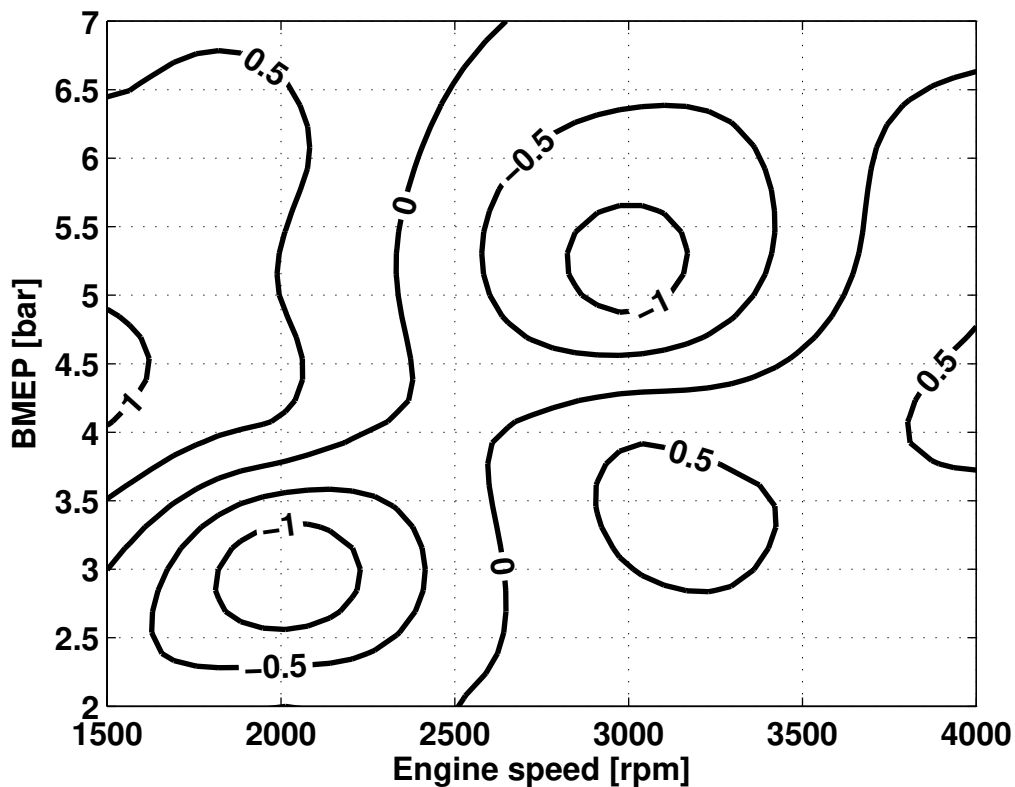
Figure 1.7: Percentage increase in brake specific fuel consumption for the engine with turbocharger and „waste-gate open" strategy compared to the naturally aspirated engine, ε=13.5

Based on these maps the fuel consumption of the vehicle in the New European Driving Cycle has been extrapolated by modelling the vehicle dynamics. For the „waste-gate closed" strategy an increase of 4% was calculated whereas the fuel consumption increases 0.5% for the „waste-gate open" strategy.

An additional advantage of the „waste-gate open" strategy is that the hot exhaust gases by-pass the turbine and support the warm up of the catalyst converter.

Only the „waste-gate open" strategy has been tested on the engine because the adaptation of the engine management system to one of these strategies was very time consuming.

Finally, the Polo equipped with the CEV-engine has been tested on the roller test bench. For the test cycles three different gas compositions had to be used. While the vehicle has to fulfil the emission standards with two synthetic gases in the NEDC, only one natural gas (California certification fuel) has to be employed for the FTP-75 cycle.

	G20	G25	Cal. NG
Methane	100%	86%	89.9%
Ethane	--	--	4.0%
C3 and higher	--	--	2.0%
Oxygen	--	--	0.5%
Inert gases	--	14% (N_2)	3.5%

Table 1.1: Natural gas compositions for the test procedure

The following table summarises the final CO, the total hydrocarbons T.HC, non methane hydrocarbons NMHC and NOx emissions in the NEDC and they are compared with the gasoline production car and the legislation standards. The vehicle has to fulfil emission standards with G20 and G25.

NEDC	CO [g/km]	T.HC [g/km]	NMHC [g/km]	NOx [g/km]
Gasoline	0.12	0.07	0.05	0.06
Natural gas G20	0.14	0.1	0.00	0.00
Natural gas G25	0.15	0.09	0.01	0.00
Euro 4	1.0	0.1	--	0.08

Table 1.2: Exhaust emissions in the NEDC

Table 1.3 shows the results obtained in the FTP-75 cycle driven with the California certification fuel. In contrast to the European legislation standards, an emission standard for the Non Methane Hydrocarbons is used here.

FTP-75 cycle	CO [g/km]	T.HC [g/km]	NMHC [g/km]	NOx [g/km]
Gasoline	0.114	0.028	0.020	0.064
Natural gas	0.081	0.047	0.004	0.001
SULEV	0.62	--	0.006	0.012

Table 1.3: Exhaust emissions in the FTP-75 cylce

A significant reduction in CO_2 emissions could be demonstrated in the NEDC as shown in the following figure. Compared to the gasoline engine with equivalent engine power the CO_2 emission are reduced by 31%. If the software of the engine control unit is only adapted for the NEDC - which is common in industry - a CO_2 reduction of 34.5% is achieved. This is denoted by „NEDC optimised" in the following graph.
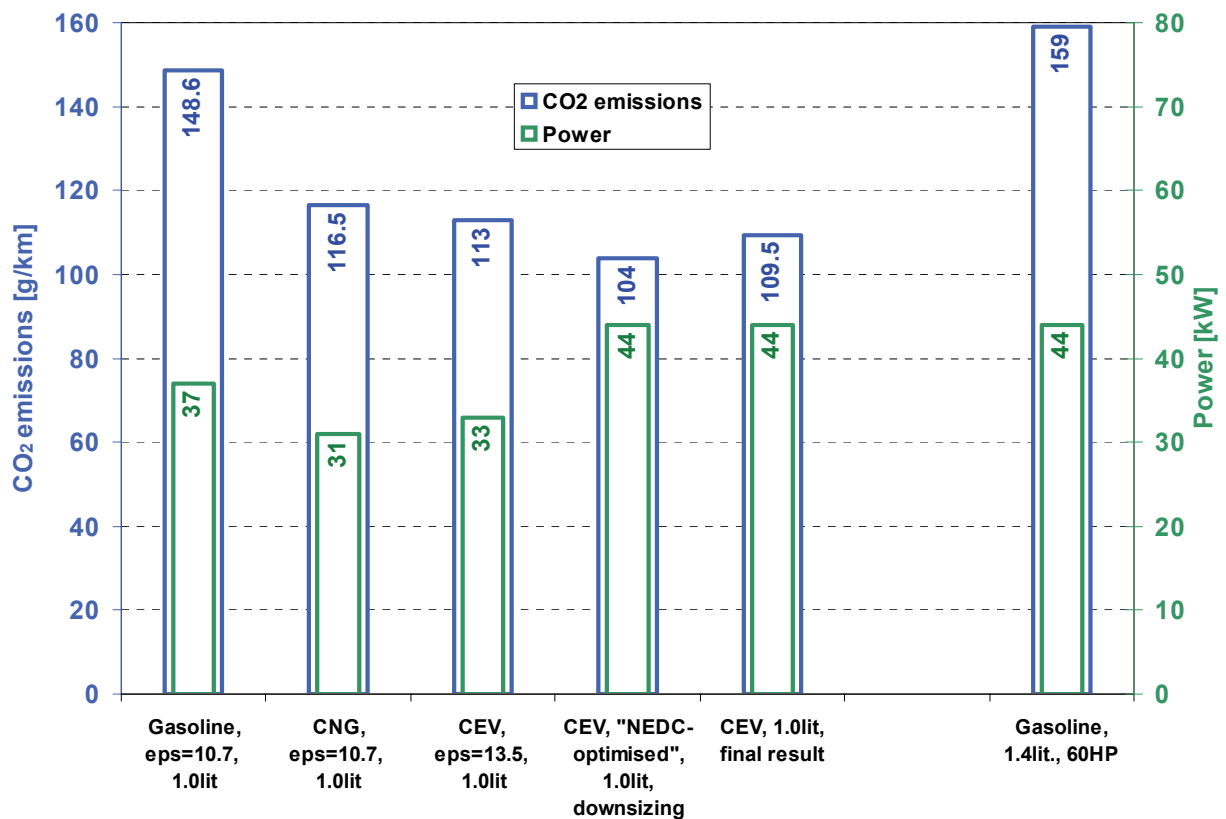
Figure 1.8: CO_2 emissions and engine power in the NEDC

The results shown in tables 1.2 and 1.3 and the results shown in figure 1.8 denoted with final results are performed with the same ECU calibration.

1.3 Objectives of this work

In this work two combustion models dedicated to compressed natural gas engines will be developed. An empirical model formulation will be used for first estimations and predictions of trends. Furthermore, based on the findings made in our group [66] a phenomenological combustion model dedicated to compressed natural gas will be developed, where the model described by Koch [66] should be extended with a turbulence model and has to be redefined to account for CNG operation. These two combustion models are planned to be implemented into a commercial cycle simulation code (GT-Power), where the existing combustion models will be replaced with the new ones by user subroutines. All other models will still be computed by GT-Power.

In the second part of this work, the knock behaviour of a turbocharged engine should be investigated. A special focus will be held on the knock behaviour for different gas compositions and on varying operating conditions. Therefore, gas composition, intake pressure, intake temperature, engine speed and spark timing have to be varied. Five well-defined compositions of synthetic gases will be tested to account for the different components found in compressed natural gases. At the end a knock model based on the knock integal method approach for cycle simulations will be developed considering the parameters described before.

Chapter 2

Experimental Setup and Applied Simulation Tools

2.1 Engine Data

Several engine configurations existed in the CEV-project and therefore, several engine models have been built up for the simulations. For all experiments and simulations a 1.0-litre four cylinder engine was used. Changes have been made on the fuel supply, the compression ratio was increased and for the final configuration a turbocharger was installed. The configurations are listed and explained below.

Configuration 1: Gasoline production engine

Bore	mm	67.1
Stroke	mm	70.6
Number of cylinders	-	4
Number of valves/cylinder	-	2
Compression ratio	-	10.7
Max. torque	Nm	86
Max. power	kW	37
Engine control unit	-	Motronic ME 7.5.10
Exhaust gas recirculation	-	yes

Table 2.1: Basic engine data

This engine configuration was used to generate a base for comparisons on the roller test bench. During this stage, no cylinder pressure transducer was installed and therefore no simulations have been made.

Configuration 2: The basic engine setup described as configuration 1 remained the same as shown in table 2.1 except the whole fuel supply was changed and pure methane was used for the experiments and the simulations. The maps in the engine control unit have been adjusted to compressed natural gas operation. This configuration was used to develop the empirical and the phenomenological combustion model (see chapter 3). The engine was equipped with a water-cooled pressure transducer.

Configuration 3: Configuration 2 was changed to a compression ratio of ε=13.5 by installing new pistons. The maps in the engine control unit have been adapted to the new configuration. This configuration was used to predict the engine behaviour by simulation tools first and later on to verify the models for different combustion chamber designs.

Configuration 4: A turbocharger has been installed, where the compression ratio remained ε=13.5. The engine control unit was adapted to turbocharger operation and the „waste-gate open" strategy described in chapter 1.2 was realised. Simulation tools have been applied to find the turbocharger. This engine configuration was used to investigate the knock behaviour and to develop the knock model (see chapter 4).

2.2   Engine Test Bench

The engine was built up on a Schenk W150 test bench. All temperature, pressure - except the in-cylinder pressure -, air mass flow rate, fuel mass flow rate and torque measurements have been collected and stored in the PCII system. The environmental temperature and humidity were kept constant during the tests. The exhaust gases have been measured by a Horiba Mexa 9200 exhaust gas analyser.

A Kistler 6043Asp water-cooled pressure transducer coupled with a Kistler charge amplifier type 5011 was used to measure the in-cylinder pressure of cylinder 1. The instantaneous intake pressure was recorded by a Kistler 4075A5 sensor. The top dead centre position has been detected using a Baumer crank shaft encoder. Furthermore, this encoder has been used as clock. These signals have been recorded using an Elsys (Elsys AG) transient recorder and the software Elsys Trans-PC was used

to visualise the crank angle based signals. The resolution was set to 0.2° CA for the combustion analysis and 0.1° CA for the knock investigations.

The air mass flow rate was measured by an ABB thermal mass flowmeter Sensyflow and the fuel mass flow was measured using a Rheonik sensor. The Rheonik mass flowmeter is based on the patented Omega shaped torsion swinger. Additionally, the engine was equipped with several mean temperature and mean pressure measurements in the intake and the exhaust systems.

The engine was equipped with a R&D ECU, where the software VS100 allowed changing various values. For the numerous investigations during this work the engine speed, throttle angle, EGR valve position and spark timing have been fixed to ensure reproducible results. Additionally, the intake pressure and - by using an air-water cooler - intake temperature were kept constant for the tests with the turbocharged engine.

Due to the various configurations examined in this work the operating points investigated and the gas compositions considered are listed in the corresponding chapters.

2.3   Thermodynamic Calculation

A two-zone model formulation was used for both simulation tools described below. The code WEG („Wärmeentwicklungsgesetz") developed by Obrecht [84] was used for the „backward calculation", where measured cylinder pressure traces have been read in and the burn rate was computed. The commercial code GT-Power [45] was used for the „forward calculation", were the burn rate was modelled and the in-cylinder pressure trace was calculated.

In a two-zone model formulation the combustion chamber is divided into a zone consisting of burned gases and a zone consisting of unburned gases, where these zones are defined by their species and are assumed to be homogenous. The unburned and burned gases are separated by a sharply defined infinitesimal small reaction zone. In principal, both zones can exchange mass and enthalpy with the intake and exhaust systems during the gas exchange process. In addition, the mass exchange between the zones is considered. The mass of the unburned gases decreases and has to be added to the burned zone during combustion. The enthalpy flux from the burned to the unburned gases can occur after the gas exchange process, if residual gases remain in the cylinder.

Further assumptions have to be made for the wall heat losses. Woschni's correlation was used here, whereas the original formulation was developed for a one zone model. Inhelder [59] suggests to split the heat flux as a function of the instantaneous volumes of the zones. In this case the surface is described as $A_i \sim V_i^{2/3}$.
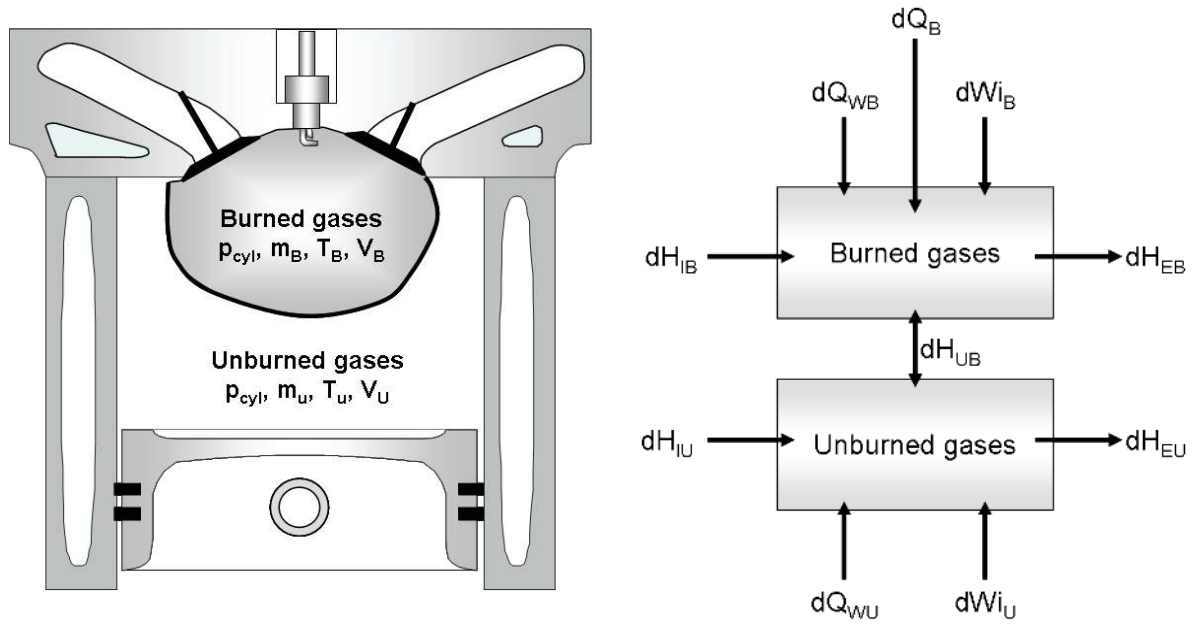
Figure 2.1: Two-zone model formulation

The in-cylinder pressure p_{cyl} is assumed to be independent of the coordinates for normal combustion, because the speed of sound is much higher than the turbulent flame speed. This leads to

$$p_U = p_B = p_{cyl} \qquad\qquad 2.1$$

The energy balance for the zone consisting of burned gases can be derived as

$$\frac{dU_B}{dt} = m_B \cdot c_{v_B} \cdot \frac{dT_B}{dt} + c_{v_B} \cdot T_B \cdot \frac{dm_B}{dt} + m_B \cdot \sum \frac{du_B}{dx_k} \cdot \frac{dx_k}{dt}$$

$$= -p_{cyl} \cdot \frac{dV_B}{dt} + \sum \dot{H}_{xB} + \sum \dot{Q}_{xB} \qquad\qquad 2.2$$

In equation 2.2 it is considered, that the mixture consists of several species k whose mass fractions are defined by x_k. Furthermore, the terms shown in figure 2.1 have been used, where the temperature T_B, the mass m_B, the volume V_B, the enthalpy fluxes $\dot{H}_{xB}$ and the heat fluxes $\dot{Q}_{xB}$ are taken into account.

The formulation for the zone consisting of unburned gases can be derived similar. The equation of state can be applied and is given here exemplary for the burned zone.

$$V_B \cdot \frac{dp_{cyl}}{dt} + p_{cyl} \cdot \frac{dV_B}{dt} = R_B \cdot T_B \cdot \frac{dm_B}{dt} + m_B \cdot T_B \cdot \frac{dR_B}{dt} + m_B \cdot R_B \cdot \frac{dT_B}{dt} \quad 2.3$$

The formulation for the in-cylinder pressure p_{cyl} can be derived by combining the equations for the burned and the unburned gases, solving the energy balance for dT_U/dt and dT_B/dt respectively and inserting in the equations of state.

$$
\begin{aligned}
\frac{dp_{cyl}}{dt} = \frac{1}{\dfrac{V_U}{\kappa_U} + \dfrac{V_B}{\kappa_B}} \cdot \Bigg[& -p_{cyl} \cdot \frac{dV_{cyl}}{dt} + \frac{R_U}{\kappa_U} \cdot \left(T_U - \frac{u_U}{c_{v_U}} \right) \cdot \frac{dm_U}{dt} \\
& + \frac{R_B}{\kappa_B} \cdot \left(T_B - \frac{u_B}{c_{v_B}} \right) \cdot \frac{dm_B}{dt} \\
& + \frac{R_U}{c_{p_U}} \cdot \left(\sum \dot{H}_{xU} + \sum \dot{Q}_{xU} - \sum \frac{du_U}{dx_k} \cdot \frac{dx_k}{dt} \right) \\
& + \frac{R_B}{c_{p_B}} \cdot \left(\sum \dot{H}_{xB} + \sum \dot{Q}_{xB} - \sum \frac{du_B}{dx_k} \cdot \frac{dx_k}{dt} \right) \\
& + m_U \cdot T_U \cdot \frac{dR_U}{dt} + m_B \cdot T_B \cdot \frac{dR_B}{dt} \Bigg]
\end{aligned}
\qquad 2.4
$$

Mass and volume conservation can be applied for the combustion chamber where the mass and volume of the unburned zone m_U and V_U and the burned zone m_B and V_B are time dependent.

$$m_{cyl} = m_U + m_B \qquad 2.5$$

$$V_{cyl} = V_U + V_B \qquad 2.6$$

The temperatures of the unburned and the burned zone are defined based on the following equations:

$$\frac{dT_U}{dt} = \frac{1}{m_U \cdot c_{pU}} \cdot \left(V_U \cdot \frac{dp_{cyl}}{dt} - h_U \cdot \frac{dm_U}{dt} + \sum \dot{H}_{xU} + \sum \dot{Q}_{xU} \right.$$
$$\left. - m_U \cdot T_U \cdot \frac{dR_U}{dt} - m_U \cdot \sum \frac{du_U}{dx_k} \cdot \frac{dx_k}{dt} \right)$$

<div align="right">2.7</div>

$$\frac{dT_B}{dt} = \frac{1}{m_B \cdot c_{pB}} \cdot \left(V_B \cdot \frac{dp_{cyl}}{dt} - h_B \cdot \frac{dm_B}{dt} + \sum \dot{H}_{xB} + \sum \dot{Q}_{xB} \right.$$
$$\left. - m_B \cdot T_B \cdot \frac{dR_B}{dt} - m_B \cdot \sum \frac{du_B}{dx_k} \cdot \frac{dx_k}{dt} \right)$$

2.3.1 Burn Rate Analysis

WEG [84] uses measurement data as input values and calculates burn rate curves, where a closed thermodynamic system is used. The data analysis was performed using a two-zone model formulation for all experiments.

The pressure data are first smoothened by a polynomial smoothing algorithm. The absolute values of the in-cylinder pressure are found by assuming that the pressure in the intake manifold and the in-cylinder pressure are equal, when the intake valve is open and the piston is at bottom dead centre.

The total in-cylinder mass at inlet valve close is found with the known engine speed, mass flow rates of air, fuel and EGR and by an approach for the residual gases developed by Fox et al. [42]. The in-cylinder temperature can be found by applying the equation of state with the cylinder pressure, cylinder volume, total mass and the composition of the cylinder charge.

The heat transfer model of Woschni was used, where the wall temperatures have been estimated by a formulation developed by Bargende [10].

The burn rate and some relevant data can be found by solving the equations described earlier.

2.3.2 Engine Cycle Simulation Tool

The „forward calculations" have been performed using the commercial software tool GT-Power developed by Gamma Technologies Inc. [45]. In contrast to the „backward formulation" 720° crank angle simulations are performed here and therefore, an open system has to be assumed. Furthermore, GT-Power solves equations for mass, energy and momentum in the intake and exhaust system. In this case, dynamics of the gas exchange process can be investigated [75, 109].

A two-zone model formulation was used for all calculations, where the formulation of the model is in general equal to the one shown in equations 2.4. But the source code is unknown and therefore differences can not be described here.

The engine model has been first validated by predefining the burn rate curves calculated by WEG. This procedure allowed testing the intake and exhaust system leading to accurate mass flow rates, temperatures and pressures along the intake and exhaust paths. The predefined burn rate curves have then been replaced by user subroutines described in chapter 3.

2.3.3 Bio-inspired Algorithm

The bio-inspired algorithm as implemented by Warth [19, 116, 117] has been used to find the parameters defined in the knock model. These algorithms - also known as evolutionary or genetic algorithm - try to imitate Darwin's evolutionary principles in a mathematical manner. First, an initial population is generated by a stochastic procedure within a defined parameter range. All these individuals - in technical applications: a parameter set - are then assessed based on a target value and a fitness value is assigned, meaning that the probability to select an individual increases with increasing fitness and target value. For technical applications, the fitness assessment for example occurs based on the square of the deviation of experimental and computed value. After this selection, new individuals are created by recombination of the individuals selected („parents"), where different combinations, mutations and cross-over processes are applied. The whole procedure is repeated until a predefined number of generations is achieved.

2.4   Engine Model Validation

Before the combustion models described in chapter 3 have been tested the entire engine model was verified to exclude other influences on the combustion simulation results. The experimentally determined burn rate curves have been approximated by Vibe functions for several operating points, where the Vibe parameters found were kept constant during the simulation of one operating point. Very good agreements between measurements and simulations have been obtained.

In figure 2.2 and figure 2.3 the model validation is shown for two operating points. In the first two diagrams the burn rate and the cumulative burn rate are compared. In some cases, the experimentally determined cumulative burn rate curve can not be approximated by a Vibe function in the late period of the combustion. Attention was paid to have a good agreement in the early period leading to accurate results.

By analysing the cylinder pressure curves, it was found, that most of the computed maximum pressures were about 3% higher than the experimentally determined maximum pressures. This may be a consequence of different formulations of some submodels in WEG and GT-Power. The intake pressures correspond well for all operating points investigated leading to good agreement of mass flow rates. It was very important to analyse the varying intake pressure to test the entire intake system, which is quite sensitive to model inaccuracies and which influences the whole model performance.

The temperatures show some differences in the values and a shift can be observed. Again, this may be a consequence of different model formulations and furthermore, it was seen, that the temperatures are sensitive to experimental inaccuracies. In some operating points the experimentally determined burn rate was observed to have slightly negative values before spark timing and in some cases small oscillations before combustion start have been observed. These oscillations - coming from experimental uncertainties in the pressure measurement - lead to inaccuracies in the temperature trace.

Overall, the engine model has the capability to reproduce the experimental data for a wide range of operating conditions very well.
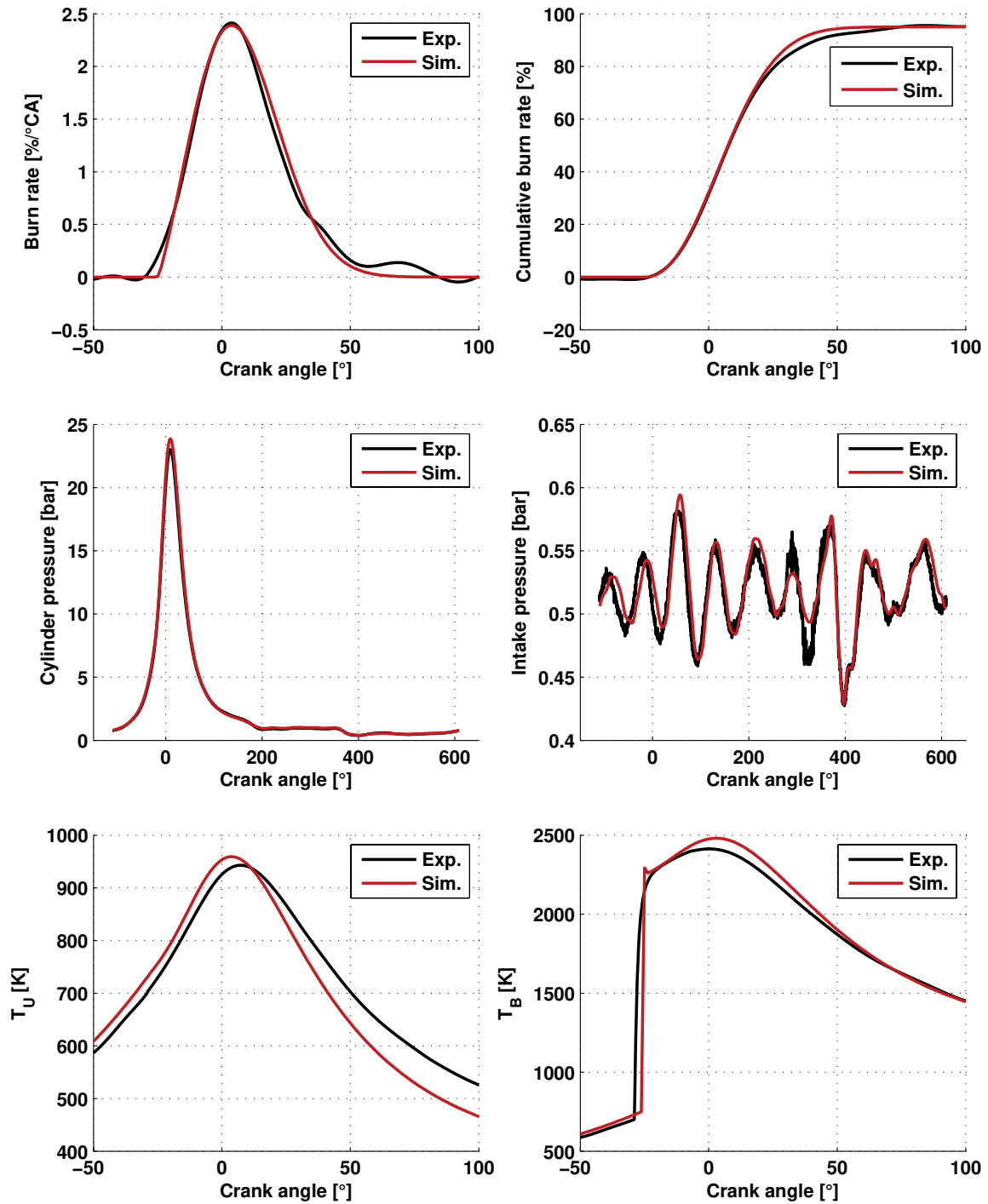
Figure 2.2:   Engine model validation for one operating point: n=2000rpm, bmep=2bar, spark timing=48.75° crank angle BTDC, EGR rate=10.5%, ε=10.7
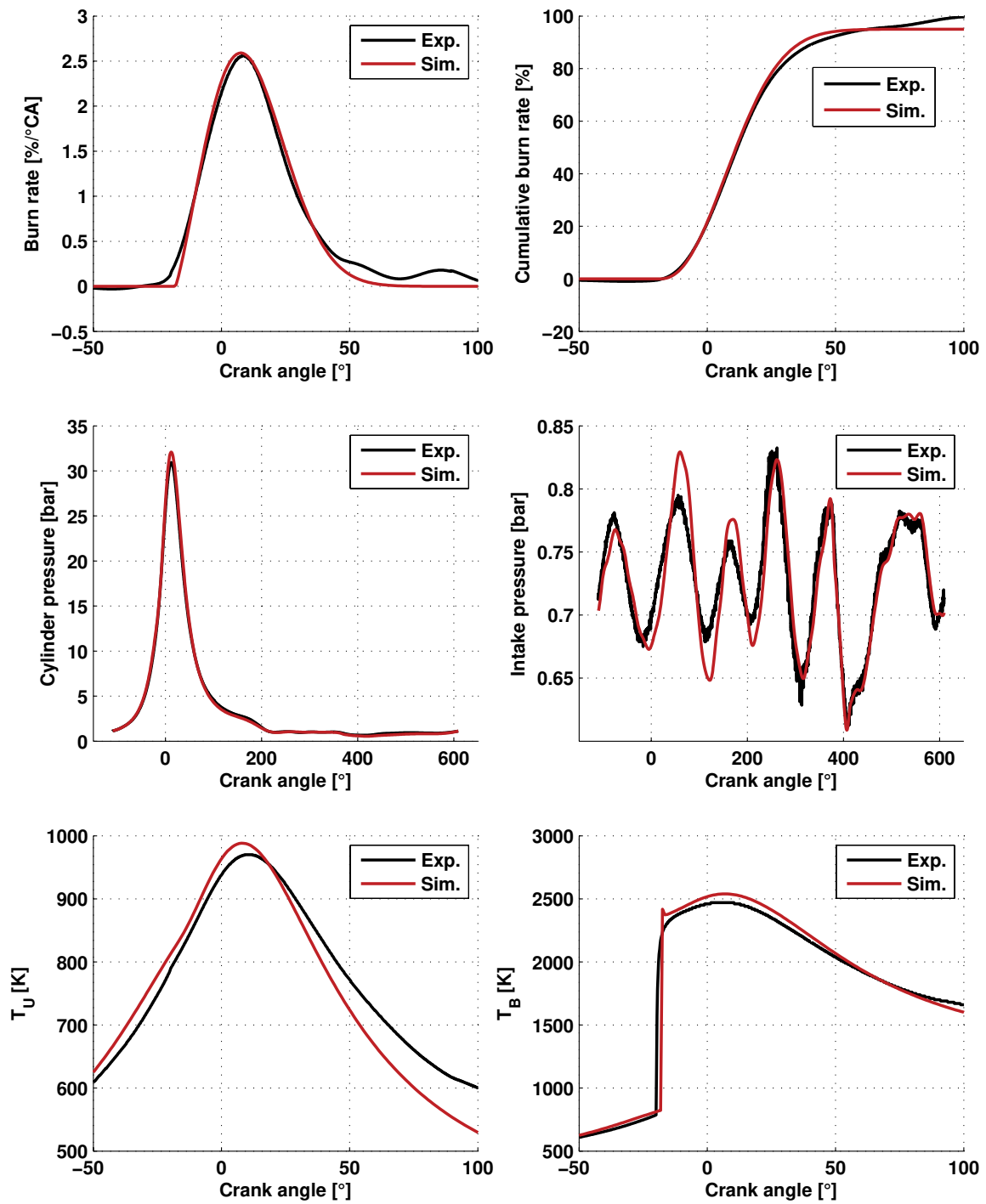
Figure 2.3: Engine model validation for one operating point: n=3000rpm, bmep=4bar, spark timing=40.5° crank angle BTDC, EGR rate=8.7%, ε=10.7

Chapter 3

Empirical and Phenomenological Combustion Model Approach

Simulation tools have been used successfully to assist the experiments on the engine test bench and to find the optimal strategy in the CEV-project. Various strategies were investigated through simulation and the one with the highest efficiency was transferred to the engine. The predictions and the experiments agreed very well.

The burn rate is treated as an external heat source in the energy balance equation. Depending on whether a Vibe approach or a flame propagation model is used, the formulation of the burned fuel mass rate has to be adjusted. While the Vibe function assumes a combustion progress variable, the flame speed and the flame front area have to be defined in the phenomenological case.

In both cases the flame front position is not explicitly described. All the models used in the phenomenological description are based on mean values, meaning that the spatial distribution is not considered. The only differentiation is made between values averaged over the entire combustion chamber, averaged values in the unburned and burned zone as the two-zone model formulation described in chapter 2.3 indicates.

The literature review showed that no specific combustion models for stoichiometric operated natural gas engines exist. Some models dedicated to lean burn CNG operating conditions and low engine speeds have been developed.

Therefore, a fast and simple empirical combustion model has been developed to predict fuel consumption, where the phenomenological model additionally was used to support the interpretation of the experiments. Both models were

implemented into GT-Power by a user subroutine and have been tested for a wide range of operating conditions. The use of the commercial code GT-Power coupled with a user subroutine allowed to focus on the combustion model.

3.1   State of the Art

For industrial applications three classes of combustion models can be applied. Zero-dimensional models are often used to develop empirically based models when fast and simple approaches are required. In the formulation of the burn rate changes in engine operation conditions are only considered if the model was build up with the corresponding parameter variations. Phenomenological models are based on physical observations and are able to take into account physical changes. In this approach a propagating flame is described where the unburned mixture entrains the flame and is burned. The flame front is assumed to be infinitesimal small. Both types of models are used in engine cycle simulation tools. If 3D-CRFD codes are used specific models for this software tools are needed.

Csallner [34] introduced an empirical combustion model based on the conversion of the Vibe parameters depending on engine operating conditions. He varied one parameter on the engine dyno while the other parameters were kept constant. He investigated the influence of rpm, load, λ and spark timing for two engines and additionally examined the effect of residual gas mass fraction and intake temperature for one engine.

He then set up rules how to change the Vibe parameters for these variations and verified the model for a 3.3-litre single cylinder MTU engine fuelled with propane and for a 2-litre BMW gasoline engine for a wide range of operating conditions.

Further refinements have been made by different researchers. An overview of these models for gasoline engines can be found in [122]. Witt [122] further developed the combustion model and extended it to higher residual gas mass fractions and for unthrottled operation. He therefore used variable valve timings. In all these cases, the test engines were fuelled with gasoline.

Zeilinger and Zitzler [126, 127] transferred this approach to lean burn compressed natural gas engines for displacements of 4 to 13.5-litres per cylinder and maximum engine speeds of 900rpm and 2500rpm. They additionally examined the

influence of the gas composition and - for the dual fuel engine - the injection timing. Finally, they focused on matching the experimental with the predicted pressure traces.

The basic procedure to develop a burn rate based conversion model can be visualised as follows:
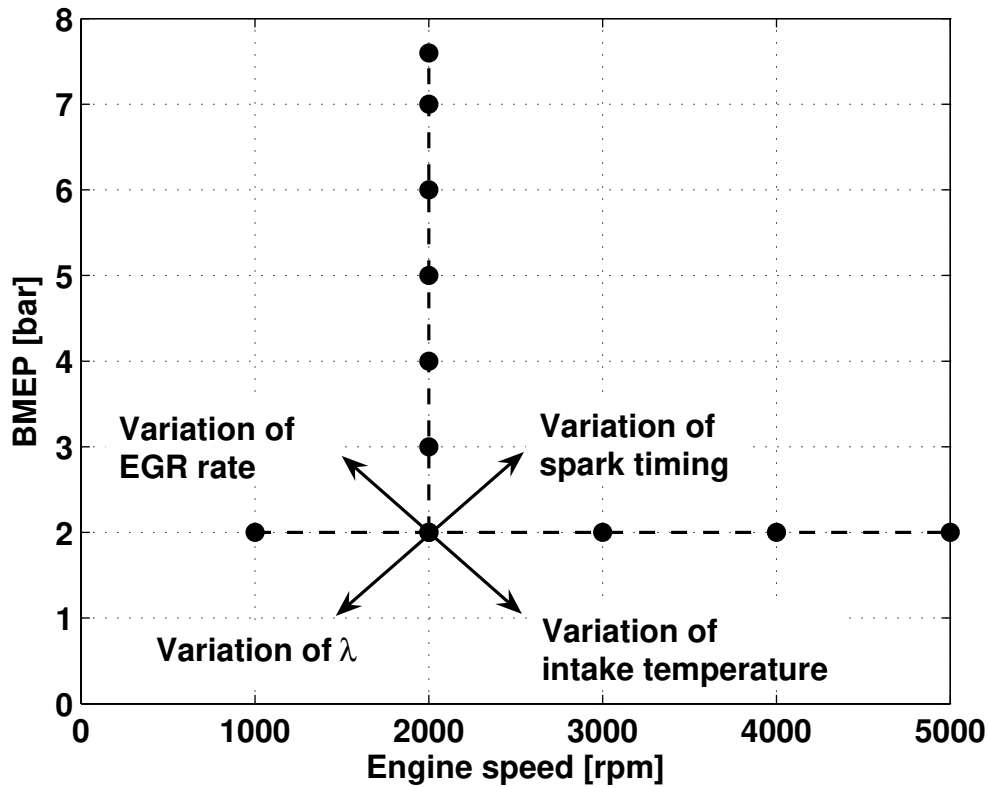
Figure 3.1:   Developing an empirical combustion model

A single step global reaction scheme for the inflammation phase was used by Soylu and Gerpen [102]. For the developed turbulent flame a Vibe function was used. The parameters of the Vibe approach and the global reaction scheme have been adjusted to match experimental results. They made their observations on a 7.6-litre 6 cylinder engine and varied the excess air ratio λ and the ignition timing. The natural gas composition - consisting of 94% methane, 3% ethane, 3% propane, nitrogen and others - and the engine speed of 1500rpm were kept constant.

If phenomenological models are used, formulations for the turbulent flame speed - as a function of the laminar flame speed and the turbulence intensity - and the flame front area are necessary. Several descriptions for each of these submodels exist.

Formulations for the laminar burn speed have been determined experimentally. For gasoline engines the model of Metghalchi and Keck [78] is often used. In a constant combustion chamber the effect of equivalence ratio, temperature, pressure and dilution on laminar burning velocity has been investigated. Rhodes and Keck [92] refined Metghalchi and Keck's approach. Instead of 85% N_2 and 15% CO_2 they used a mixture consisting of 80% N_2 and 20% CO_2 as dilution gas which was chosen to meet heat capacity of the actual exhaust products from stoichiometric combustion of the fuels tested. The percentage reduction in laminar burning speed due to the addition of simulated residual gas was found to be only a function of the amount added but independent of the properties of the mixture.

Liao et al. [73] developed a laminar burn speed model for compressed natural gas based on experiments in a constant combustion chamber. The composition of the CNG by volume fractions was 96.16% methane, 1.096% ethane and the remains including hydrocarbons higher than C_3, CO_2, N_2, sulfurated hydrogen and water. Furthermore, the effect of dilute gas consisting of 88% N_2 and 12% CO_2 has been studied.

Gu et al. [51] investigated laminar burning speed at three different equivalence ratios and developed three different approaches for each of the examined equivalence ratio. They used methane as fuel and compared their results with various experimental data found in the literature and with numerical data using the GRI-Mechanism. Experimental data agreed well whereby the numerically obtained flame speeds gave higher values. The authors speculate that the mechanism was calibrated with experimental data in the past, which showed too high values.

Witt and Griebel [123] used the GRI3.0-Mechanism to find the laminar flame speed for methane for a wide range of pressures and temperatures. Available experimental data have been compared with the computations and the agreements were found to be quite well. Investigations with dilute gas were however not carried out.

A combustion vessel was used by Elia et al. [39]. They examined the laminar burning velocity of methane for different equivalence ratios, for pressures up to 70atm and temperatures up to 550K. An extension for temperatures up to 650K and a verification of the developed approach was made by Rahim et al. [90]. The effect of dilute gas consisting of 86% N_2 and 14% CO_2 was investigated and taken into account in the formulation.

The different trends found for gasoline and natural gas are compared in figure 3.2 as a function of the normalised temperature and pressure.

For the temperature dependence p/p_0 was set to 1 and for the pressure dependence T/T_0 was set to 1. T_0 is between 298K and 300K and p_0 is between 1bar and 1.013bar for all the approaches plotted. For SL_0 the values are 0.375m/s (Elia), 0.36m/s (Gu), 0.395m/s (Liao) and 0.38m/s (Witt/Griebel). SL_0 for gasoline engines was found to be 0.281m/s for both approaches.
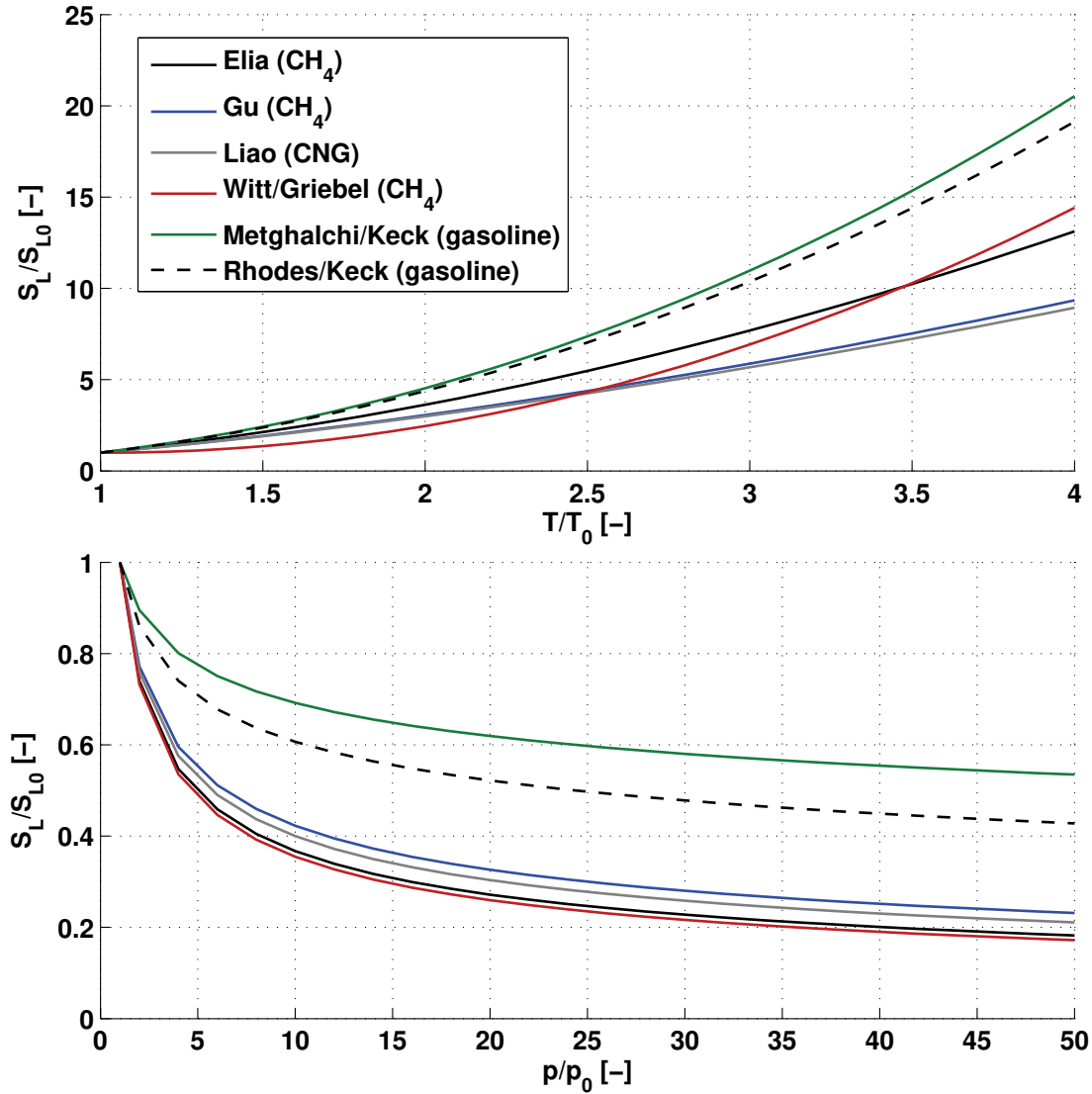
Figure 3.2: *Dependencies of the laminar flame speed on temperature and pressure according to different approaches and experimental investigations*

A lot of models exist for the turbulent flame speed. Based on the formulation of Damköhler a lot of refinements have been made. The basic idea is that the turbulence wrinkles the flame and increases the flame front area therefore. Applying conservation of mass leads to the following formulation.
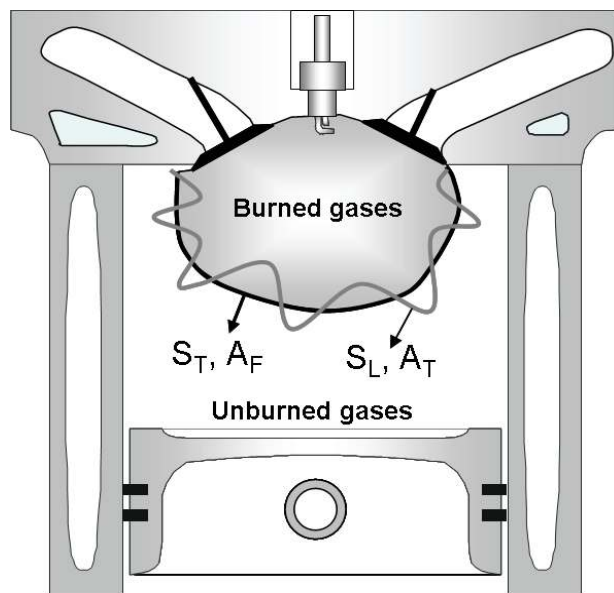
$$S_T \cdot A_F = S_L \cdot A_T$$

$$\text{or}$$

$$\frac{S_T}{S_L} = \frac{A_T}{A_F}$$

Figure 3.3:   Definition of the turbulent flame speed

An overview of different approaches can be found in [52]. Abdel-Gayed and Bradley [3] investigated the turbulent flame speed for hydrogen-air mixtures and introduced a correlation between the turbulent Reynolds number and the turbulent flame speed. Gülder [52] used a modification of Damköhler's approach and verified the dependence on the turbulent Reynolds number.

A different approach has been developed by Blizard and Keck [13], which was refined by Tabaczynski et al. [111] and verified by Hires et al. [55]. This model is known as the entrainment model, is often used and is implemented in GT-Power. The basic idea is that eddies consisting of unburned gas entrain the flame front and are burned with a time delay, the so called burnup time. The mass burning rate is given by the total mass of unburned mixture within the flame divided by the characteristic burnup time. Blizard and Keck assumed that the entrainment speed is correlated with the inlet gas speed through the valves and therefore avoided the use of a turbulence model. Tabaczynski and Hires assumed that the entrainment velocity is proportional to the density of the unburned mixture to the power of one third.

Various formulations for the in-cylinder turbulence can be found in the literature. A two equation k-ε turbulence model was introduced by Achuth and Mehta [4]. They assume that the mean flow field spins in a two-dimensional plane. A

tumble vortex is assumed to have an elliptical shape in 2D. Two velocities are defined along the x and y directions. Conservation of angular momentum for the mean vortex is used and wall shear stresses are considered. The instantaneous tumble velocity is found. Davis and Borgnakke [35] calculate the turbulence intensity for the unburned and the burned zone where the formulation includes swirl and squish flow. For each of these zones they built up a two equation turbulence model. For combustion analysis, they use the entrainment model.

Morel and Keribar [80] focused on diesel engines with bowl-in piston combustion chamber, divided the combustion chamber into three regions and set up a two equation k-ε model for each of these zones. In this case, they get a set of six coupled ordinary differential equations. Morel et al. [79] enhanced this approach for spark ignition engines. The combustion chamber was divided into four zones resulting in a system of eight coupled ordinary differential equations. Axial and radial velocity and swirl, modelled as solid body rotation, have been considered. A one equation model was used by Poulos and Heywood [89], Bargende [10] and Brohmer [24]. If a one equation model is used, the turbulent length scale has to be defined. They calculate the turbulent length scale based on the instantaneous cylinder volume. When combustion starts Poulos and Heywood [89] and Tabaczynski et al. [111] calculate the integral length scale and the turbulence intensity only in function of the density of the unburned mixture. Bargende [10] used the mean density and considers turbulence production due to squish flow.

The formulation of the flame front area has to consider the interaction between the flame front and the combustion walls. Blizard and Keck [13] assumed a cylindrically shaped combustion chamber and a spherically propagating flame. The same procedure was used in [35, 55, 111]. Morel et al. [79, 80] approximated the combustion chamber surfaces with circular discs, annuli, quadrangular or triangular flat panels and curved, cylindrical shells to describe the interaction between the cylinder walls and the propagating flame front. Poulos and Heywood [89] used the following procedure: For each piston position, a series of individual calculations are performed at equal flame radius increments until the flame passes through the chamber. At each radius step, the flame area, enflamed volume, and chamber wall area behind the flame front are calculated. Finally, they store the relevant data to a table. In the thesis of Koch [66] the flame front area was determined by reversing the calculation procedure. The flame front area was calculated based on experimentally determined burn rate curves. This examination of the turbulent flame front area will be used in chapter 3.3.3.

3.2   Empirical Combustion Model Formulation

The empirical combustion model is based on the conversion of the Vibe parameters depending on the engine operating conditions. Starting from a fixed engine operating point one parameter is changed while the others are kept constant as it is shown in figure 3.1. The „star point" was set to n=2000rpm and bmep=2bar. By analysing the burn rate based on measured cylinder pressure curves and adjusting the Vibe parameters to match these experimental data, rules can be defined how the burn rate has to be changed for each of the investigated engine parameter. The resulting conversion factors for the Vibe parameters are obtained by superposing the individual effects.

The burn rate is defined by the total amount of fuel m_F, a rate of change of a progress variable x_B and the lower heating value H_L:

$$\frac{dQ_B}{d\varphi} = \dot{m}_F \cdot H_L = m_F \cdot \frac{dx_B}{d\varphi} \cdot H_L \qquad 3.1$$

The combustion progress variable introduced by Vibe can be described as follows:

$$x_B(\varphi) = 1 - e^{a \cdot y_B^{mv+1}} \qquad 3.2$$

In this formulation m_V is the shape parameter and a is a constant which defines the total amount of fuel burned at combustion end. The constant a can be calculated as

$$a = \ln(1 - x_{BEnd}) \qquad 3.3$$

Vibe suggested to define a=-6.908 which corresponds to x_{BEnd}=0.999. y_B is the normalised combustion duration:

$$y_B = \frac{\varphi - \varphi_S}{\varphi_E - \varphi_S} \qquad 3.4$$

Where: φ =current crank angle, φ_S=crank angle of combustion start corresponding to x_B=0, φ_E=crank angle of combustion end corresponding to x_B=0.999.

It is difficult to find the combustion start and the combustion end from experimentally determined burn rate curves. Therefore the burn duration was defined by the crank angle interval from $x_B=0.05$ to $x_B=0.9$.

The following parameters have been varied to match experimental data using a function which solves non-linear least square problems [113]:

- Ignition delay: $\varphi_{ID} = \varphi_{x_B = 0.05} - \varphi_{sparktiming}$
- Burn duration: $\varphi_{BD} = \varphi_{x_B = 0.9} - \varphi_{x_B = 0.05}$
- Shape parameter m_V

Some physically based criterions have been defined to constrain the possible parameter ranges:

- The crank angle where 50% of the fuel mass is burned must agree
- Because the experimental data could not been matched very well in the late combustion period the shape of the cumulative burn rates should agree until the combustion progress reaches 70%.

Based on the burn duration defined from experimental data the crank angles of combustion start and combustion end - required for the Vibe function - can be calculated by a set of two equations:

$$x_{B0.05} = 0.05 = 1 - e^{a \cdot \left(\frac{\varphi_{0.05} - \varphi_S}{\varphi_E - \varphi_S}\right)^{m_V + 1}}$$

$$x_{B0.9} = 0.9 = 1 - e^{a \cdot \left(\frac{\varphi_{0.9} - \varphi_S}{\varphi_E - \varphi_S}\right)^{m_V + 1}}$$

$$3.5$$

Solving equations 3.5 for $\varphi_E - \varphi_S$ leads to

$$\varphi_E - \varphi_S = \frac{\varphi_{0.9} - \varphi_{0.05}}{\left[\frac{\ln(1 - x_{B0.9})}{a}\right]^{1/(m_V + 1)} - \left[\frac{\ln(1 - x_{B0.05})}{a}\right]^{1/(m_V + 1)}} \qquad 3.6$$

The crank angle of combustion start can be calculated based on the first relation in equation 3.5.

$$\ln(1 - x_{B0.05}) = a \cdot \left(\frac{\varphi_{0.05} - \varphi_S}{\varphi_E - \varphi_S} \right)^{m_V + 1}$$

$$\varphi_S = \varphi_{0.05} - (\varphi_E - \varphi_S) \cdot \left(\frac{\ln(1 - x_{B0.05})}{a} \right)^{1/(m_V + 1)}$$

3.7

Finally, the overall Vibe parameter conversion can be described by normalising the dependencies with a known reference state. The model can be defined as follows:

$$\frac{\varphi_{ID}}{\varphi_{IDO}} = f_{rg} \cdot f_{st} \cdot f_{rpm} \cdot f_{bmep}$$

$$\frac{\varphi_{BD}}{\varphi_{BD0}} = g_{rg} \cdot g_{st} \cdot g_{rpm} \cdot g_{bmep}$$

3.8

$$\frac{m_V}{m_{V0}} = h_{rg} \cdot h_{st} \cdot h_{rpm} \cdot h_{bmep}$$

The effects of the residual gases - where the residual gases here are defined as the amount of exhaust gases due to the previous cycle plus the amount of exhaust gases coming from external EGR -, the spark timing, the engine speed and the engine load represented by the brake mean effective pressure are considered as the indices in equations 3.8 indicate.

This model formulation includes the assumption that the individual effects are independent. To eliminate the effect of the residual gases the conversion factors of engine speed, load and spark timing have been corrected by the amount of residual gases:

$$f_{st,\ rpm,\ bmep} = f_{st_{tot},\ rpm_{tot},\ bmep_{tot}} \cdot f_{rg}^{-1}$$

$$g_{st,\ rpm,\ bmep} = g_{st_{tot},\ rpm_{tot},\ bmep_{tot}} \cdot g_{rg}^{-1}$$

3.9

$$h_{st,\ rpm,\ bmep} = h_{st_{tot},\ rpm_{tot},\ bmep_{tot}} \cdot h_{rg}^{-1}$$

Starting from a reference state - where the Vibe parameters are known - the redefined combustion parameters can be determined with equations 3.8 and the functions summarised in the following table.

	residual gas [%]	spark timing [°BTDC]	engine speed [rpm]	bmep [bar]
f	$\dfrac{0.8932\,rg + 19.769}{0.8932\,rg_0 + 19.769}$	$\left(\dfrac{st}{st_0}\right)^{0.2287}$	$\left(\dfrac{rpm}{rpm_0}\right)^{0.3965}$	$\left(\dfrac{bmep}{bmep_0}\right)^{-0.0744}$
g	for rg<18.5% $\dfrac{0.9718\,rg + 26.279}{0.9718\,rg_0 + 26.279}$ for rg>18.5% $\dfrac{5.7535\,rg - 62.195}{5.7535\,rg_0 - 62.195}$	$\left(\dfrac{st}{st_0}\right)^{-0.46}$	$\left(\dfrac{rpm}{rpm_0}\right)^{0.3663}$	$\left(\dfrac{bmep}{bmep_0}\right)^{-0.1407}$
h	$\dfrac{-0.0829\,rg + 2.8187}{-0.0829\,rg_0 + 2.8187}$	$\left(\dfrac{st}{st_0}\right)^{0.8831}$	$\dfrac{-0.00036\,rpm + 2.3255}{-0.00036\,rpm_0 + 2.3255}$	$\left(\dfrac{bmep}{bmep_0}\right)^{0.1735}$

Table 3.1:   Experimentally determined conversion functions found for the empirical combustion model, f: ignition delay, g: burn duration, h: shape parameter

The conversion functions are visualised in figure 3.4 where the denotations of table 3.1 and equation 3.8 have been used.

The duration of the inflammation phase increases with increasing total amount of residual gases, increasing spark timing and increasing engine speed but decreases with increasing load as expected. It has to be taken into account that increasing spark timing means here by definition that ignition occurs earlier in the compression stroke. The temperatures and pressures are therefore lower for earlier spark timings.

In contrast to the ignition delay the burn duration decreases with earlier spark timings due to the higher temperatures and pressures during the combustion period near top dead centre. Slightly shorter burn durations for higher loads can be observed and combustion speed decreases for higher dilution and engine speeds. The behaviour as a function of the load may surprise first but in the engine this function is superposed by changing residual gas mass fractions and therefore the total ratio is a

combination of g_{bmep} and g_{st} (see equation 3.9). The residual gas mass fraction decreases for higher loads.
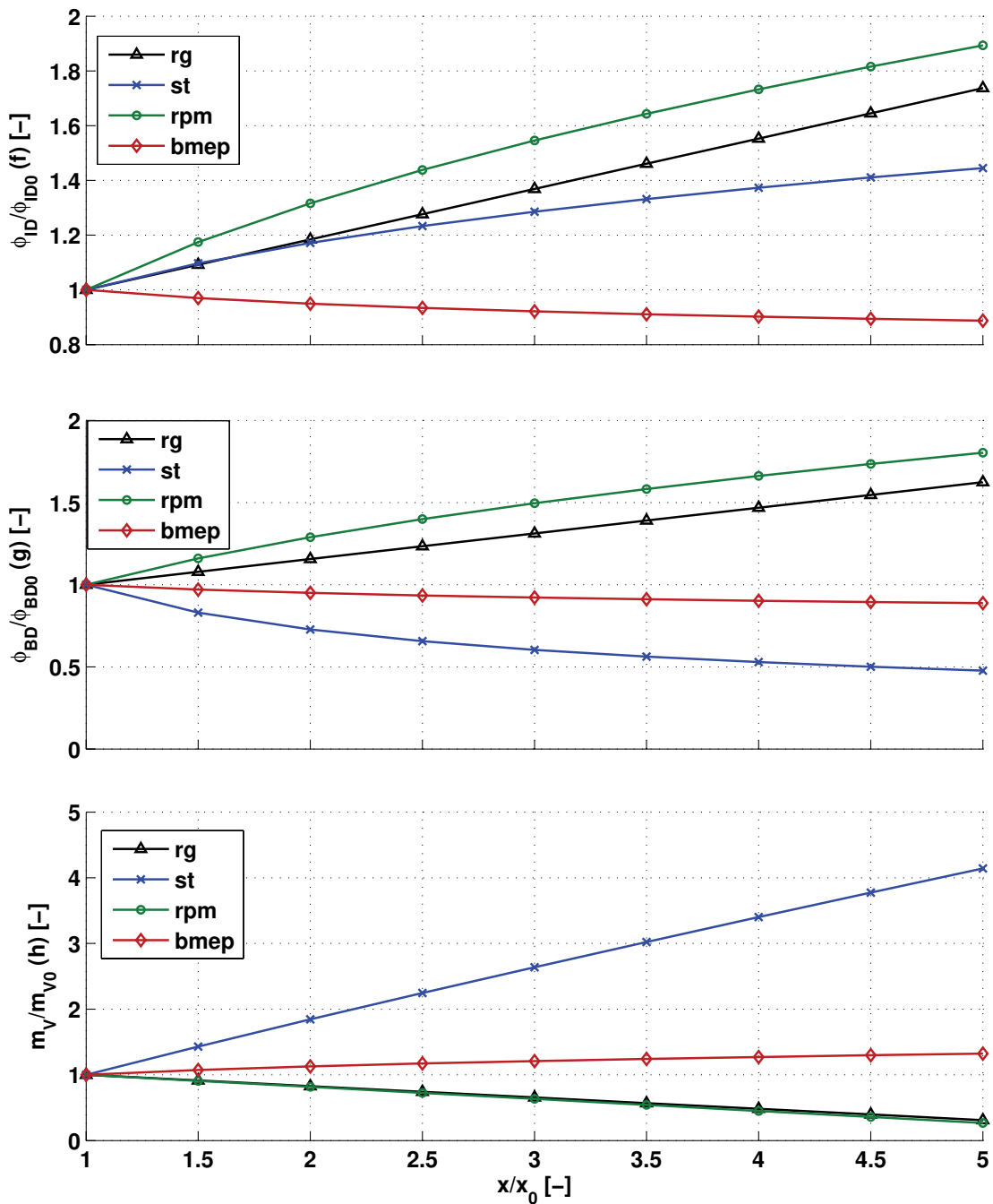

Figure 3.4:   Visualisation of the conversion functions found for the empirical combustion model according to table 3.1

The third graph shows that the shape parameter increases with earlier spark timing and increasing load whereas it decreases with increasing amount of residual gases and higher engine speeds - where these two curves superimpose in this diagram. A small shape parameter means that the burn rate is growing fast in the beginning while a slow burnout can be observed. Taking the dependence on spark timing as an example the burn rate increases fast in the first combustion period (small shape parameter) if spark ignition occurs late in the compression stroke - near top dead centre - due to the higher temperatures and pressures when combustion starts.

The parameter range x/x_0 in figure 3.4 was set to a very high value to cover a wide range of operating conditions. One possible reference point was used to develop the empirical model - and two more reference points have been tested in chapter 3.4 - where the engine speed was n=2000rpm and therefore the typical parameter range is between x/x_0=0.5 and x/x_0=3 for engine applications. For the „star point" chosen here - the „star point" is visualised in figure 3.1 - the brake mean effective pressure was bmep=2bar where x/x_0=5 is usual for naturally aspirated engines and has to be increased for turbocharged engines if no other reference point is chosen. The total amount of residual gas is around 10% for low speeds, low loads and no external EGR and the spark timing is approximately 30° and therefore x/x_0 is around 2 to 2.5. It is not recommended to choose the reference point at the outer boundaries of the engine map.

The validation of this model for ε=10.7 is described in chapter 3.4 and in chapter 3.5 the model was evaluated for different engine configurations (ε=13.5).

As denoted in chapter 1.2 this model has been used to test various strategies in the CEV-project. It should already be mentioned here that trends ca be reproduced well.

3.3 Phenomenological Combustion Model Formulation

In a phenomenological way the burn rate can be described by a propagating premixed flame front and is defined by the density of the unburned mixture ρ_U, the air to fuel ratio λAF_{ST} - with the stoichiometric air to fuel ratio AF_{ST} -, the turbulent flame speed S_T, the flame front area A_F, the expansion factor Ex and the lower heating value H_L:

$$\frac{dQ_B}{dt} = \frac{dm_F}{dt} \cdot H_L = \frac{\dot{m}_U}{1 + \lambda \cdot AF_{ST}} \cdot H_L = \frac{\rho_U}{1 + \lambda \cdot AF_{ST}} \cdot S_T A_F Ex H_L \qquad 3.10$$

Two parameters have to be modelled in this formulation. On one hand the turbulent flame speed has to be described and on the other hand the turbulent flame front area has to be modelled.

Due to the expansion of the burned gases the flame front propagates with a higher speed than the turbulent flame speed S_T. This is taken into account by the expansion factor Ex [54]:

$$Ex = \frac{\rho_U / \rho_B}{(\rho_U / \rho_B - 1) \cdot x_B + 1} \qquad 3.11$$

where ρ_B denotes the density of the burned mixture and x_B is the combustion progress variable.

3.3.1 Laminar and Turbulent Flame Speed Correlation

As shown in chapter 3.1 several correlations for the laminar flame speed for methane and for CNG exist. In this work the approach developed by Witt and Griebel [123] was used. The general form of their formulation is

$$S_L = c \cdot p_{cyl}^{-d} \qquad 3.12$$

This approach was extended by Liao's formulation for the influence of dilute gas [73] where rg_{Vol} denotes the total (internal and external) amount of volumetric residual gas in the combustion chamber.

$$S_L = c \cdot p_{cyl}^{-d} \cdot (5.4825 \cdot rg_{Vol}^2 - 4.1988 \cdot rg_{Vol} + 0.9952) \qquad 3.13$$

The coefficients are divided in a low and a high pressure part. In the range of $1bar < p_{cyl} < 7bar$ the coefficients are defined as

$$c = (-1.03 \cdot 10^{-2} T_u + 3.645) \cdot \Phi^2$$
$$+ (-4.12 \cdot 10^{-6} T_u^2 + 2.512 \cdot 10^{-2} T_u - 7.68) \cdot \Phi$$
$$+ (8.78 \cdot 10^{-6} T_u^2 - 1.547 \cdot 10^{-2} T_u + 4.19) \tag{3.14}$$

$$d = 7.5 \cdot 10^{-1} \Phi^2 - 1.6 \cdot \Phi + 1.337 - 2 \cdot 10^{-4} T_u$$

T_u denotes the temperature of the unburned mixture, p_{cyl} is the cylinder pressure and Φ is the equivalence ratio.

For higher pressures the coefficients are defined as follows

$$c = (-6.906 \cdot 10^{-5} T_u^2 + 6.875 \cdot 10^{-2} T_u - 25.13) \cdot \Phi^3$$
$$+ (1.155 \cdot 10^{-4} T_u^2 - 1.1523 \cdot 10^{-1} T_u + 46.47) \cdot \Phi^2$$
$$+ (-4.185 \cdot 10^{-5} T_u^2 + 4.922 \cdot 10^{-2} T_u - 24.82) \cdot \Phi \tag{3.15}$$
$$+ (6.57 \cdot 10^{-6} T_u^2 - 9.55 \cdot 10^{-3} T_u + 5.185)$$

$$d = 0.45$$

The laminar flame speed model developed by Witt and Griebel was tested up to T_U=850K, where all other models have been developed for temperatures up to T_U=550K or have been extended to T_U=650K. The flame speed is more sensitive to temperature than to pressure. In the engine used here, T_U goes up to 1000K and therefore, this formulation seemed to be meaningful.

In this study Gülder's approach [52] for the turbulent flame speed was used:

$$\frac{S_T}{S_L} = 1 + A_G \cdot \left(\frac{u'}{S_L}\right)^{n_{ST}} \cdot Re_T^{m_{ST}} \tag{3.16}$$

In the formulation of the turbulent Reynolds number the viscosity of the unburned mixture $\eta(T_U)$ was described according to [62]:

$$Re_T = \frac{u' \cdot li \cdot \rho_U}{\eta(T_U)} \ and \ \eta(T_U) = \frac{\sum_{i=1}^{n} V_i \eta_i(T_U) \sqrt{M_i T_{crit,i}}}{\sum_{i=1}^{n} V_i \sqrt{M_i T_{crit,i}}} \qquad 3.17$$

with V_i=Partial volume of component i, M_i=Molecular weight of component i, $T_{crit,i}$=Critical temperature of component i, $\eta_i(T_U)$=Viskosity of component i taken from GT-Power.

3.3.2 Turbulence Model

The turbulence intensity u' was calculated from a one equation energy balance for the turbulent kinetic energy, where the turbulence production due to compression k_{comp}, the dissipation k_{diss}, the turbulence production due to the squish flow k_{squish} and the intake flow k_{intake} are considered.

$$\frac{dk}{dt} = \frac{dk_{comp}}{dt} - \frac{dk_{diss}}{dt} + \frac{dk_{squish}}{dt} + \frac{dk_{intake}}{dt} \qquad 3.18$$

A detailed description of the turbulence model can be found in appendix A.1. For this application isotropic homogenous turbulence is assumed. Therefore, the turbulence intensity u' can be expressed as

$$k = \frac{1}{2} \cdot (u'^2_x + u'^2_y + u'^2_z) = \frac{3}{2} \cdot u'^2 \rightarrow u' = \sqrt{\frac{2}{3}k} \qquad 3.19$$

The turbulent integral length scale - which characterises a typical size of an eddy - was calculated from the conservation of mass (see equation A.1.1 in the appendix) by assuming that l_i is equal to the diameter of one eddy. The density at inlet valve close was used as reference and a multiplier K_{li} has been introduced. For the densities used in equation 3.20 the mean values - meaning that $\rho = m_{cyl}/V_{cyl}$ - have been applied.

$$l_i = K_{li} \cdot \left(\frac{\rho_{IVC}}{\rho}\right)^{1/3} \qquad 3.20$$

3.3.3 Determination of the Flame Front Area

In this study, experimentally determined burn rate curves are used as input parameters. This allows deriving a flame front area by reversing equation 3.10:

$$A_F = \frac{dQ_B/dt \cdot (1 + \lambda \cdot AF_{ST})}{\rho_U \cdot S_T \cdot Ex \cdot H_L} \qquad 3.21$$

In figure 3.5 the calculated flame front area for a variation of the spark timing is shown. Furthermore, the dashed line characterises the maximum flame front areas A_{FMax} calculated from

$$A_{FMax} = A_{FMaxTDC} \cdot K_{CorrA_F} = A_{FMaxTDC} \cdot \left(\frac{V_{cyl}}{V_{TDC}}\right)^{n_{vol}} \qquad 3.22$$

The crank angle dependent exponent n_{vol} - displayed in the upper part of figure 3.5 - considers the different timings of the flame impingement on the piston due to the changing volume.
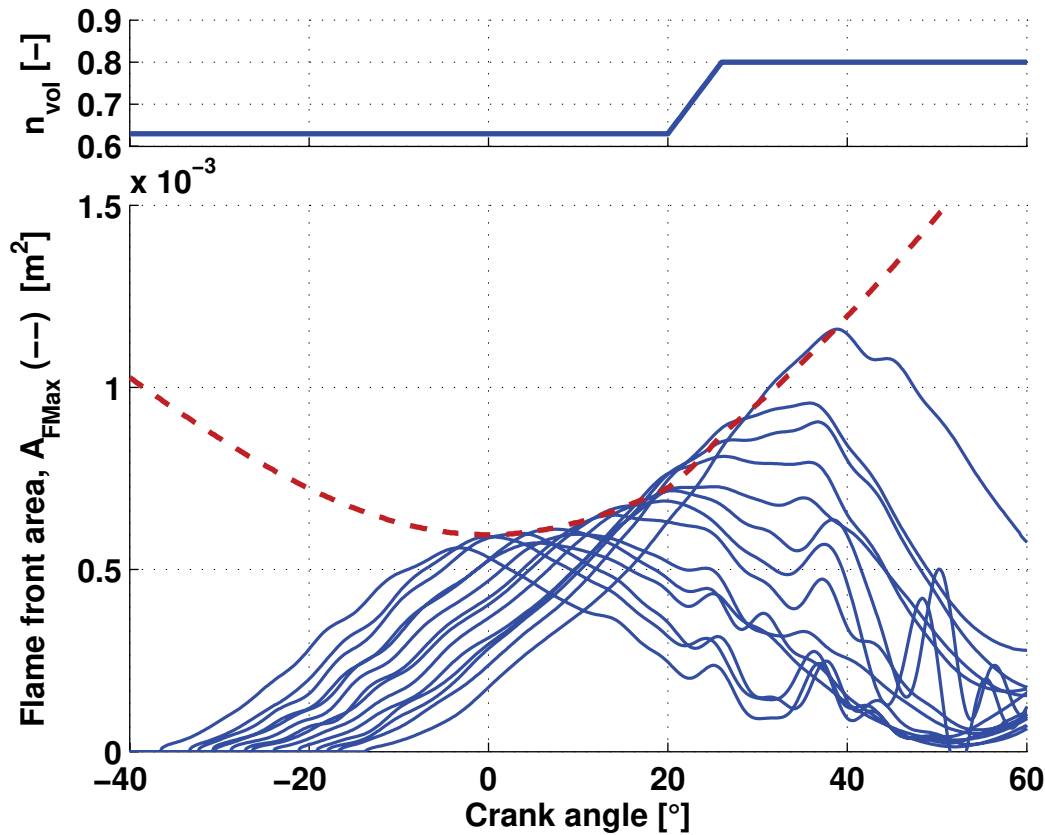
Figure 3.5:   *Flame front area for a variation of spark timing, n=2000rpm, bmep=2bar, ε=10.7*

It can be seen that the flame front area depends on the crank angle due to interaction between the flame and the combustion chamber walls. Moreover, it can be observed that if spark timing occurs late, the flame front area increases due to increasing cylinder volume. In this case, the flame-wall interaction takes place later in the expansion stroke. Furthermore, the shape of the flame changes due to piston movement what is taken into account by K_{CorrAF} .

Based on the development illustrated by Koch [66] a characteristic shape of the flame front area curves can be defined. By dividing each of the flame front areas shown in figure 3.5 with the correction factor K_{CorrAF} (equation 3.22) - which means that each of the flame front areas is related to the same piston position - and plotting these corrected flame front areas as a function of the combustion progress variable x_B, the characteristic mean flame front area can be derived:

Figure 3.6:   Corrected flame front areas and characteristic mean flame front area as a function of the combustion progress variable x_B for the same conditions as in figure 3.5, ε=10.7

The final formulation of the flame front area used for the cycle simulations presented later is defined as follows

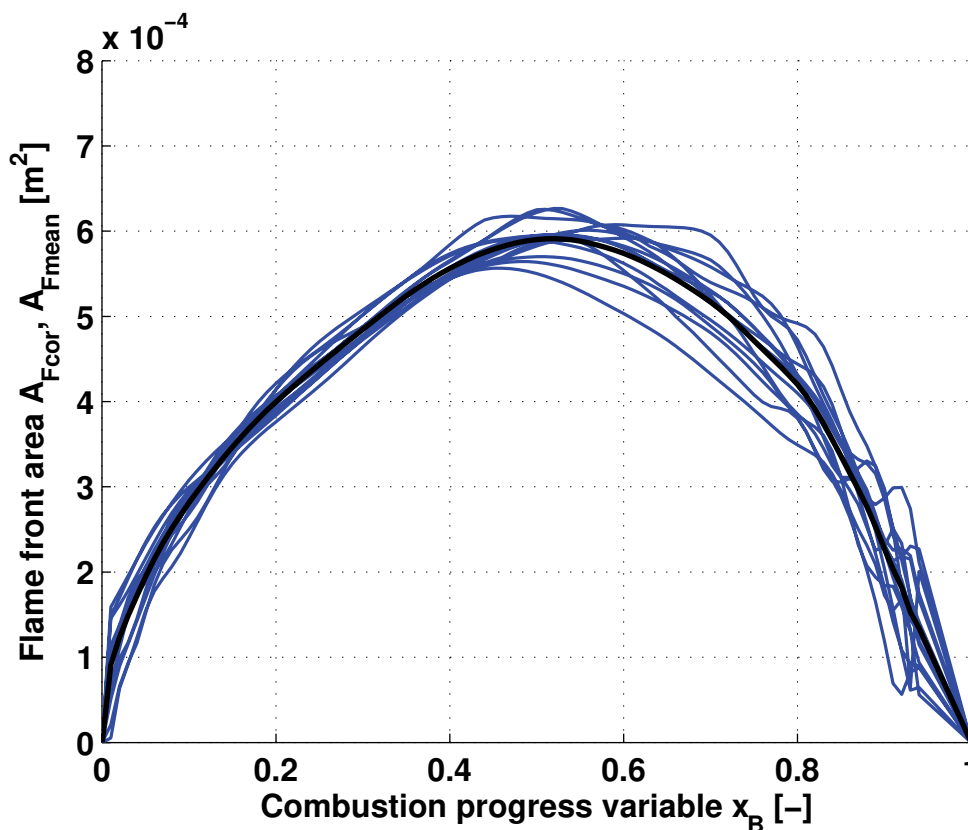$$A_F(\varphi) \ = \ A_{Fmean} \cdot K_{CorrA_F} = A_{Fmean} \cdot \left(\frac{V_{cyl}}{V_{TDC}}\right)^{n_{vol}} \qquad 3.23$$

The characteristic mean flame front area was stored in a text file and has been read in every time step.

It has to be mentioned here, that for the determination of the flame front area the crank angle range starts at inlet valve close and ends at exhaust valve open, because experimentally determined burn rate curves have been used as source. Therefore, the turbulent kinetic energy at start of compression has to be estimated (see equation A.1.23 in appendix A.1).

3.3.4 Inflammation Phase

During the inflammation phase the flame propagates with a speed which is first of the order of the laminar flame speed and increases up to the turbulent flame speed then. In the beginning the flame radius is smaller than the eddy size and therefore it is assumed that the turbulence does not wrinkle the flame front. As the flame radius increases the effect of turbulence becomes more important. It is assumed that when the flame radius reaches a critical value turbulent flame propagation is established.

To consider this transition the inflammation phase has been modelled separately. To initiate the flame propagation it is assumed that in the first time step after ignition a sphere with a corresponding diameter of 1mm is burned instantaneously. The growth of the flame radius as a function of time was defined as

$$r_{flame}(t_2) \ = \ r_{flame}(t_1) + K_{ignsturb} \cdot S_T \cdot (t_2 - t_1) \qquad 3.24$$

where $K_{ignsturb}$ denotes a turbulent flame speed multiplier and S_T is the turbulent flame speed. In this formulation the inflammation phase is coupled with the turbulent flame speed - and therefore indirectly coupled with the operating conditions - leading to accurate predictions of the burn rate in the early combustion period for a wide range of operating conditions.

As long as the following inequality is fulfilled, the combustion remains in the inflammation phase.

$$r_{flame}(t) < K_{ignli} \cdot li(t) \qquad 3.25$$

During the inflammation phase the flame front area is defined based on the radius shown in equation 3.25. For the fully established turbulent flame, the characteristic mean flame front area defined in equation 3.23 is used.

3.4 Empirical Combustion Model Validation

To test the empirical model 18 operating points have been chosen which are specified in the following table. Most of the operating points chosen can be found during a cycle test. Furthermore, full load performance - denoted by FL in the table - was tested. The first nine points are with EGR, operating points eleven to eighteen are without EGR. The spark timing varies for each of the investigated operating point.

Number of operating point	Engine speed [rpm]	BMEP [bar]	Spark timing [° BTDC]	EGR rate [%]
1	2000	2	36	0
2	2000	5	30	0
3	2000	7.7 (FL)	30	0
4	3000	2	38	0
5	3000	5	32	0
6	3000	8.5 (FL)	30	0
7	4000	2	44	0
8	4000	5	36	0
9	4000	8.3 (FL)	26	0
10	2000	2	50.25	10.5
11	2000	3	45	12.9
12	2000	4	39.75	10.6
13	3000	2	48.75	8.5
14	3000	3	42	8.5
15	3000	4	40.5	8.7
16	4000	2	46.5	8.3
17	4000	3	45	12.6
18	4000	4	44.25	12.2

Table 3.2:   Operating points used for the empirical combustion model validation, $\varepsilon=10.7$

The first nine operating points represent the typical driving range in a test cycle where the range has been extended to full load operating condition. Here, a variation of the engine load at constant engine speed on one hand and on the other hand a variation of the engine speed at constant load can be investigated. For bmep=2bar the transition from non-EGR to EGR operation can be examined. The spark timing had to be adjusted for every single operating point.

Based on the experimentally determined cumulative burn rate curves the crank angle at 5% burned, the crank angle at 50% burned and the burn duration defined as 5% to 90% burned have been compared. Furthermore, the model formulation shown in table 3.1 indicates that the results may depend on the reference state whereas this effect was investigated by testing three operating points as reference.

The reference operating conditions are summarised in the following table:

Reference point	Engine speed [rpm]	BMEP [bar]	Spark timing [° BTDC]	Residual gas [%]	EGR rate [%]
2000/2	2000	2	48.75	18.8	10.5
3000/3	3000	3	34.5	7.5	0
4000/5	4000	5	45	15.1	11.2

Table 3.3: Reference operating conditions used for the empirical combustion model validation, ε=10.7

Before the results will be discussed, it should be mentioned that the determination of the EGR rate by measuring the CO_2 concentration in the intake manifold was quite uncertain for this small engine. While turning on the exhaust gas analyser, the throttle angle had to be adjusted to keep the brake mean effective pressure due to the analyser to engine mass flow ratio. This effect could be observed especially for low load operating conditions.

Figure 3.7 shows the comparison between experiment and calculation for the crank angle at 5% burned where the curve is interrupted to separate the non-EGR and the EGR operating points.

As mentioned before the results depend on the chosen reference point. The denotation in the legend consists of two numbers. The first indicates the engine speed

in rpm and the second the brake mean effective pressure in bar. For all these calculations the trends agree very well, whereas the variations and the differences increase for the operating points with EGR. It can be seen that the inflammation phase is too long for the 2000/2 reference operating conditions where for the 3000/3 and the 4000/5 reference operating conditions good agreements are observed. The ignition delays are slightly too short for most of the operating points investigated, if reference operating conditions 3000/3 or 4000/5 are applied. The transition from non-EGR to EGR operation can be reproduced quite well.

Figure 3.7:   *Experimentally determined and calculated crank angle at 5% burned for the operating points listed in table 3.2 using the reference operating conditions listed in table 3.3, $\varepsilon=10.7$*

It is noticeable that the best results have not been obtained with the reference operating conditions (2000/2) which is almost equal to the „star point" (2000/2) where the model was built up. This observation indicates that the choice of the reference operating conditions is more important than the choice of the „star point".

Figure 3.8 shows the results for the burn duration where the trends again agree very well for the operating points without EGR and quite well for the non-EGR

operating points. By comparing the reference operating conditions it can be noticed, that the differences increase if EGR is turned on.

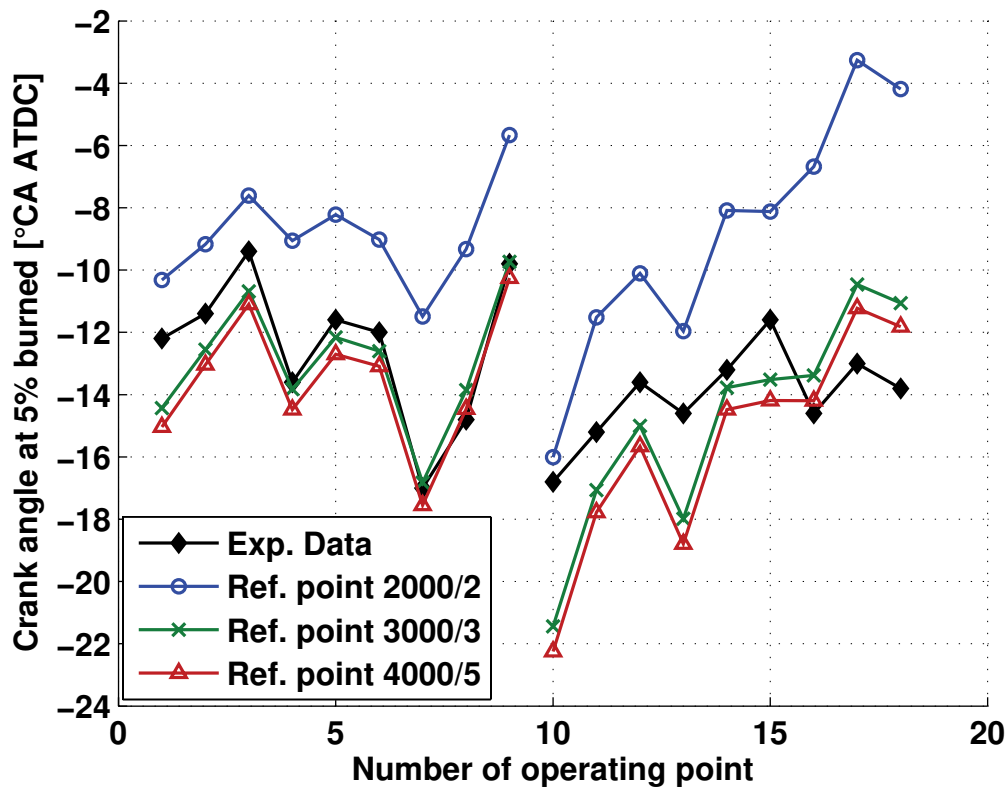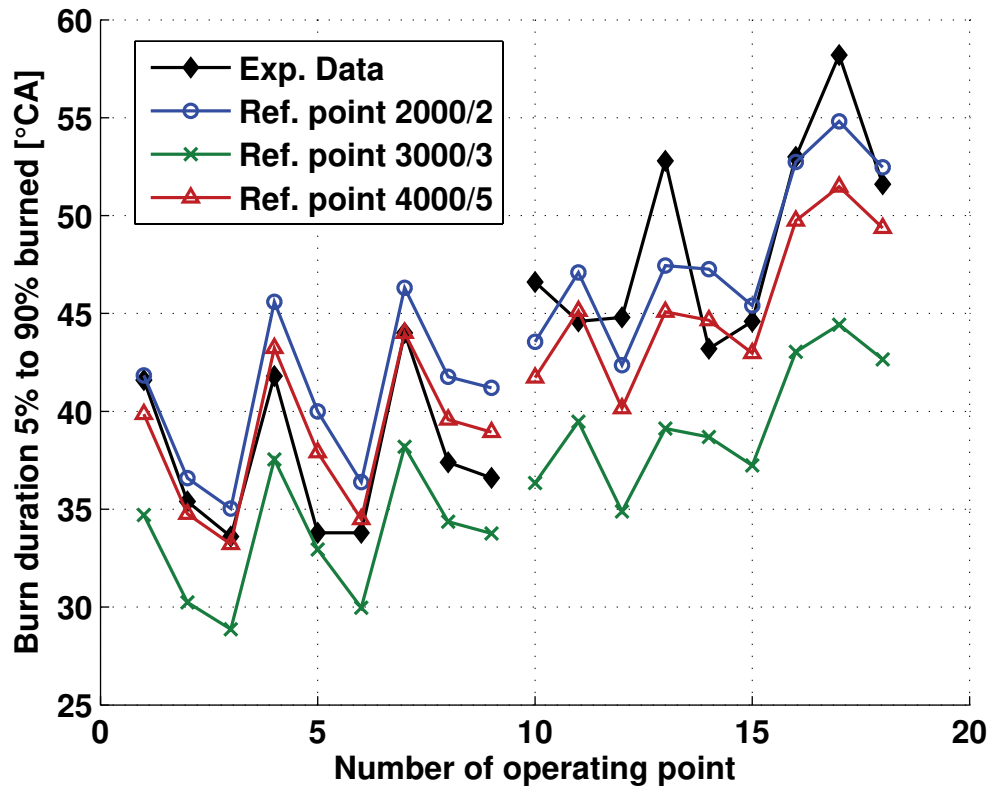*Figure 3.8:   Experimentally determined and calculated burn duration for the operating points listed in table 3.2 using the reference operating conditions listed in table 3.3, ε=10.7*

In contrast to the crank angle at 5% burned, the burn duration is too short for all the investigated operating points if the 3000/3 reference operating conditions and in most cases too long if the 2000/2 reference operating conditions is used. The 4000/5 reference operating conditions seem to be the best compromise. A shift can be observed if comparing the EGR cases with the non-EGR cases where in general the calculations result in too short burn durations.

A similar behaviour was found for the crank angle at 50% burned. It has to be considered that these differences are a consequence of the variations of the crank angle at 5% burned and the variations of the burn duration because no explicit formulation for the crank angle at 50% burned is used in this model. Nevertheless, the trends agree quite well, where most of the operating points are within a difference

of 6° crank angles. Again, good agreements between experiments and the 4000/5 reference point can be observed.

The results shown in figure 3.9 correspond well to the crank angle at 5% burned and the burn duration. Taking operating point 10 as an example the crank angle at 50% burned occurs too early for the 3000/3 and the 4000/5 reference operating conditions, the inflammation phase and the burn duration are too short. For the 2000/2 reference operating conditions the crank angle at 5% burned and the burn duration agree well resulting in a good prediction for the crank angle at 50% burned.
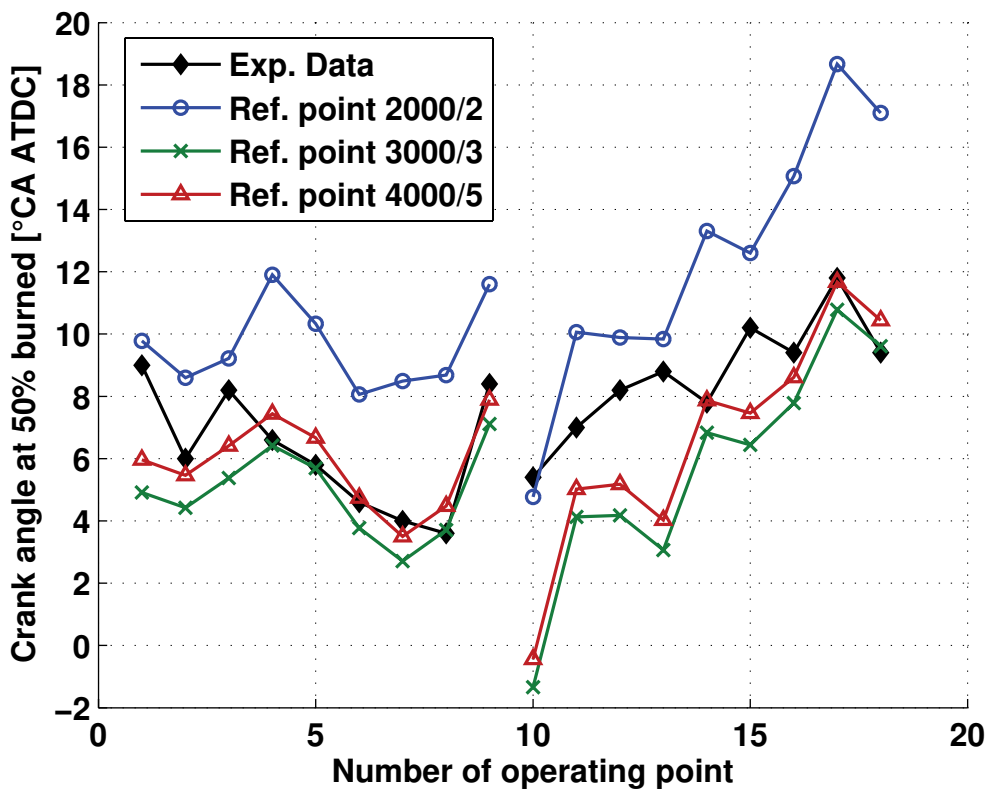
Figure 3.9:   *Experimentally determined and calculated crank angle at 50% burned for the operating points listed in table 3.2 using the reference operating conditions listed in table 3.3, $\varepsilon = 10.7$*

The sensitivity of the selected reference operating conditions may be found if the dependencies on the engine parameters are examined. The following diagram shows the experimentally determined burn durations as a function of the engine speed. Furthermore, the resulting burn durations are plotted if the three reference

operating conditions are applied. These burn durations are independent of the chosen brake mean effective pressure, in general.

If n=2000rpm is applied as reference operating conditions, the burn duration will be too long for all other engine speeds, whereas it will be too short if n=3000rpm is chosen. As the results shown before indicate, n=4000rpm seems to be the best compromise.
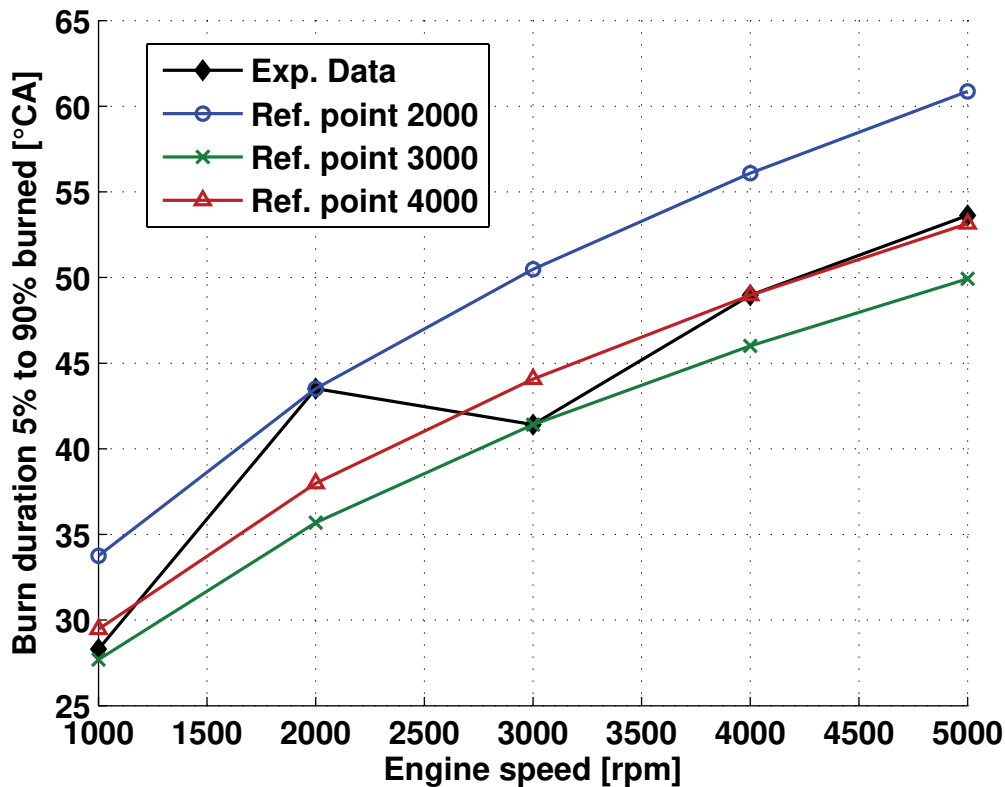
Figure 3.10: Burn duration as a function of engine speed (g_{rpm}) and sensitivity to the reference operating conditions

This sensitivity may be the reason for the results illustrated in figure 3.8. It has to be considered, that the resulting Vibe parameters are a product of different dependencies (equation 3.8). Similar sensitivities have been found for the ignition delay.

The fluctuations of the burn duration as a function of the engine speed have been confirmed by several measurements where the engine speed has been varied at different brake mean effective pressures.

Finally, figure 3.11 compares the indicated mean effective pressure. Most of the investigated operating points are within an acceptable difference, excluding operating point number 13. For test number 13 it is assumed, that the experimentally determined EGR rate is too low where the behaviour of the crank angle at 5% burned, of the crank angle at 50% burned, the burn duration and the air mass flow rate confirm this assumption.
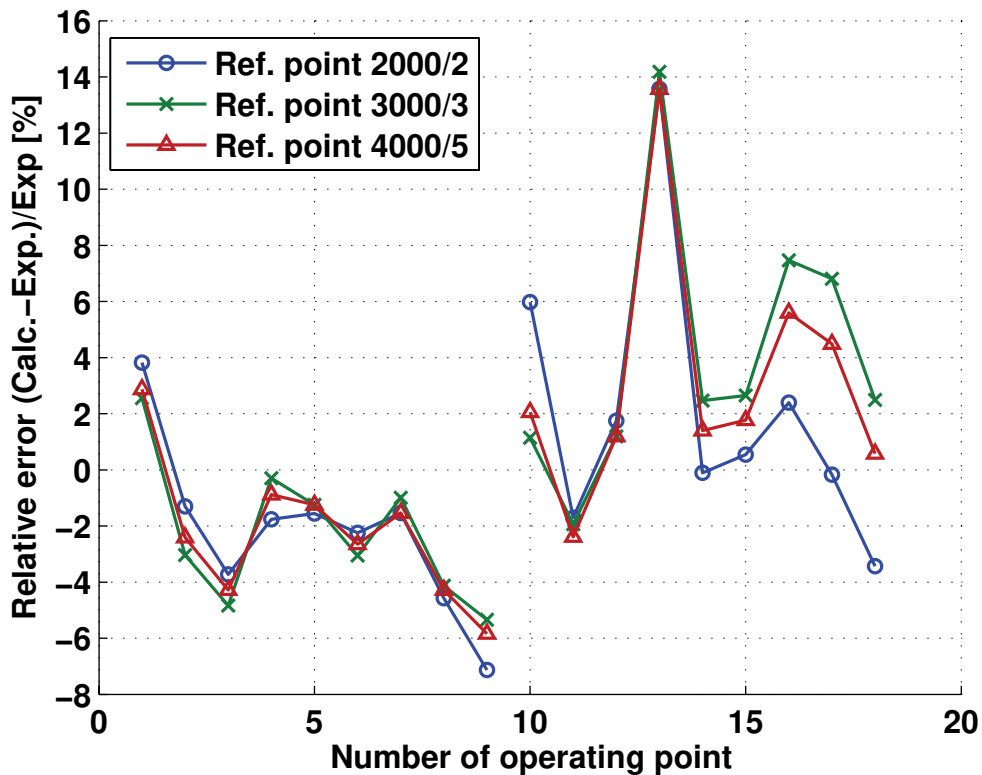
Figure 3.11: Relative error for the indicated mean effective pressure according to the simulations and to experimental data for the operating points listed in table 3.2 using the reference operating conditions listed in table 3.3, ε=10.7

One possibility to improve the empirical combustion model is to use more than one „star point" in the engine map. In this case, more fluctuations in engine operation can be taken into account and a mean formulation over the „star points" used is possible. This investigation was not carried out in this work.

3.5   Evaluation of the Empirical Combustion Model for Different Combustion Chamber Designs

The capabilities and limitations of the developed empirical combustion model have been investigated by applying the model to engine configuration 3 (ε=13.5). Therefore, 30 operating points - listed in appendix A.2 - have been chosen and analysed. It has to be taken into account that for this new engine configuration the conditions in the combustion chamber will change. As an example, the temperatures and pressures during the combustion period will increase, whereas the residual gas mass fraction will decrease, in general. The temperatures and pressures in the combustion chamber are not explicitly considered in the model formulation.

The first ten operating points are without EGR, where some of them lie at the boundaries of the engine map. Points eleven to thirty are with EGR and represent the typical driving range of the CEV-engine during the cycles tested (NEDC, FTP-75). The following diagram shows the results obtained for the crank angle at 5% burned.
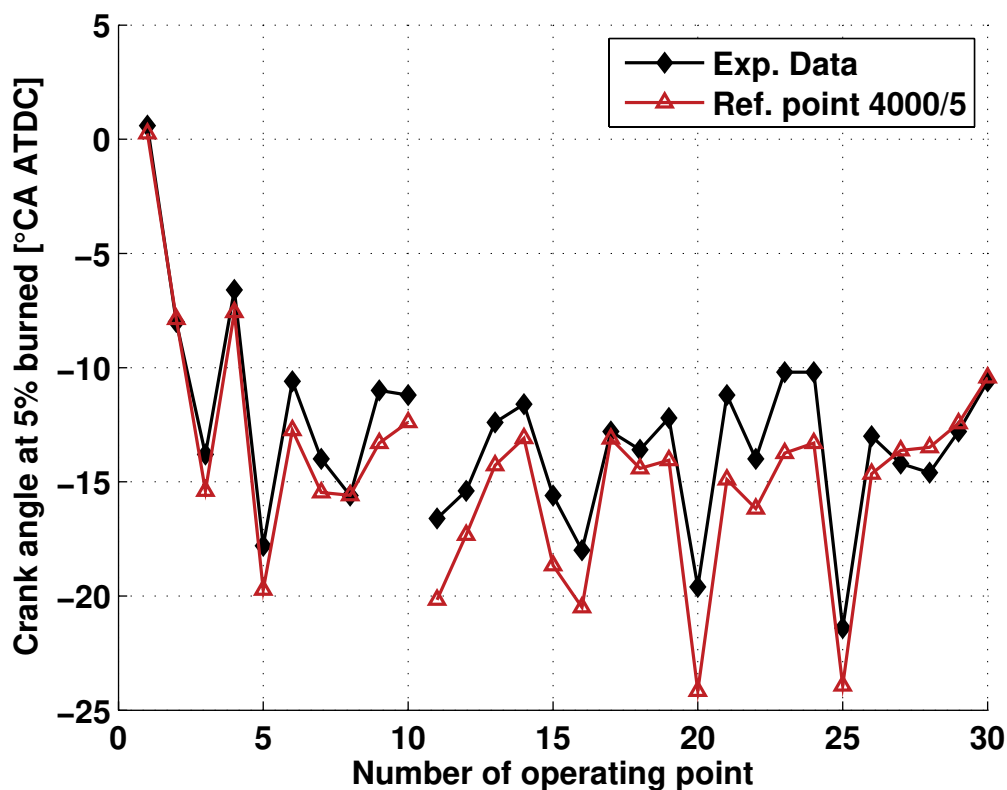

Figure 3.12:   Experimentally determined and calculated crank angle at 5% burned for the operating points listed in appendix A.2, ε=13.5

The agreement between experimentally determined and calculated ignition delays is quite well, although the conditions for the new engine configuration at spark timing are not explicitly considered in the model formulation. Most of the computed operating points have a shorter inflammation phase than experimentally observed but the trends can be reproduced very well.

The burn durations are compared in figure 3.13. All calculations indicate much shorter burn durations than the experiments do. One reason for this behaviour could be the flame impingement on the piston which is not taken into account in the model here. The flame impingement will be discussed in chapter 3.7. Operating point 7 shows a very long burn rate and is one of the mentioned „extreme values“ (n=2500rpm, bmep=1bar) where small uncertainties in the experiment and in the simulation result in large differences.
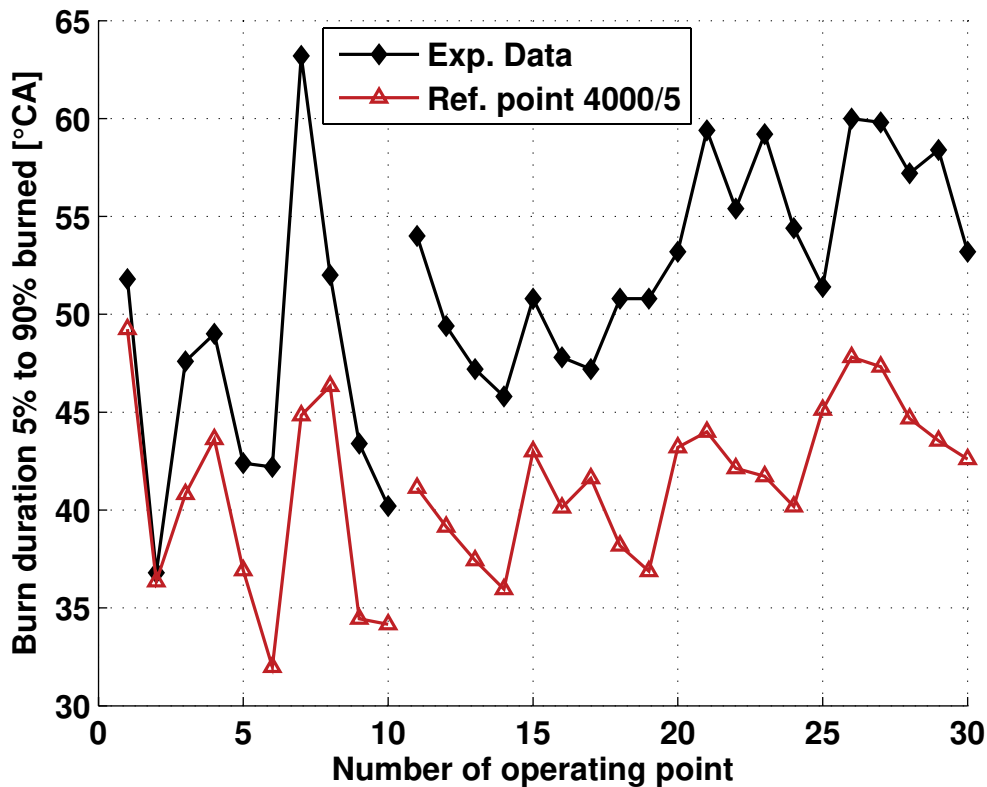

Figure 3.13: Experimentally determined and calculated burn duration for the operating points listed in appendix A.2, ε=13.5

The crank angles at 50% burned shown in figure 3.14 are again a result of the ignition phase and the burn duration and correspond well to the results obtained. Most of the calculated crank angles at 50% burned occur too early in the simulation,

but the trends can be reproduced quite well. The differences between experiment and simulation again increase when EGR is turned on.
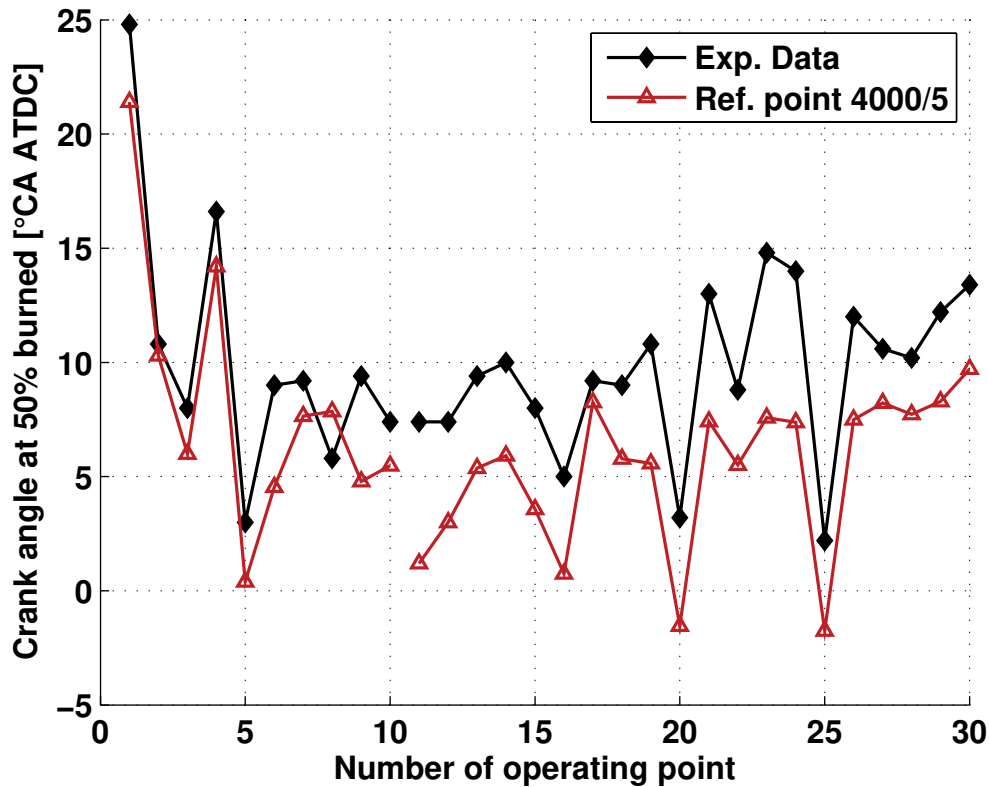
Figure 3.14: Experimentally determined and calculated crank angle at 50% burned for the operating points listed in appendix A.2, ε=13.5

The use of the empirical combustion model for different engine configurations indicated that trends can be reasonably predicted, in general. The absolute values differ as the differences between experiment and simulation show. It has to be taken into account that this model is not based on explicit physical formulations.

Two possibilities to improve the model for different combustion chamber designs can be figured out. Some of the conversion functions shown in table 3.1 may be replaced by new ones. As a consequence some single conversion functions would have to be redefined if the engine setup changes. On the other hand a conversion function for different combustion chamber geometries may be introduced to take into account the new geometrical conditions.

In this work, the phenomenological model was preferred for this application.

3.6   Phenomenological Combustion Model Validation

The phenomenological combustion model was validated for the ε=10.7 configuration. The 18 operating points already used for the validation of the empirical combustion model - and listed in table 3.2 - have been used in order to test the phenomenological combustion model.

The model parameters described in chapter 3.3 and used for the simulations are summarised in the following table:

Model parameter	Unit	Equation	Value
A_G	--	3.16	0.62
n_{ST}	--	3.16	0.5
m_{ST}	--	3.16	0.25
K_{li}	m	3.20	0.002
n_{Vol}		3.23	$0.63 \quad for \quad CA \leq 20$ $0.0283 \cdot (CA - 20) + 0.63 \quad for \quad 20 < CA < 26$ $0.8 \quad for \quad 26 \leq CA$
$K_{ignsturb}$	--	3.24	0.06
K_{ignli}	--	3.25	1

Table 3.4:   Model parameters used for the phenomenological combustion model

The parameters used for the turbulent flame speed have been taken from Gülder [52]. K_{li} is used for the determination of the integral length scale and therefore affects the turbulence intensity and additionally the inflammation phase. It is known that turbulence intensity in IC engines is about half of the mean piston speed at top dead centre [15] and therefore, K_{li} was varied to meet this value. Here, a typical eddy size is 2mm at inlet valve close. The range of n_{vol} has been shown in figure 3.5. $K_{ignsturb}$ was varied to match experimental data, has been first investigated

for one operating point and was transferred to the other operating points. Good results have been obtained using K_{ignli}=1.

The formulation of the inflammation phase seems to be meaningful as indicated by figure 3.15. The trends agree qualitatively and quantitatively well. It is important to have a reasonable formulation for the inflammation phase due to its influence on the entire combustion behaviour [14, 63, 88]. The transition from non-EGR to EGR operation can be reproduced very well. For operating point 1 and 10 the differences increase which is in agreement with the observations made for the empirical combustion model. The differences here are within 3° crank angle.

Figure 3.15: Experimentally determined and calculated crank angle at 5% burned for the operating points listed in table 3.2, ε=10.7

In contrast to the observations made for the empirical combustion model, where the burn duration was modelled, the burn durations shown in figure 3.16 as well as the crank angles at 50% burned shown in figure 3.17 are a consequence of the submodels described in chapter 3.3 in the phenomenological case.

Some of the investigated operating points show a too short and some show a too long burn duration where the differences are within an acceptable range. Again, the transition from non-EGR to EGR operation can be reproduced well indicating that - together with figure 3.15 - the laminar flame speed can be well approximated. Moreover, it can be observed that the trends are much smoother for the simulations.

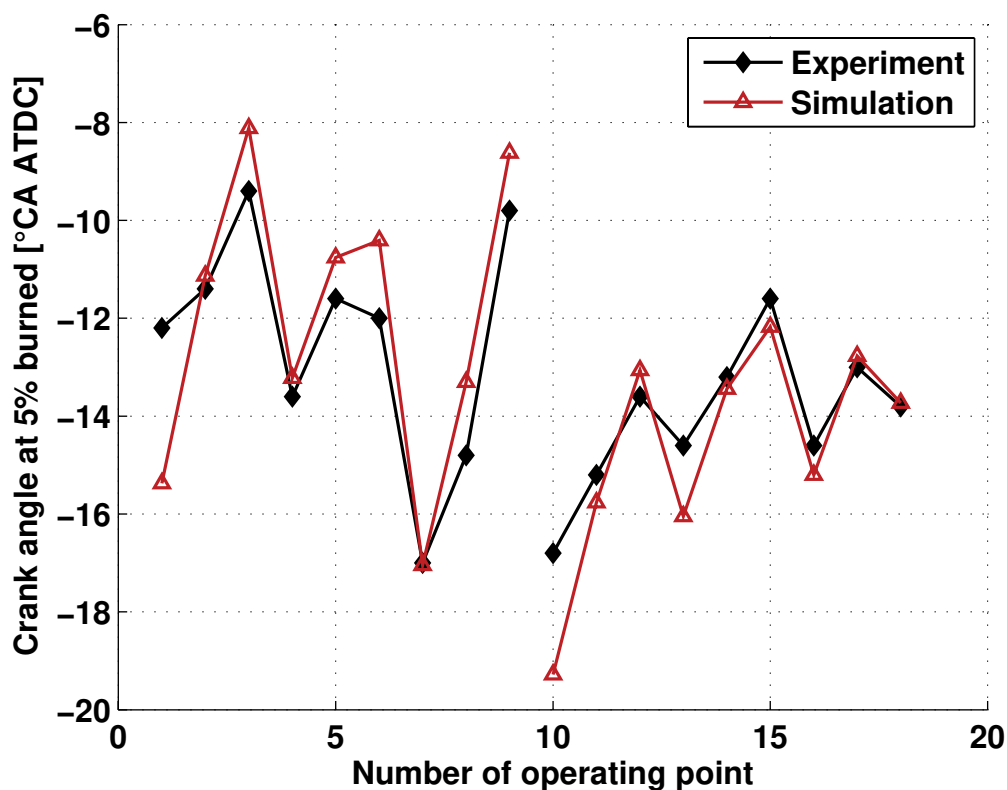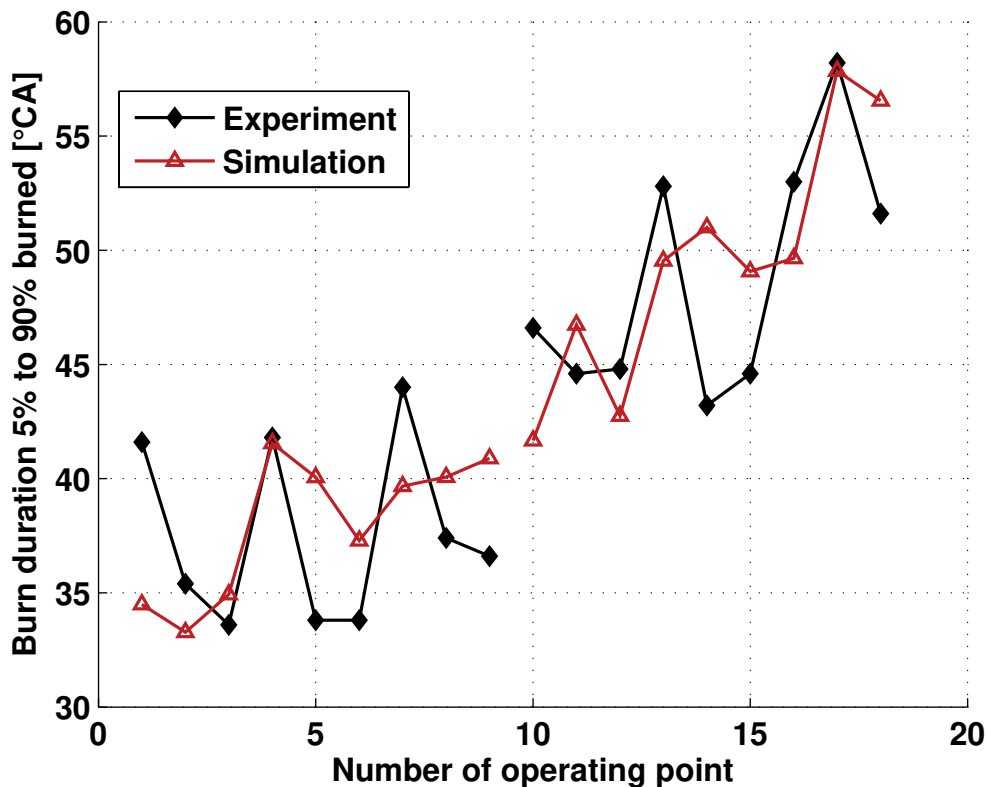*Figure 3.16: Experimentally determined and calculated burn duration for the operating points listed in table 3.2, ε=10.7*

Based on figure 3.15 and figure 3.17 it can be seen that operating point number 1 has a too short ignition delay which leads to part of the early crank angle at 50% burned. The too short burn duration may be a consequence of the inflammation phase or may occur due to inaccurate model formulations. For operating point number 14 in contrast the crank angle at 5% burned agrees very well but the burn duration is too long which leads to a late crank angle at 50% burned. The differences between simulation and experiment for the crank angle at 50% burned are within 3° crank angle, excluding operating point 1 and 10.

The validation of the phenomenological combustion model showed that the physically based formulation is more sensitive to experimental inaccuracies than the

empirical model. Some of the experimentally determined burn rate curves show a slightly negative value before spark occurs leading to deviations in the parameters (crank angle at 5% burned, crank angle at 50% burned, burn duration) investigated here. Furthermore, the determination of the characteristic mean flame front area is an indicator for the quality of the experimental data and, of course, for the model formulation. These experimental uncertainties are included in the empirical combustion model case.
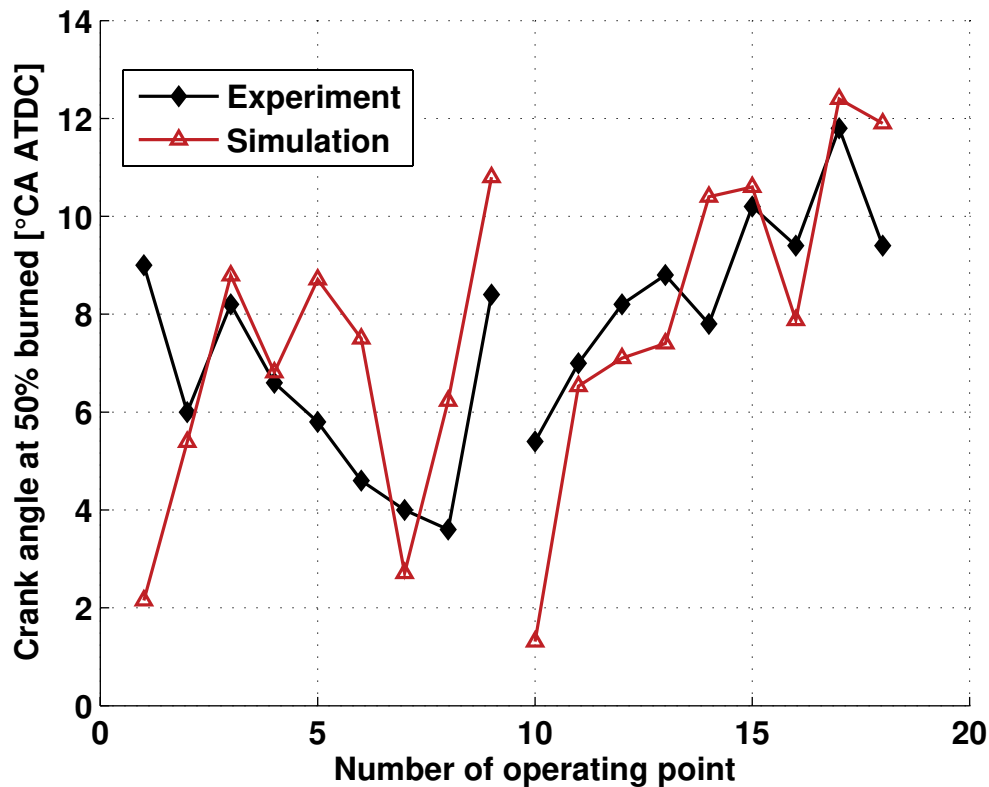

Figure 3.17: Experimentally determined and calculated crank angle at 50% burned for the operating points listed in table 3.2, ε=10.7

The general trends and the absolute values can be reproduced well using the phenomenological combustion model and in addition a lot of information can be extracted as it will be shown in the following chapters.

3.7 Combustion Analysis Using the Phenomenological Combustion Model

The phenomenological model was employed in order to learn more about the combustion behaviour for the two combustion chamber designs used in this work. The high compression ratio was realised by using flat pistons, whereas the original pistons with bowl have been replaced.

In figure 3.18 the experimentally determined burn rate and the cumulative burn rate curves are compared for n=3000rpm and bmep=4bar (3000/4 operating point). The engine speed, the spark timing and the brake mean effective pressure are identical for both configurations. As expected, the inflammation phase is shorter for the ε=13.5 case due to the higher temperature and pressure and burns faster in the early combustion period. The burning speed seems to decrease at about 10° crank angle after top dead centre and finally the higher compression ratio case burns slower.
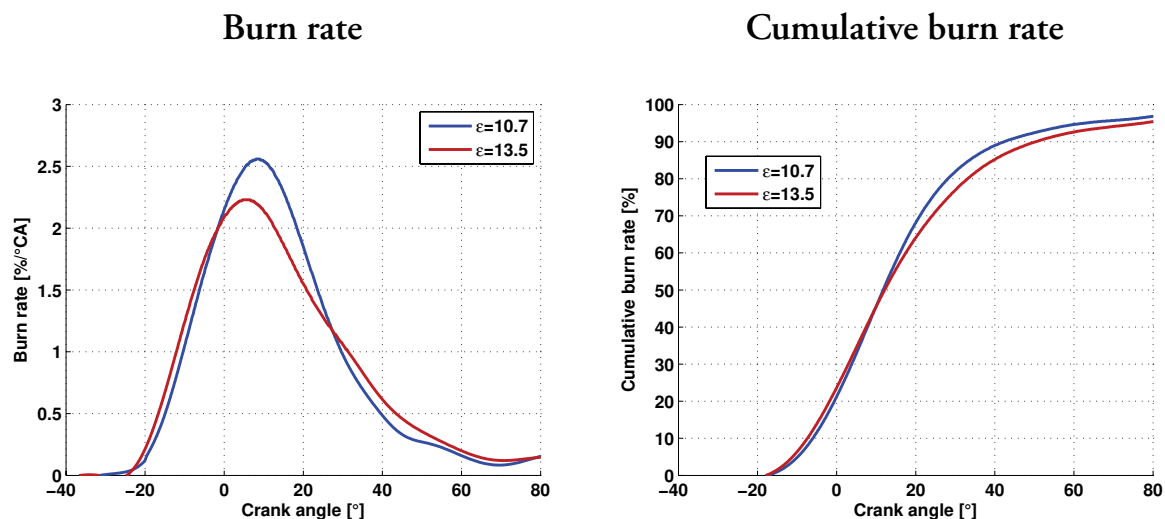
Figure 3.18: Burn rate and cumulative burn rate curves (experiment) for n=3000rpm, bmep=4bar, spark timing=40°CA BTDC, ε=10.7 and ε=13.5

The analysis of the laminar and the turbulent flame speeds and the turbulence intensity showed no mentionable differences and therefore, equation 3.21 was applied to model the flame front area in the new configuration (ε=13.5). Figure 3.19 compares these flame front areas for both combustion chamber designs. Due to the smaller combustion chamber volume the flame front area is smaller if the compression ratio is increased. Furthermore, the curves cross at -13.4° crank angle.

On the right hand side of figure 3.19 the apparent flame radius is shown where a spherically propagating flame is assumed over the entire crank angle range. In the strict sense this assumption is only valid as long as the flame does not impinge the walls. Therefore, the flame radius is denoted as apparent flame radius.

Flame front area   **Apparent flame radius**
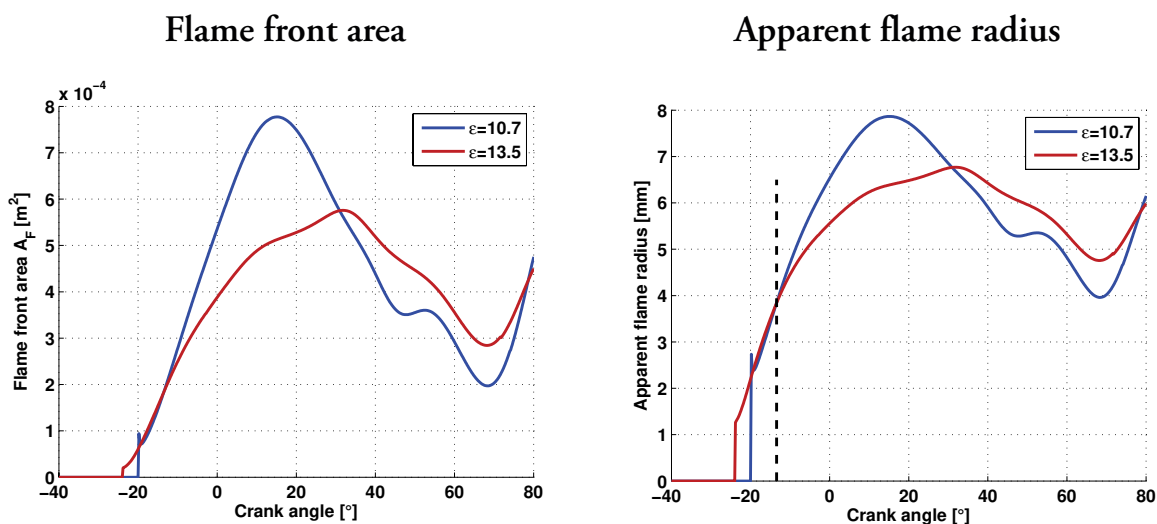
Figure 3.19: Flame front area and apparent flame radius for n=3000rpm, bmep=4bar, spark timing=40°CA BTDC, ε=10.7 and ε=13.5

The dashed line in the right diagram of figure 3.19 indicates the time when the curves cross. In figure 3.20 a sphere with the corresponding radius is drawn into the combustion chamber at this time. It was seen that the flame impinges the piston at CA=-13.4°. This piston position is exactly the moment where the flame front area curve flattens and the burn rate slows down.

ε=10.7   **ε=13.5**
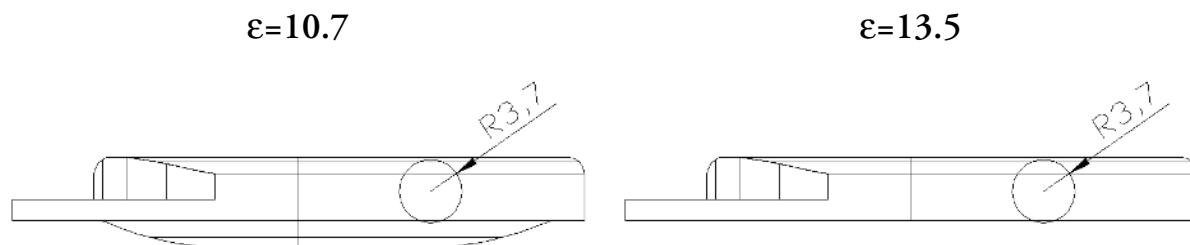
Figure 3.20: „Flame visualisation" in the combustion chamber at -13.4° crank angle

This observation was very helpful to understand the combustion behaviour of the high compression ratio engine and it is encouraging that these effects could be observed by using the phenomenological combustion model.

The flame-piston interaction leads to smaller „reactive" flame front areas. Therefore, the entrainment of the unburned mixture and the burn rate decrease (equation 3.10) leading to decreasing engine efficiency. Furthermore, high burning speeds are necessary to drive the engine with high EGR rates.

3.8 Comparison of Different Combustion Chamber Geometries

The procedure described in chapter 3.3 was used to determine the characteristic mean flame front area for $\varepsilon=13.5$. The spark timing has been varied at the same operating point as for $\varepsilon=10.7$ (n=2000rpm, bmep=2bar) and the flame front areas have been computed based on experimentally determined burn rate curves. The following figure shows the comparison between the two compression ratios.
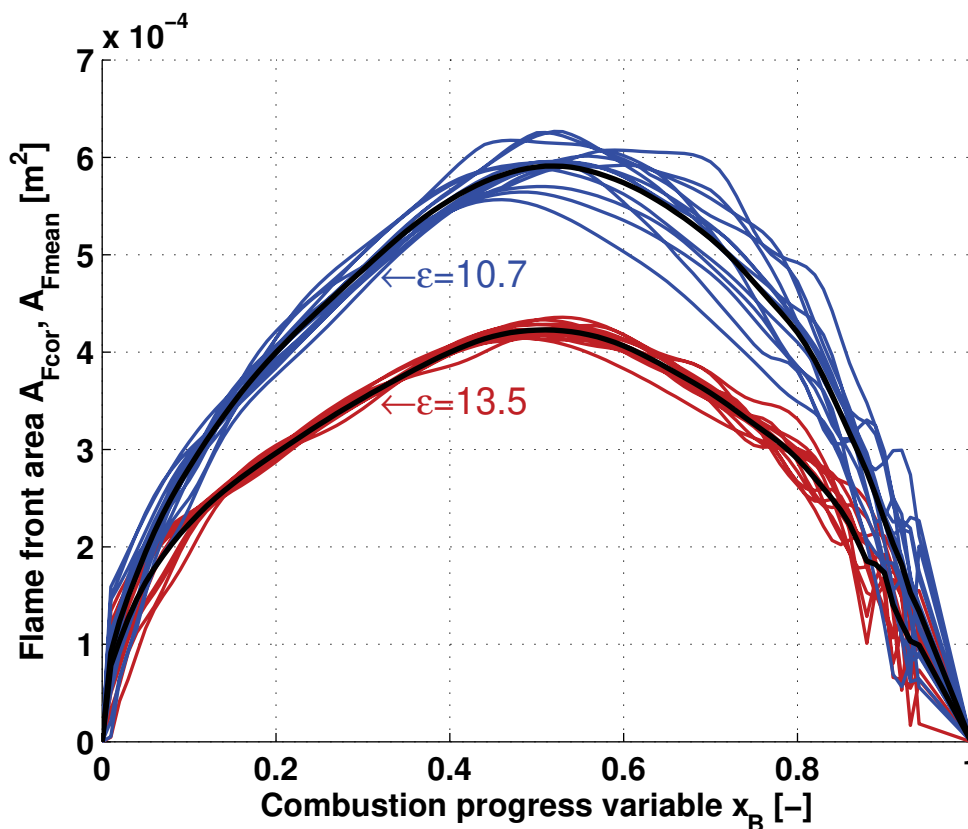
Figure 3.21: Corrected flame front areas and characteristic mean flame front areas as a function of the combustion progress variable x_B, $\varepsilon=10.7$ and $\varepsilon=13.5$

As already observed for the 3000/4 operating point (chapter 3.7) the characteristic mean flame front area is smaller for the higher compression ratio. This means that A_{Fmean} has to be tuned by one measurement for every new combustion chamber design.

Based on the curve for the $\varepsilon=10.7$ case, the characteristic mean flame front area for the $\varepsilon=13.5$ case can be approximated by a very simplified formulation where

basically two approaches can be applied. First, it will be assumed that the flame propagates spherically without wall interactions. The second approximation will be the flame propagation in a disc shaped combustion chamber. The combustion chamber used in this work can be approximated by a disc, where pent-roof combustion chambers may be approximated by a sphere. The following figure compares the shapes of the flame where the grey area indicates the flame front area A_F which is actually the „reactive" area.

Case 1: Spherical flame   Case 2: Disc shaped flame
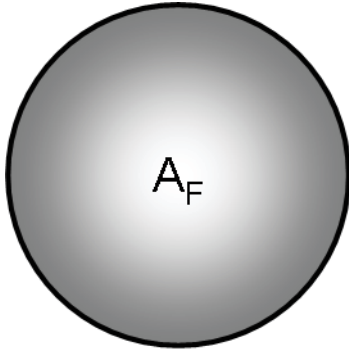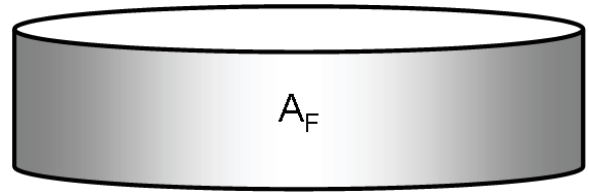
Figure 3.22: Simplified description of the flame propagation

Assuming a spherically propagating flame without wall interactions the flame front area A_{sphere} can be expressed as a function of V_{sphere} by

$$V_{sphere} = \frac{4}{3}\pi r_{sphere}^3 \ and \ A_{sphere} = 4\pi r_{sphere}^2 \Rightarrow A_{sphere} \sim V_{sphere}^{2/3} \qquad 3.26$$

If one assumes that the volume of the burned gases can be described based on the instantaneous cylinder volume the ratio of the two flame front areas can be defined as

$$A_{F13.5} = A_{F10.7} \cdot \left(\frac{V_{cyl13.5}}{V_{cyl10.7}}\right)^{2/3} \qquad 3.27$$

The subscripts in equation 3.27 denote the compression ratios.

For the disc shaped combustion chamber the flame front area can be defined as follows

$$A_{disc} = 2\pi r_{disc} \cdot h_{disc} \qquad\qquad 3.28$$

If one assumes that the radius can be described by the bore, the ratio of the flame front areas can be obtained.

$$A_{F13.5} = A_{F10.7} \cdot \frac{h_{13.5}}{h_{10.7}} \qquad\qquad 3.29$$

Due to the time dependence of the volume ratio and the ratio of the heights, one more simplification was introduced. For both approximations the values at top dead centre have been assumed to be representative. This means that the volume ratio and the ratio of the combustion chamber heights at TDC have been calculated.

Case 1: Spherically propagating flame:

$$\frac{A_{F13.5}}{A_{F10.7}} = \left(\frac{V_{TDC13.5}}{V_{TDC10.7}}\right)^{2/3} = \left(\frac{\varepsilon_{10.7}-1}{\varepsilon_{13.5}-1}\right)^{2/3} = 0.844 \qquad\qquad 3.30$$

Case 2: From the CAD drawings shown in figure 3.20 the heights at TDC could be defined. For the piston bowl and the cylinder head a mean height was calculated by dividing the volumes by the corresponding areas. The following table shows the resulting values

h_{squish}	mm	1.2
$h_{cylhead}$	mm	4.88
h_{bowl}	mm	2.24

Table 3.5: Combustion chamber height

This leads to the following flame front area ratio

$$\frac{A_{F13.5}}{A_{F10.7}} = \frac{h_{squish}+h_{cylhead}}{h_{squish}+h_{cylhead}+h_{bowl}} = 0.731 \qquad\qquad 3.31$$

Based on the characteristic mean flame front area for $\varepsilon=10.7$, $A_{Fmean,\varepsilon=13.5}$ was calculated. The resulting curves are plotted in figure 3.23.

It can be seen that the spherical approach is valid until the combustion progress variable achieves about 5%. It seems that during this phase a freely

propagating spherically shaped flame can be assumed. This is in good agreement with the observations shown in chapter 3.7 for the 3000/4 operating point where the flame impingement was visualised.
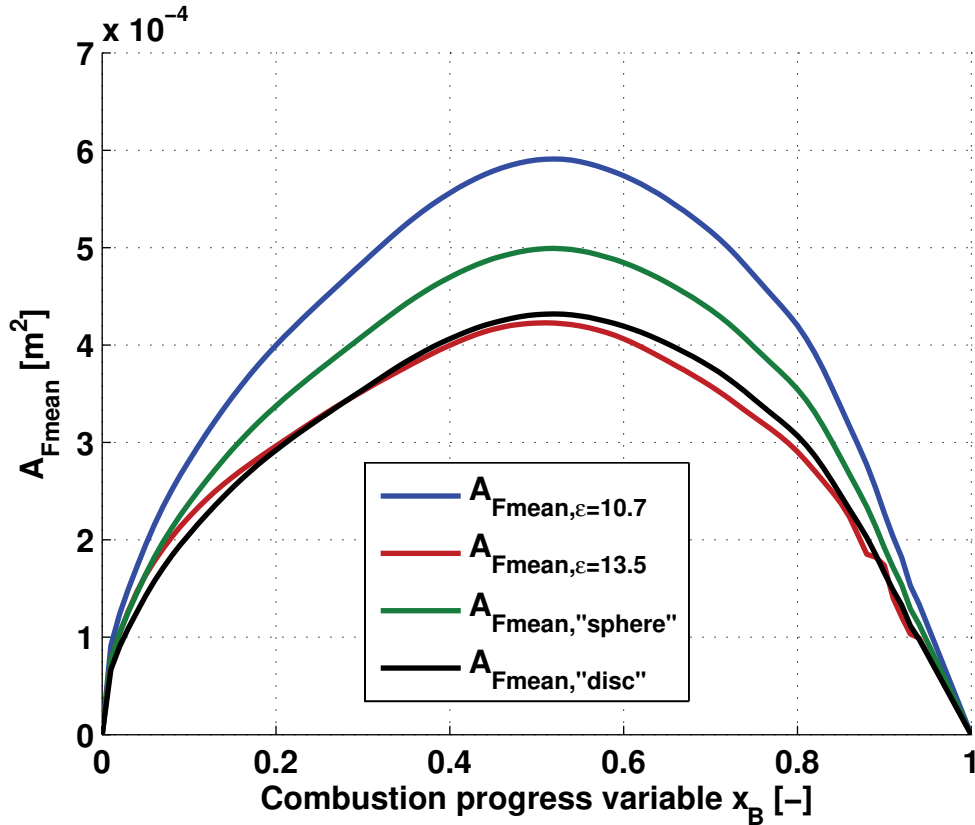
Figure 3.23: Approximation of the mean flame front area for ε=13.5 based on the mean flame front area for ε=10.7

In the range of x_B=0.05 to x_B=0.25 there seems to be a transition phase where the flame shape is like a spherical segment. If x_B=0.25 is reached, the flame front area for the ε=13.5 case can be quite well approximated by the disc shaped assumption which is in good agreement with the combustion chamber design (figure 3.20). The differences between the approximation and the experimentally determined flame front area after x_B=0.25 may occur from the assumption that the radius of the disc can be approximated by the bore and as a consequence that the radius is equal for both geometries.

3.9 Evaluation of the Phenomenological Combustion Model for Different Combustion Chamber Designs

Further tests with the phenomenological combustion model have been performed where the operating points listed in appendix A.2 have been employed for the high compression ratio engine (ε=13.5). The use of different combustion chamber designs gives the opportunity to extensively test the physical formulations.

The modelling parameters listed in table 3.4 have been retained and the characteristic mean flame front area for ε=13.5 shown in figure 3.21 was applied. The volume correction exponent n_{vol} was set to 1 over the entire crank angle range.

Figure 3.24 compares the experimentally determined and calculated crank angle at 5% burned where the lines again are separated by the non-EGR and the EGR cases.

Figure 3.24: Experimentally determined and calculated crank angle at 5% burned for the operating points listed in appendix A.2, ε=13.5

For all investigated operating points except number 1 a too fast burn behaviour up to 5% mass fraction burned can be observed. Many possible reasons can be named. As the agreement was very well for the ε=10.7 case, the submodels of the laminar flame speed, turbulence intensity and turbulent flame speed possibly do not accurately enough consider the new thermodynamic and fluid mechanical conditions. On the other hand the model seems to reproduce the trends qualitatively very well.

The explanation for these deviations was found on the experimental side. The ECU software had to be adjusted for the new engine configuration. The software used for these two engine configurations have been compared and it was found that the injection timing was improved for ε=13.5. It is known that injection timing affects burn behaviour and emissions even in port injection engines [40, 44].
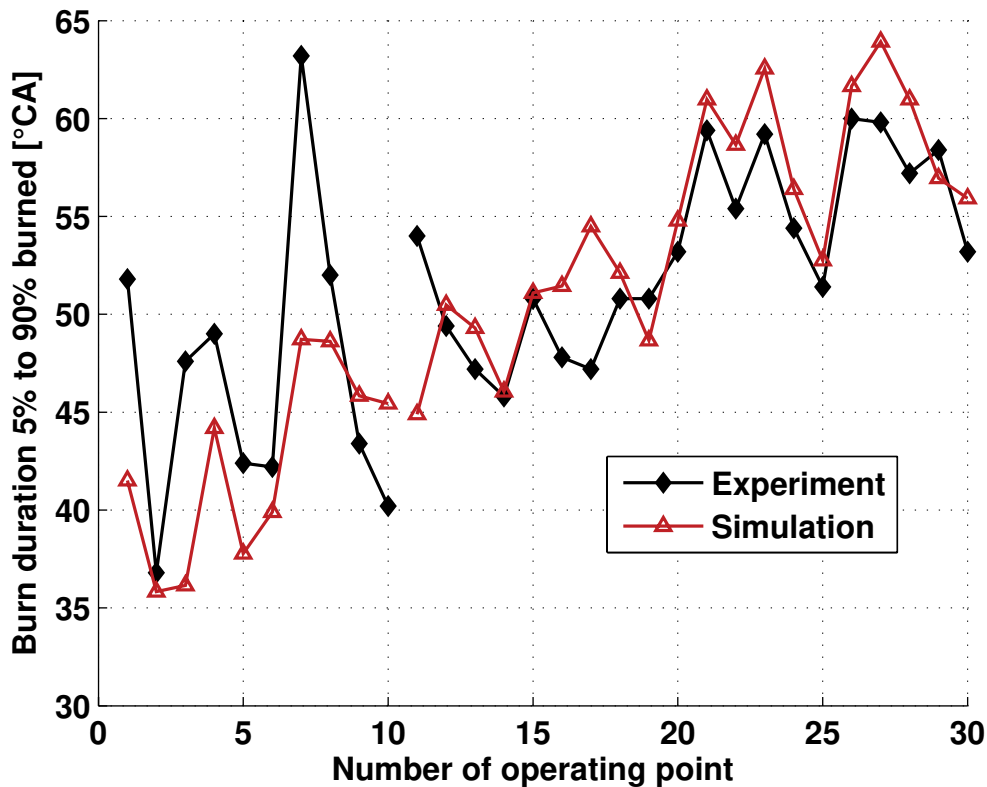
Figure 3.25: Experimentally determined and calculated burn duration for the operating points listed in appendix A.2, ε=13.5

The experimentally determined and computed burn durations shown in figure 3.25 agree quite well in contrast to the empirical model (figure 3.13). Smaller differences can be found for the operating points with EGR. Operating point number

7 again can not be matched. For operating point number 11 the computed inflammation phase is to short leading to a shorter burn duration. As a consequence the crank angle at 50% burned occurs too early in the simulation. This operating point underlines the importance of an accurate formulation of the early combustion period.

Together with figure 3.26, where the crank angles at 50% burned are compared, it can be seen that this model is very helpful in analysing and predicting combustion processes for compressed natural gas engines and various operating conditions. The explicit physical formulation in contrast to the empirically based formulation has advantages if different engine configurations are employed.
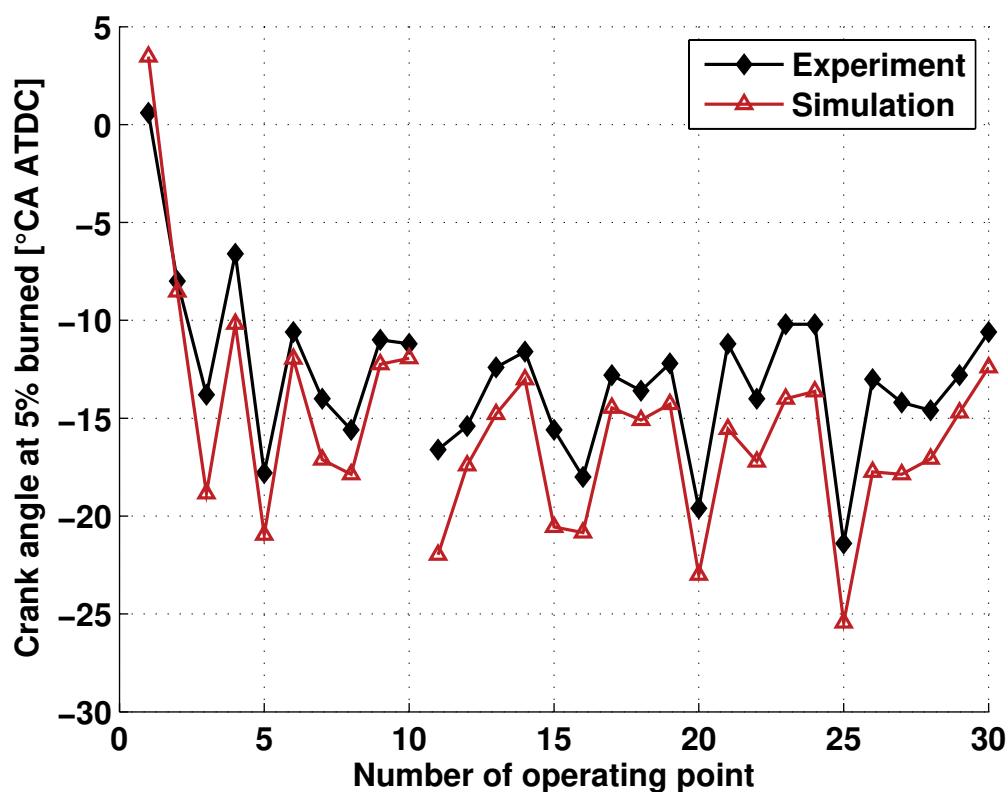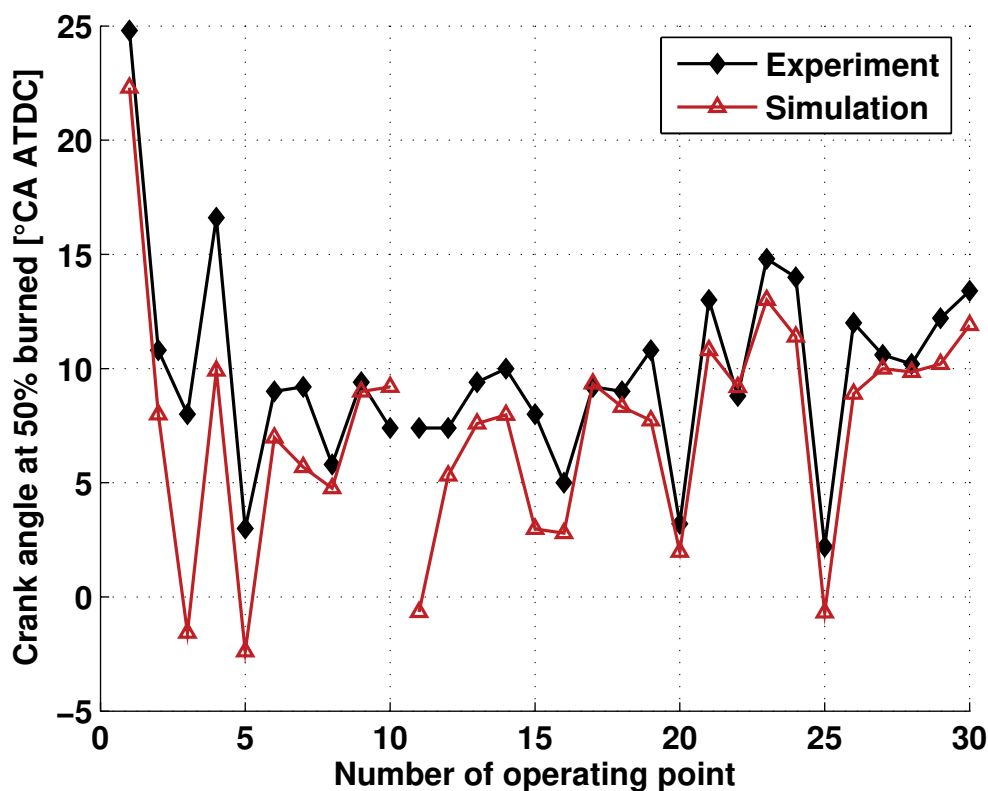

Figure 3.26: Experimentally determined and calculated crank angle at 50% burned for the operating points listed in appendix A.2, ε=13.5

A disadvantage of the phenomenological model is that the characteristic mean flame front area has to be redefined if the combustion chamber geometry changes. On the other hand the calibration of the model is easily possible in this way. It was shown in chapter 3.8 that the characteristic mean flame front area may be

approximated by simple spherically/disc shaped flame propagation assumptions. Nevertheless, the calibration with experimental data is advantageous.

Experimental data are very important to test and validate combustion models independent of the combustion model used. A well-defined engine model and an accurate combustion model lead to enormous advantages during the development process. Simulation tools can be used to accelerate development and are useful to support understanding the experimental results.

3.10 Comparison with Gasoline Engines

The theoretical potential to reduce CO_2 emissions compared to gasoline engines could not be achieved in the CEV-project. For most of the cars on the market, the reduction was found to be between 21% and 23% where the theoretical potential is 25%, if the same efficiency is assumed.

Based on the measurements carried out in the CEV-project the average efficiency in the New European Driving Cycle was calculated. It has to be mentioned here, that the same centrifugal mass has been used for gasoline and CNG operation. The results obtained for the gasoline vehicle and the CNG configurations for ε=10.7 and ε=13.5 are compared in the following table.

		Gasoline	CNG, ε=10.7	CNG, ε=13.5
CO_2	g/km	148.6	116.5	113
Fuel consumption	kg/100km	4.69	4.28	4.13
Energy consumption	MJ/100km	197.2	214	206.7
Mean cycle efficiency	%	15.2	14.3	14.7

Table 3.6:   Mean efficiency in the NEDC for different fuels and concepts

The lower heating value was set to 42.7MJ/kg for gasoline and 50MJ/kg for compressed natural gas. The results for CNG operation shown in table 3.6 have been obtained with methane (G20).

It can be seen that the efficiency for both CNG configurations is lower than for the gasoline vehicle, although the throttle losses can be reduced, if compressed natural gas is injected. These observations lead to the conclusion that the efficiency of the high pressure part is lower for CNG engines.

The phenomenological model formulation indicates that only the formulation of the laminar flame speed has to be adjusted, if gasoline is used instead of compressed natural gas. The other submodels can be applied independent of the fuel composition used. The following contour plot displays the ratio of $SL_{CNG}/SL_{Gasoline}$ whereas Rhodes and Keck's approach was used for gasoline. Furthermore, the 3000/4 operating point for both compression ratios is displayed where the experimentally

determined pressure and temperature of the unburned mixture during combustion have been used.
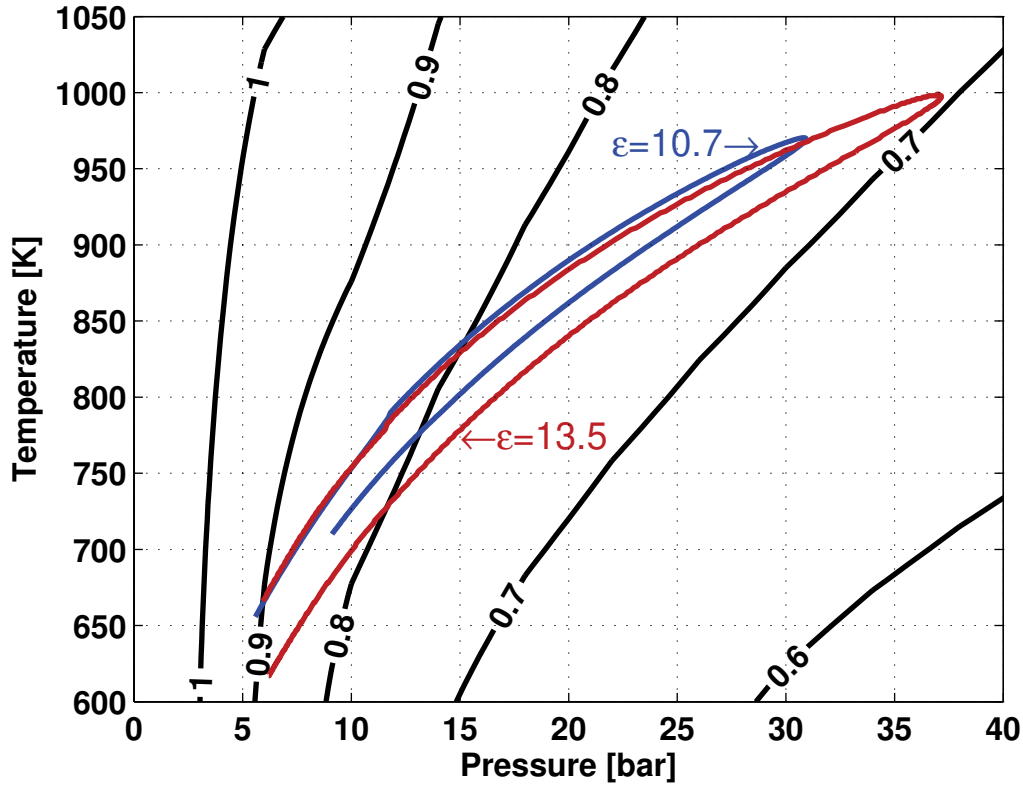
Figure 3.27: Laminar flame speed ratio CNG to gasoline

The compressed natural gas seems to burn faster than gasoline for low pressures. But for the temperature and pressure range relevant during the combustion period in engines, compressed natural gas burns slower. Low burn rates - and therefore high burn durations - lead to lower efficiencies. The formulation for the laminar burn rate of methane shown in chapter 3.3.1 and figure 3.27 indicate that the burning speed decreases faster for CNG than for gasoline if the pressure increases, where the burning speed for CNG increases faster for increasing temperatures. For an increasing compression ratio the pressure and temperature at the end of compression can be approximated by

$$p_2 = p_1 \cdot \varepsilon^{\kappa}$$
$$T_2 = T_1 \cdot \varepsilon^{\kappa - 1}$$

3.32

In this case, the pressure increase is comparatively higher leading to smaller $SL_{CNG}/SL_{Gasoline}$ ratios, as it can be seen in figure 3.27.

The phenomenological model should be able to consider different fuel compositions due to the physically based formulation. Therefore, simulations have been performed with CNG and gasoline, whereas the laminar flame speed of natural gas has been replaced by Rhodes and Keck's approach for the gasoline case. The flame front area is independent of the fuel composition and therefore the characteristic mean flame front area for $\varepsilon=10.7$ has been used for both fuels.

As a result the difference $\Delta\eta_e=\eta_{egasoline}-\eta_{eCNG}$ in percent - where η_e denotes the brake efficiency - is visualised as contour plot in the following figure.
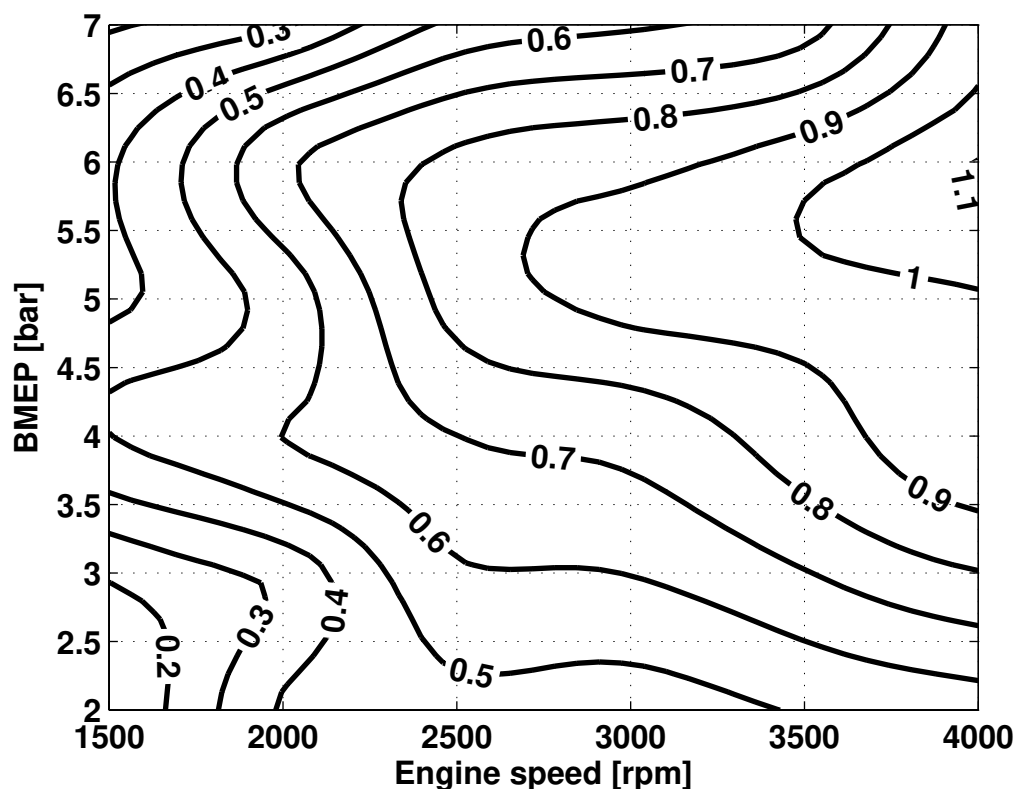
Figure 3.28: $\Delta\eta_e=\eta_{egasoline}-\eta_{eCNG}$ [%] for gasoline and CNG with EGR, $\varepsilon=10.7$

For n=1500rpm and bmep=2bar and for bmep=7bar up to n=3500rpm the engines operate without EGR, where for the other operating points the EGR rate is between 6% and 12%. A general trend can be observed: $\Delta\eta_e$ increases with increasing engine speed and load.

The results shown in figure 3.28 could not be completely explained. One of the influencing parameters is the EGR rate, what can be seen in figure 3.29, where

the same operating points have been computed without EGR. Again, $\Delta\eta_e$ increases with increasing engine speed and load, but the differences here are lower.
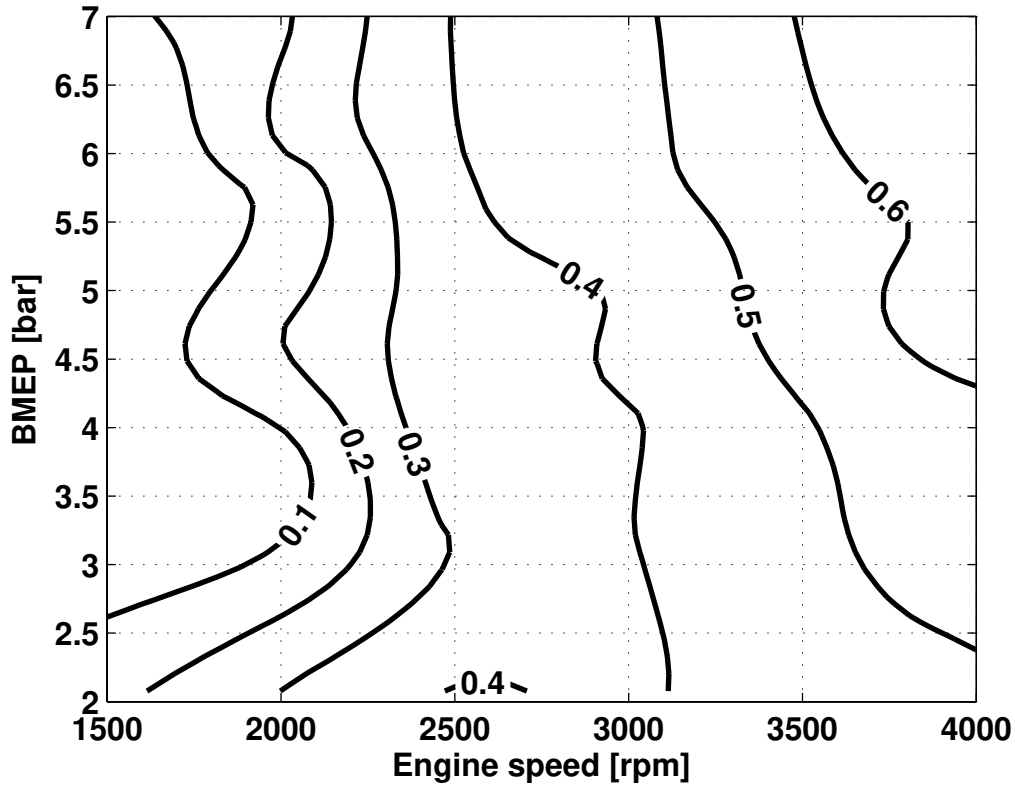
Figure 3.29: $\Delta\eta_e = \eta_{egasoline} - \eta_{eCNG}$ *[%] for gasoline and CNG without EGR,*
$\varepsilon = 10.7$

It has to be taken into account that the water content in the exhaust gases of CNG engines is higher than for gasoline engines resulting in increasing heat capacity of the mixture what may lower the temperature of the unburned mixture comparatively.

Finally, the cycle simulations applied in the CEV-project has been repeated for the maps computed here. The mean cycle efficiency difference $\Delta\eta_e = \eta_{eGasoline} - \eta_{eCNG}$ was found to be 0.5%-point with EGR - what is in good agreement with the experimental results shown in table 3.6 - and 0.3%-point without EGR. It can be concluded, that the impact of EGR on brake efficiency is comparatively higher for CNG engines.

3.11 Combustion Analysis Using 3D-CRFD and Comparison with the Phenomenological Model

Since the combustion chamber has no optical access the flame impingement on the piston observed with the phenomenological combustion model has been validated using 3D-CRFD calculations. The Weller flame area model as implemented in Star-CD [29] was employed. The model parameters have been varied to obtain agreement between experiment and simulation. A short description of the model is given in chapter 3.11.1 followed by a discussion of the results in chapter 3.11.2.

3.11.1 The Weller Flame Area Model

The Weller model is a flame area model where a wrinkling factor Ξ defines the flame surface

$$\Xi = \frac{\Sigma}{\Sigma_l} \qquad\qquad 3.33$$

where Σ and Σ_l are the volumetric average turbulent flame area and laminar flame area, respectively.

In Star-CD the equilibrium version of the Weller flame propagation is implemented. This means that the transport equation for the wrinkling factor is simplified to its equilibrium formulation with a wrinkling generation factor G and a removal rate coefficient R:

$$\Xi = \frac{G}{\Xi_{eq}} \qquad\qquad 3.34$$

Under these circumstances the equilibrium value Ξ_{eq} is equal to the turbulent to laminar flame speed ratio which is described with Damköhler's correlation:

$$\Xi_{eq} = \frac{S_T}{S_L} \ and \ \frac{S_T}{S_L} = 1 + A_D \cdot \frac{u'}{S_L} \qquad\qquad 3.35$$

The parameter A_D is a model coefficient and u' is the turbulence intensity. Keck and Methgalchi's approach for the laminar flame speed, the unstrained laminar flame speed, is used, where the coefficients are adjusted depending on the equivalence ratio of the fuel:

$$S_L = S_{L0} \cdot \left(\frac{T_U}{T_0}\right)^{\alpha_{SL}} \cdot \left(\frac{p_{cyl}}{p_0}\right)^{\beta_{SL}} \qquad 3.36$$

where p is the pressure and T the temperature, the subscripts cyl, 0 and U denote cylinder, unburned and reference gas properties, respectively.

To take into account the laminar flame behaviour during the early stages of flame propagation Ξ is modelled by a time delay function:

$$\Xi = 1 + (\Xi_{eq} - 1) \cdot \left(1 - e^{\frac{-(1 - t_{ST})}{\tau_d \cdot \tau_\eta}} \right) \qquad 3.37$$

t_{ST} is the spark timing, $\tau_\eta = \sqrt{\nu/\varepsilon}$ is the Kolmogorov time scale and τ_d is a time delay coefficient.

The mean reaction rate for the regress variable b is given by

$$\omega_{We} = -\rho_U \cdot Y_U \cdot S_L \cdot \Xi \cdot |\nabla b| \qquad 3.38$$

Y_U is the mass fraction of the unburned mixture and b is the regress variable, the normalised fuel mass fraction, and is defined as

$$b = \frac{Y_f - Y_{res}}{Y_{ft} - Y_{res}} \qquad 3.39$$

which has the value 1 in the unburned gas and 0 in the burned gas. Here Y_f is the fuel mass fraction, Y_{ft} is the total fuel mass fraction, i.e. the fuel mass fraction in the unburned gas, and Y_{res} is the amount of fuel left when the deficient reactant is consumed, i.e. the amount of fuel left at the end of combustion.

3.11.2 Results

The model parameters A and τ_d have been varied to obtain agreement between experiment and simulation for both combustion chamber designs and had to be optimised for every operating point. Figure 3.30 shows the comparison of the cumulative burn rate, the burn rate and the cylinder pressure for both compression ratios.

It can be observed that the start of combustion can be reproduced well, whereas in the late part of the combustion the burn rate is higher for the computations. One of the reasons for these differences may be the use of Keck and Methgalchi's approach for the laminar flame speed in Star-CD. It is unknown, if the parameters α_{SL} and β_{SL} are adjusted for compressed natural gas.

The computed cylinder pressures were higher than the experimentally determined pressure data for all operating points investigated. It was found that the wall heat losses have been underestimated by the 3D-CRFD code. In this work, no further investigations of the wall heat losses have been carried out.

The regress variable b (equation 3.39) was visualised at CA=-13.4° to compare the results obtained with the phenomenological combustion model. Half of the combustion chamber is displayed in figure 3.31. As it was already observed in the phenomenological case, the flame impinges the piston for ε=13.5 at this time. The dark blue colour and the red colour indicate burned mixture and unburned mixture, respectively. These pictures are in good agreement with the observed burning behaviour shown in figure 3.20.

Comparing the 3D calculation results with the observations made with the phenomenological combustion model it can be noticed that the results seem to be meaningful and do aid one another (see figure 3.31).
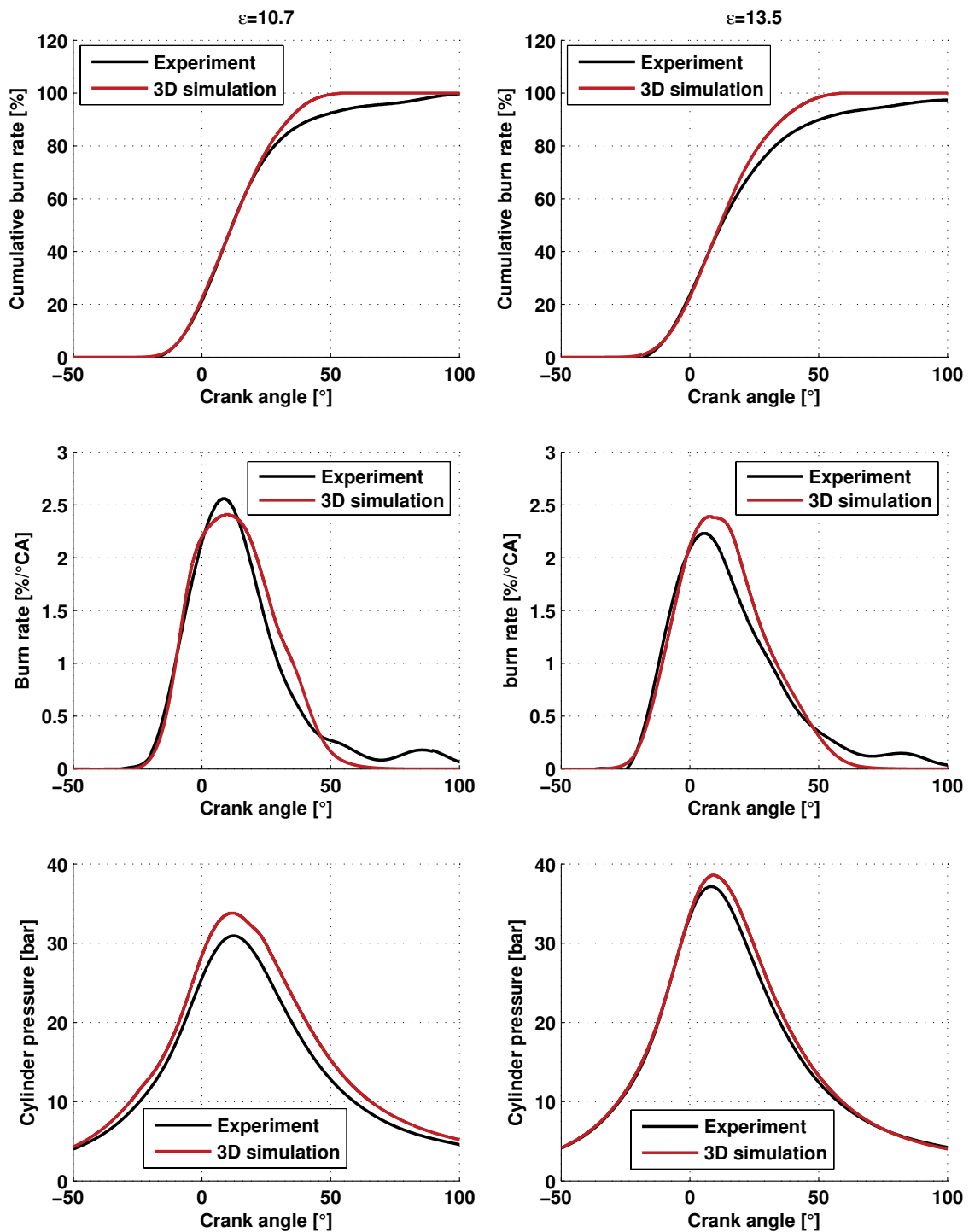
Figure 3.30: *Comparison between experimentally determined and computed data with 3D-CRFD for the same operating condition but different compression ratios, n=3000rpm, bmep=4bar, spark timing=40.5° CA BTDC*

ε=10.7   ε=13.5
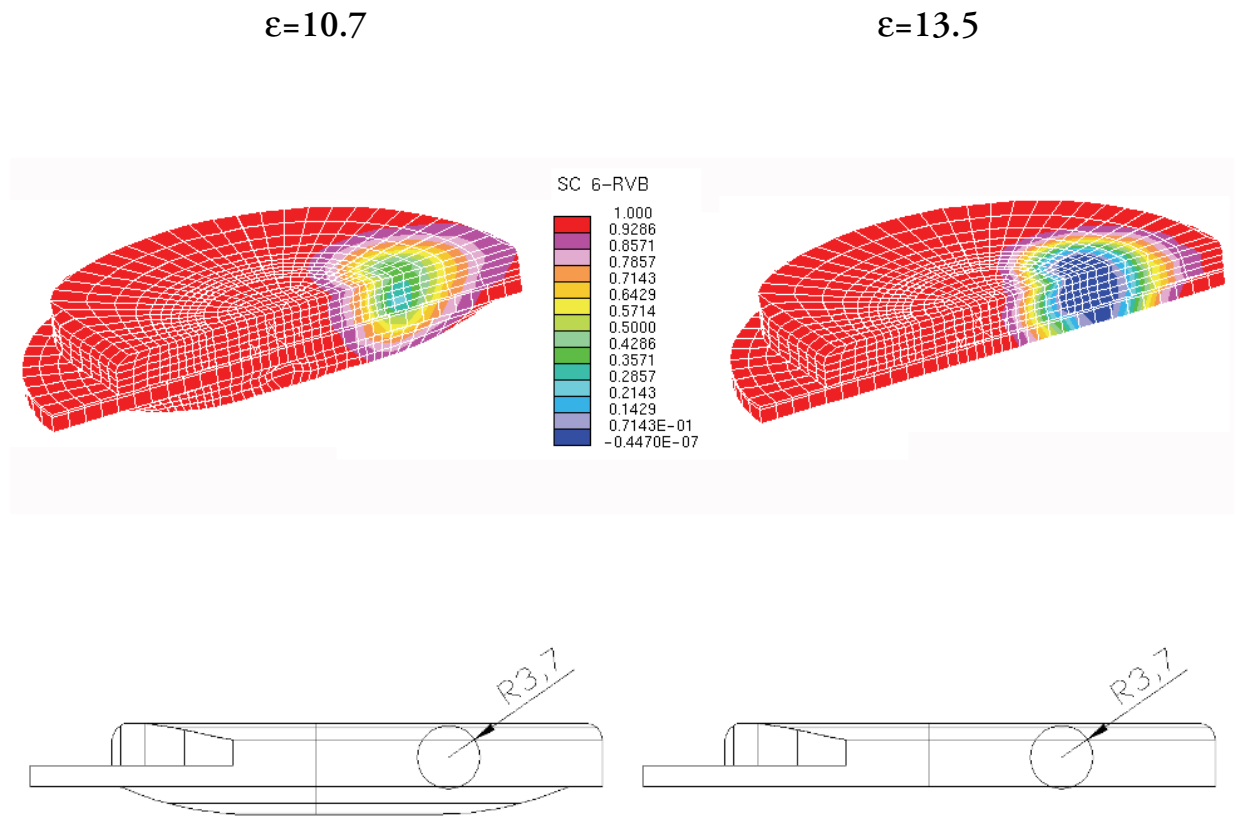
Figure 3.31: Visualisation of the flame propagation using 3D-CRFD and comparison with the phenomenological combustion model

Chapter 4

Study of Knock Behaviour and Knock Model Approach

The knock phenomena in spark ignition engines results from the self-ignition of part of the unburned gas ahead of the propagating flame front. The engine can be damaged due to high cylinder pressure rise and pressure waves if knock occurs. The compression ratio of the production engine (gasoline) has been increased in the CEV-engine to increase efficiency in part load operation and additionally a turbocharger was installed to take advantage of the high knock resistance of natural gas. These arrangements lead to higher risk of knock occurrence in full load condition due to the higher temperatures and pressures although CNG is better than gasoline in this context.

In turbocharged gasoline engines the compression ratio has to be reduced compared to naturally aspirated engines leading to increased fuel consumption in part load operation. The compression ratio and the boost pressure are limited by knock occurrence and thus knock does indirectly affect the overall efficiency.

Nowadays, the engines are equipped with knock sensors to detect the vibrations caused by knocking combustion. The signal is processed in the ECU and as a result the spark timing is retarded - which again lowers efficiency - depending on the knock intensity. This knock detection chain has to be adapted to an engine.

Various research activities for gasoline and some for compressed natural gas engines can be found in the literature where the physics basically remains the same. One of the major challenges for CNG engines is the varying gas composition depending on the regional provenance.

The objective of this chapter is to develop a simple but robust knock model based on the knock integral method for varying operating conditions and different gas compositions where a key factor for the quality of the model was found to be the differentiation between knocking and non-knocking combustion. This model may be used in cycle simulation tools to find the best setup for different engine configurations and parameter settings.

4.1 State of the Art

Most of the investigations concerning knock is done with gasoline, where the approaches and measurement techniques can be applied to compressed natural gas engines. The physics remains qualitatively independent of the fuel. Therefore, observations made for gasoline engines can be partially transferred to compressed natural gas engines.

Only a few knock models dedicated to compressed natural gas can be found. The focus in knock research activities for CNG engines is on experimental knock detection methods and potential estimations on engine test benches.

4.1.1 General Findings

During the last years research activities have led to a better understanding of knock phenomena. Nowadays, it is known that knock occurs due to self-ignition of the unburned gas ahead of the propagating flame front. The start of knock can occur near the wall [50, 65, 108] or just ahead of the flame front [26, 97, 108] and it was observed, that several reaction zones can exist which converge together to look like a propagating premixed flame front [50, 67, 108]. This apparent flame front propagates with a much higher speed than the turbulent flame propagation due to normal combustion [67, 108, 112]. If extreme knock occurred, Kollmeier [67] observed several centres with extremely high locally propagating flame speeds. As knocking strength was reduced, the flames propagated slower. Knock investigations with methanol showed that from the place of knock occurrence a flame with moderate speed started (370m/s) compared to gasoline with 1000m/s or heavy knock with 2200m/s. Later, the flame speed increases up to 1800m/s. Takati et al. [112] observed a seven to eight times higher combustion speed due to autoignition and a speed-up factor of 25 is mentioned by Alt et al. [6]. The place of knock occurrence depends on local temperature gradients [49, 128] and inhomogeneities of fuel and

residual gas distribution. The pressure waves induced due to this self-ignition can cause severe damages to the combustion chamber walls.

The effect of the amount of unburned gas mass fraction at knock onset was investigated by By et al. [27], Chun and Heywood [32] and Stiebels [108]. They report that the mean knock intensity increases, if the unburned gas mass fraction at knock occurrence increases. But Chun and Heywood [32] report that the individual knock intensities do not correlate with unburned gas mass fractions at knock onset. Furthermore, they show that the correlation between the crank angle of knock occurrence and the pressure at the crank angle at 50% burned is better than the correlation between the knock occurrence crank angle and the pressure at knock onset. They derive out of this observation that this indicates that the thermodynamic state history prior to knock is more important than the state at knock onset. Dimitrov [37] and Kollmeier [67] found that cycles which burn faster tend to knock more intensely and earlier than cycles which burn slower. Stiebels [108] observed that high early peak pressures correspond to early knock occurrence and that early knock onset results in heavier knock. This observation was confirmed by Grandin et al. [47]. The influence of the amount of burned gas by autoignition was investigated by Takagi et al. [112]. They found that the closer autoignition occurred relative to top dead centre the huger the amount of mixture burned by autoignition and the higher the knock intensity was. Worret [124] in contrast shows that knocking cycles with an early knock onset or a high end gas temperature do not result in high knock intensities.

The effect of EGR was investigated by Brecq et al. and Sakonji [23, 93] for natural gas engines, for isooctane-n-heptane blends by Diana [36] and for gasoline engines by several researchers [27, 47, 48, 97]. Brecq et al. [23] added N_2 and CO_2 separately to a CNG-air mixture. As expected, a twice higher augmentation of knock limited spark timing is noted if CO_2 is added compared to N_2 for an equivalent volumetric concentration. In all cases an increased knock resistance due to EGR addition was observed. Sakonji et al. [93] compared a 10% EGR dilution with λ=1.1 lean burn operation. Introducing EGR substantially improved the possible brake mean effective pressure and efficiency and at the same time knock intensity was reduced. A turbocharged gas engine for cogeneration [82, 83] was operated with high EGR rates and λ=1 where high efficiencies combined with low NOx-emissions have been achieved.

4.1.2 Knock Detection Methods

In principal, three knock detection methods can be found in the literature where a lot of refinements have been developed and are often compared to each other [5, 36, 41, 61, 106]. Most of the researchers detect knock directly based on the pressure signal where some investigate the net heat release rate [11, 26, 124]. In some cases optical sensors and/or ion sensors are used to observe the local behaviour of the flame and autoignition regions [46, 106]. The pressure and the net heat release rate based methods are used for the adaptation of knock detection systems on engine test benches and for the development of knock models. The optical and ion sensor techniques are used to support the understanding and to learn more about knock phenomena in general [5, 106, 108, 112, 124].

The knock detection method and the differentiation between knocking and non-knocking operating conditions are key parameters in knock research activities and are the basis for a successful development of a knock model, because it has to indicate the start of knock. This differentiation is quite often not described in detail or even not at all mentioned.

If the direct pressure signal analysis is applied the maximum amplitude of the pressure oscillation is most often used. In this case, the pressure trace is filtered with a high or a band-pass filter. The maximum difference between the filtered and the raw data is defined as the maximum amplitude of the pressure oscillation Δp_{max} as shown in figure 4.1.

This procedure is applied to all of the recorded cycles and with statistical methods [32, 41, 67] it is assessed whether the operating point does knock or not. In this case quantiles can be used [41]. A threshold has to be defined to distinguish between knocking and non-knocking combustion. Franzke [43] proposes that the knock limit has to be defined arbitrary and in his case it was chosen if continuous occurrence of pressure oscillations could be observed. Sometimes, the basic noise of the engine and the experimental equipment are first examined before this threshold value is applied [11, 26, 124].

One of the disadvantages of this method is the strong dependence on pressure sensor location [25], fuel composition [25], combustion chamber design [25] and that a threshold value has to be defined for each of the investigated operating points [22, 25, 41]. Breq et al. [22] concluded that the knock level is not unique, because it depends on the engine and on the filter used. Moreover, they say that the knock threshold value should not only be adapted to a specific engine but also to operating

conditions and its selection should be based on solid statistical analysis. Furthermore, the threshold value is dependent on the number of cycles analysed. Some of the works investigate the effect of the applied filter technique [74], the number of consecutive cycles analysed [25, 41] and the pressure sensor location [25, 32, 43, 67]. These parameters strongly influence the results of the pressure oscillation analysis.
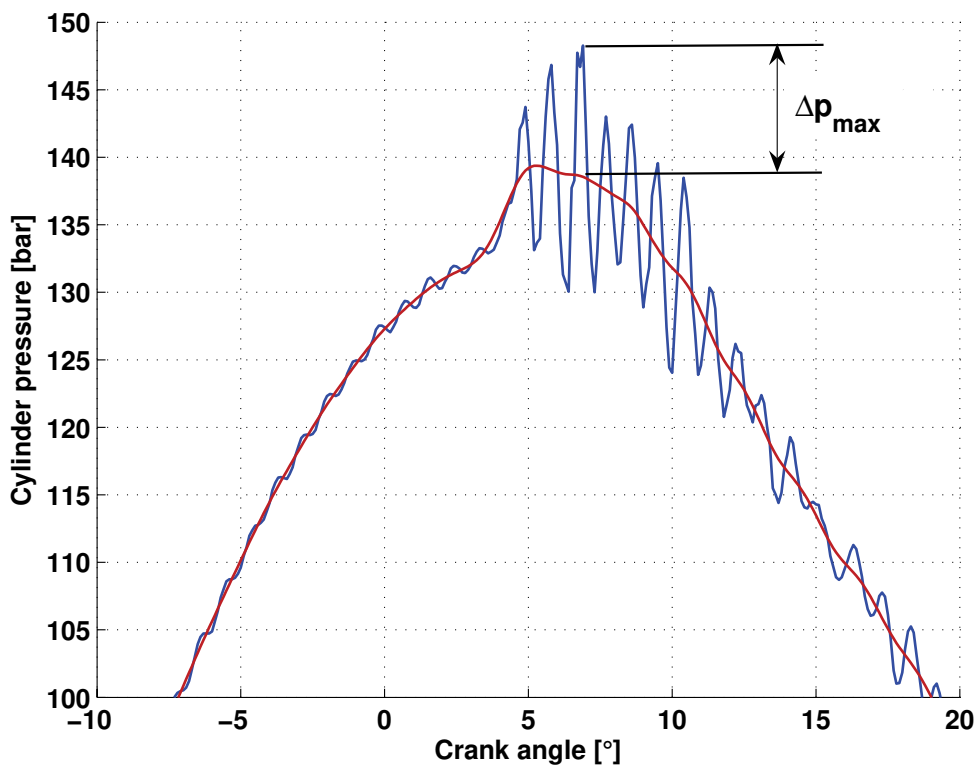
Figure 4.1: Maximum amplitude of pressure oscillations

Another pressure-based method has been developed by Checkel and Dale [30] and was tested in [31, 118, 119]. They used the third derivative of the pressure signal to detect knocking combustion. It is reported that the major difference between their knock indicator and other techniques is that it works with low frequency data (1° CA resolution) rather than requiring adequate time resolution to resolve oscillations at the characteristic knock frequency of the cylinder. A threshold value has to be found to differ between knocking and non-knocking combustion.

Sometimes the „energy" of the pressure oscillations is analysed [22, 56, 67]. This concept is analogous to the definition of the energy of an electrical signal where the square of the difference between the filtered and unfiltered signal is integrated

over a certain crank angle interval. It can be shown, that this indicator correlates well with the maximum pressure amplitude.

If the pressure-based knock detection method is used, the crank angle of knock occurrence - which is the start of knock - is defined as the first remarkable difference between the filtered and the non-filtered signal. In chapter 4.3 it will be shown that the reliable detection of the crank angle of knock occurrence can be very difficult for low engine speeds; an observation which is confirmed by Fischer et al. [41].

Another knock detection method used is the analysis of the net heat release rate. The net heat release rate can be derived as the difference between the burn rate and the wall heat losses and is defined as [54]:

$$\frac{dQ_n}{dt} = \frac{dQ_B}{dt} - \frac{dQ_W}{dt} = \frac{\kappa}{\kappa - 1} p \cdot \frac{dV}{dt} + \frac{1}{\kappa - 1} V \cdot \frac{dp}{dt} \qquad 4.1$$

Bargende [11], Burkhardt [26] and Worret [124] use an approach similar to the pressure oscillation method. They use the difference between the net heat release rate and its high-pass filtered signal. A threshold value was defined to distinguish between knocking and non-knocking combustion. They first investigated the basic noise of the engine and the measurement equipment. The start of knock is again defined by the first remarkable difference of the raw data and the filtered data. Worret defined knock intensity based on the „energy" of the net heat release rate.

Bradley et al. [20, 21] divided the net heat release rate into three parts: flame propagation, autoignition and heat losses where the autoignition is approximated by an Arrhenius approach. They identified the start of autoignition by the first derivative of the net heat release rate. It is noticeable that the net heat release rates plotted in the papers of Bradley et al. [20, 21] look very different from the ones shown by Bargende [11] and Worret [124] - although the authors used the same procedure - and from typical burn rate curves. The knock intensity was still calculated from the maximum pressure amplitudes.

Chun and Heywood [32] mention that they used the burn rate to identify the crank angle of knock occurrence. A check of whether the burn rate was greater than 1.5 times compared to the value of the previous sampling point provided a simple and accurate test of knock occurrence. Unfortunately, they do not show a graphical representation and do not describe any sensitivity analysis for the crank angle of knock occurrence criterion. The knock intensity was defined by the maximum pressure oscillations.

Ando [7] investigated different indicators and used the maximum negative change of the net heat release rate Max($-d^2Q_n/d\phi^2$) to define the knock intensity.

4.1.3 Knock Models for Gasoline Engines

Two types of knock models can be found in the literature. On one hand detailed chemical kinetic models and reduced schemes have been employed to integrate relevant species concentrations and temperature in the end gas over time. On the other hand the so called knock integral method is usually used for cycle simulations and in most cases related to a one step chemistry approach.

The Shell model was developed at Shell research Ltd and has been tested for diesel and gasoline engines [53, 94, 95, 97]. In this model the autoignition chemistry is reduced to an eight-step chain branching reaction scheme.

Initiation

$$RH + O_2 \rightarrow 2R^* \qquad Rate\ coefficient \quad k_q$$

Propagation

$$R^* \rightarrow R^* + P \qquad Rate\ coefficient \quad k_p$$

$$R^* \rightarrow R^* + B \qquad Rate\ coefficient \ f_1 k_p$$

$$R^* \rightarrow R^* + Q \qquad Rate\ coefficient \ f_4 k_p$$

$$R^* + Q \rightarrow R^* + B \qquad Rate\ coefficient \ f_2 k_p$$

4.2

Branching

$$B \rightarrow 2R^* \qquad Rate\ coefficient \quad k_b$$

Termination

$$R^* \rightarrow out \qquad Rate\ coefficient \ f_3 k_p$$

$$2R^* \rightarrow out \qquad Rate\ coefficient \quad k_t$$
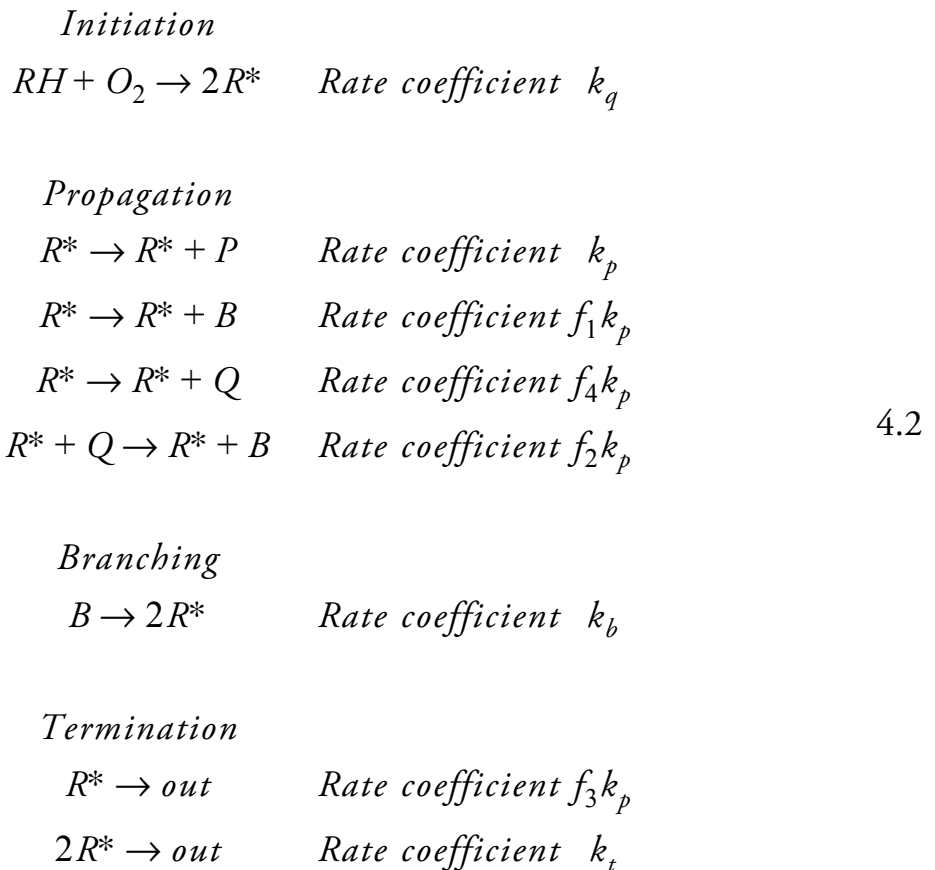
Four stages are processed: The initiation phase is followed by the propagation phase where a branching agent B and an intermediate agent Q are considered. The

third stage is the branching and the fourth is the termination phase. The shell model tries to account for the negative temperature coefficient behaviour observed for most fuels used in engine applications. Chemical heat is release when products P are formed during the propagation phase. A good agreement with experimental data has been observed with the Shell model where the coefficients of the model have to be adjusted to a specific fuel.

Li et al. developed a model [72] to predict the heat release rate and extended it to knock applications [71]. The model was modified and tested for three fuels where the experimentally observed negative temperature coefficient behaviour could be reproduced. The final formulation - which is the extended model described in [72] - consists of 29 reactions and 20 active species.

Cowart et al. [33] used 19 reactions to account for the two-stage hydrocarbon ignition characteristics. This reduced model was compared with a detailed chemical kinetic model consisting of 380 species and 1972 reactions. The knock occurrence criterion was set to a threshold temperature of 1200K where no coupling of the results obtained with the chemical kinetic model to the applied cycle simulation existed.

Another reduced mechanism was developed by Schreiber et al. [98], the so called five-step mechanism. They use five species and six reactions where the scheme is adaptable to fuels of octane numbers of 0 (n-heptane) and 100 (isooctane). The transition from high-temperature reactions to the negative temperature coefficient branch agreed well with experimental data. One of the objectives was to use this five step mechanism for high temperature flame regimes.

A reduced kinetic model was used by Jenkin et al. [61] which is based on the model developed by Li et al.. They divide the near wall region into several slices, where each slice has its own unique temperature.

Three models have been compared by Kleinschmidt [65]. He tested the model developed by Li et al., the five-step model and the Shell model. He found that for low engine speeds the Shell and Li model predicted the crank angle of knock occurrence well where at high engine speeds disagreement between prediction and measurement was observed. He introduces a third zone which is part of the unburned zone but with its own temperature and having a defined but small mass compared to the unburned zone. It was assumed that the processes within this zone cause no reaction in the unburned and burned zone.

The most often used knock integral method model is the one developed by Douaud and Eyzat [38]. The basic idea is that all reactions in the unburned gas are described by one global reaction of species i. The history of this reaction and the possible build up of radicals is considered by a time integration of the reaction rate of this global species. Knock occurs if the knock integral achieves a critical value KI=1. The reaction rate is approximated by a characteristic reaction time and is expressed as an Arrhenius function. The following scheme describes the procedure.

$$\frac{\partial c_i}{\partial t} \sim \frac{1}{\tau_{reac}} \; and \; \tau_{reac} = Ap^{-\alpha}e^{TA/T_U} \qquad\qquad 4.3$$

$$KI_{CAknock} = \frac{1}{c_{iknock}} \int_{t_{IVC}}^{t_{knock}} \frac{1}{\tau_{reac}}dt = 1 \qquad\qquad 4.4$$

They developed a knock model for gasoline engines and tested it on about one thousand measurements referring to different octane requirements made at wide open throttle and various constant speeds on about 60 European and Japanese passenger cars. By et al. [27] compared four knock models for gasoline engines. The best results were obtained using the correlation of Douaud and Eyzat. Wayne et al. [119] used the same approach but redefined the parameters (A, α, TA) for their application.

Worret [124] found that the predictions obtained with the knock integral method were not precise enough. He introduces a correction function for the knock integral, where a correlation between the knock integral and the crank angle of 75% mass fraction burned was found. He then applied the K-value (see chapter 4.1.5) of Franzke [43] to his engine. In his case, the K-value was not constant at knock limit. He then made a „K-value-correction" as a function of the excess air ratio λ and the crank angle at 50% burned. He argues that every cycle reaches the critical value with the knock integral sometime although not every cycle knocks. He then compares the crank angle at knock onset with the crank angle calculated from the K-value and decides whether the operating point does knock or not.

4.1.4 Knock Models for CNG Engines

Karim et al. [64] introduced a methane-air system consisting of 32 elementary reaction steps and 14 reactive species. They show that trends can be predicted quite well with their knock model.

A one step chemistry approach, the knock integral method, was developed by Soylu et al. [103]. They use compressed natural gas consisting of 94% methane, 3% ethane, 3% propane, N_2 and other gases for their investigations and added propane to this natural gas. The model found was also implemented into the KIVA-code. The knock integral showed good predictions of the crank angle of knock occurrence whereas the results obtained with the KIVA code where less satisfactory.

Dimitrov et al. [37] - who used a stationary gas engine - extended the knock integral to take into account combustion chamber geometry and methane number. He showed that shorter ignition delays - spark timing to 1% mass fraction burned - leaded to heavier knock and a correlation between ignition delay and peak pressure can be found. Two additional conditions have been introduced to account for non-knocking cycles. The unburned gas mass fraction and the knock intensity have to exceed certain values. The knock intensity was modelled to be proportional to the speed of a detonation wave. The whole procedure can be summarised as follows: The mean burn rate is calculated using cycle simulations and a mean knock integral is defined. The ignition delay is then shortened from which a new burn rate and maximum cylinder pressure result. A new crank angle of knock occurrence is defined by the knock integral. The criterions defined above are used to decide whether the cycle does knock or not.

Boulouchos et al. [17] used the knock integral method to investigate the potential of EGR utilisation for full load operation.

4.1.5 Knock Models for Other Fuels

Franzke [43] used a propane-air mixture for his knock integral model and introduced a „K-value". He divided the crank angle interval from start of combustion to the crank angle of knock occurrence $CA_{knock} - \varphi_{x_B = 0.01}$ by the overall burn duration which was defined as $\varphi_{x_B = 0.95} - \varphi_{x_B = 0.01}$ and found that this „K-value" is constant at the knock limit.

$$K = \frac{CA_{knock} - \varphi_{x_B = 0.01}}{\varphi_{x_B = 0.95} - \varphi_{x_B = 0.01}} \approx 0.53 \qquad 4.5$$

The crank angle of knock onset can then be defined based on the overall burn duration by using equation 4.5.

4.2 Investigated Operating Points and Gas Compositions Used

Due to the fact that a knock model based on the knock integral method will be developed (see equation 4.4) allowing to predict knock for various operating conditions of an engine at full load, variations of pressure, temperature and time for the measurements to be taken are necessary. Therefore, intake pressure, intake temperature and engine speed have been varied. Figure 4.2 displays schematically the variations examined.
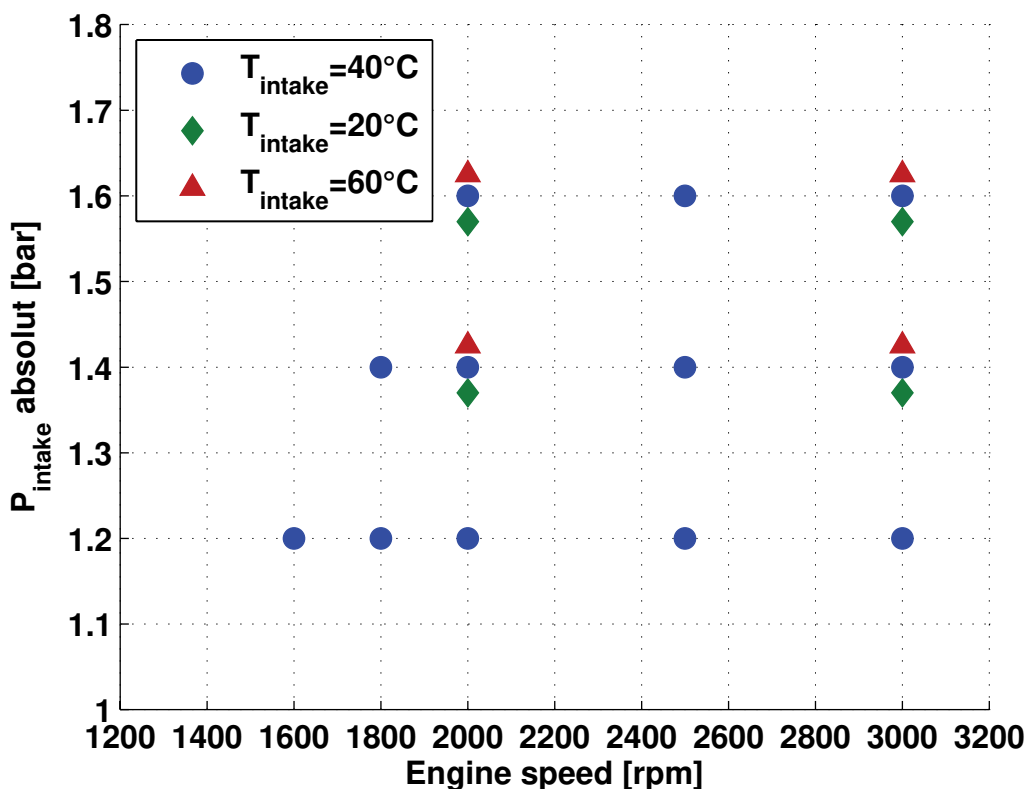
Figure 4.2:   Investigated operating points to examine knock

The major objective was to keep the intake pressure constant - at several pressure levels - over the entire range of investigated engine speeds. Therefore, only one intake temperature was tested at low intake pressure where $T_{intake}=40°C$ was taken as reference. For $p_{intake}=1.4$bar and $p_{intake}=1.6$bar at n=2000rpm and n=3000rpm the intake temperature was decreased by 20°C and increased by 20°C, respectively. As it is shown in figure 4.2 not all of the engine speeds could be tested at higher intake pressures.

The spark timing was varied by an increment of 0.75° CA - which was limited by the resolution of the ECU - and was used to adjust knock intensity in the sense of driving from non-knocking to knocking combustion continuously.

This test series was performed with five well-defined compositions of synthetic gases which are summarised in the following table. Thought has been given to the major components found in natural gases, where natural gas compositions of various countries have been studied. Based on the reference gas consisting of 100% methane the ethane content was increased by 4% (G4E) to 8% (G8E). For G44 4% propane was added to a 92% methane/4% ethane mixture and finally an official test gas for the NEDC containing dilute gases was used (G25).

Names have been created for the gases containing ethane, where the numbers indicate the ethane and propane content, respectively. G20 and G25 in addition are official terms.

		G20	G4E	G8E	G44	G25
Component	**Unit**					
Methane CH_4	**Vol.-% / Mass-%**	100 / 100	96 / 92.76	92 / 85.99	92 / 83.26	86 / 77.86
Ethane C_2H_6	**Vol.-% / Mass-%**	--	4 / 7.24	8 / 14.01	4 / 6.79	--
Propane C_3H_8	**Vol.-% / Mass-%**	--	--	--	4 / 9.95	--
Nitrogen N_2	**Vol.-% / Mass-%**	--	--	--	--	14 / 22.14
Density*	**kg/m³**	0.7155	0.7405	0.7655	0.7906	0.7903
Lower heating value	**MJ/kg**	50.012	49.415	48.856	49.088	38.94
Stochiometric Air-Fuel ratio**	**kg/kg**	17.372	17.289	17.211	17.138	13.526

* at p=1.013bar and T=273.15K
** for 10.7% O_2 content in the air (by volume)

Table 4.1:   Gas compositions used for the knock model development process

4.3 Knock Detection Method

The widely-used maximum amplitude of the pressure oscillations - shown in figure 4.1 - has been tested to detect knocking combustion. Due to the high frequency pressure waves the resolution of the pressure recording was set to 0.1° CA. 581 cycles have been stored to ensure an accurate statistical analysis.

Figure 4.3 displays Δp_{max} for four operating points and three selected spark timings for each of the operating points as a function of the cycle number.

In the first row the engine speed was varied but the intake pressure kept constant. In the second row the engine speed remains constant, where the intake pressure was increased. T_{intake} was 40°C for all the operating points displayed.

For these calculations a threshold value of Δp_{max}=0.2bar was set to account for the variations due to the experimental setup.
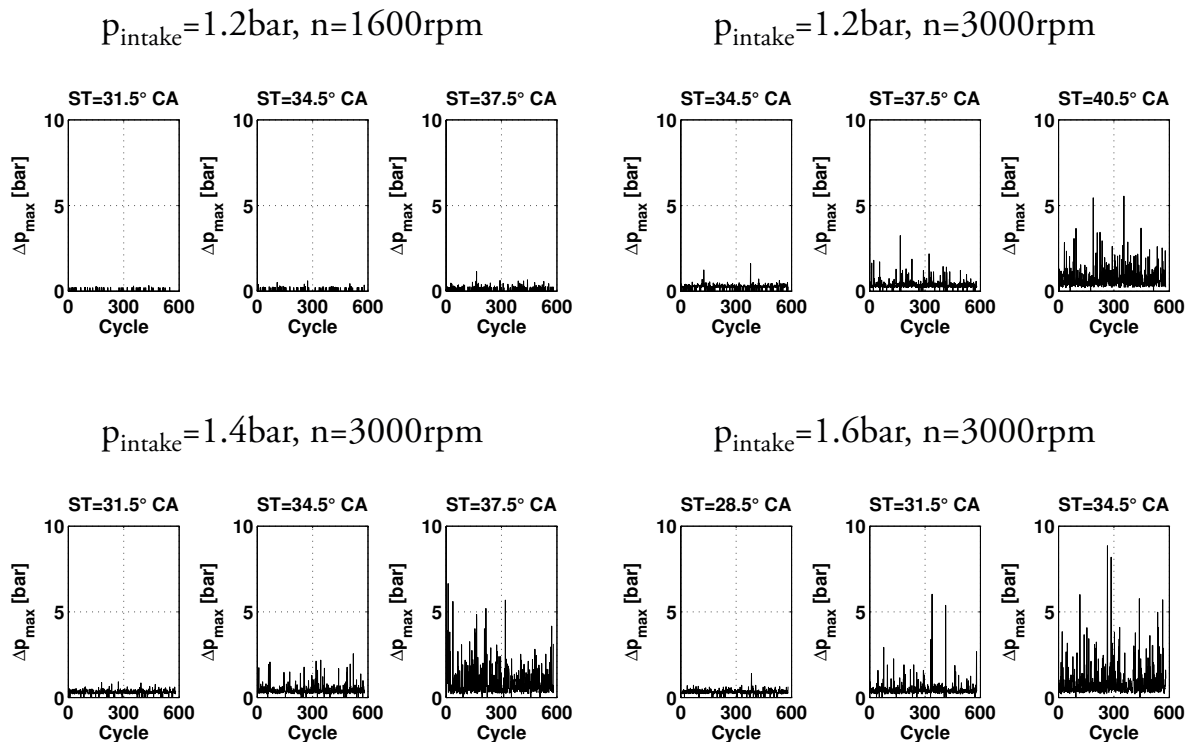

Figure 4.3:   Maximum amplitude of the pressure oscillations for 581 cycles and different spark timings (ST=34.5° CA, ST=37.5° CA, ST=40.5° CA), gas composition G20 and T_{intake}=40°C

It can be seen that knock intensity increases with increasing spark advance as expected. Furthermore, it is observable that some of the cycles knock and some do not. Moreover, the figure indicates that the maximum amplitude of the pressure oscillations is strongly dependent on the operating conditions.

This illustration does not allow a clearly visible correlation between different operating conditions and/or gas compositions. Therefore, statistical methods have been used to characterise knock intensity of one operating point based on the pressure oscillations.

An appropriate method to visualise Δp_{max} is to arrange the data to a frequency distribution plot or - as shown in the following picture - to integrate the resulting frequency distribution and to display as cumulative frequency. The graph contains the data of one operating point and three spark timings.
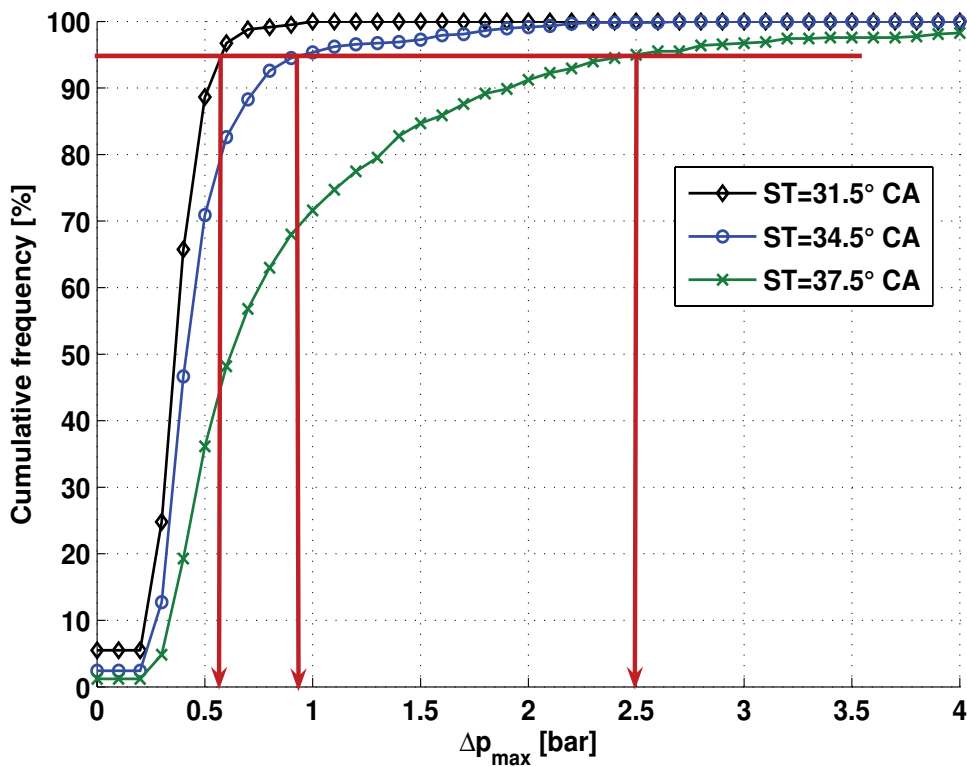

Figure 4.4:   Cumulative frequency plot of the Δp_{max} distribution for operating point G20, p_{intake}=1.4bar, T_{intake}=40°C, n=3000rpm

It can be seen, that less than 6% of the cycles do not knock at all for all spark timings - under the assumption that $\Delta p_{maxcrit}$=0.2bar - and fall below the threshold

value. The curves increase continuously, which means that various values of pressure oscillations - and depending on the knock intensity definition - various knock intensities can be found for one operating point. The „bins" have equidistant width of Δp=0.1bar.

One method to define knock is, that a certain number of cycles have to exceed a critical value of Δp_{max}. The red line in figure 4.4 denotes that 5% of the cycles exceed and 95% of the cycles fall below a threshold value of Δp_{max}. This value is called the 95% quantile and is marked with the arrows for each of the plotted spark timings. It makes sense to define a single value for one measurement to have the possibility to compare different engine conditions.

The following diagram displays the 95% quantiles for all investigated engine speeds at a constant intake pressure of 1.4bar.
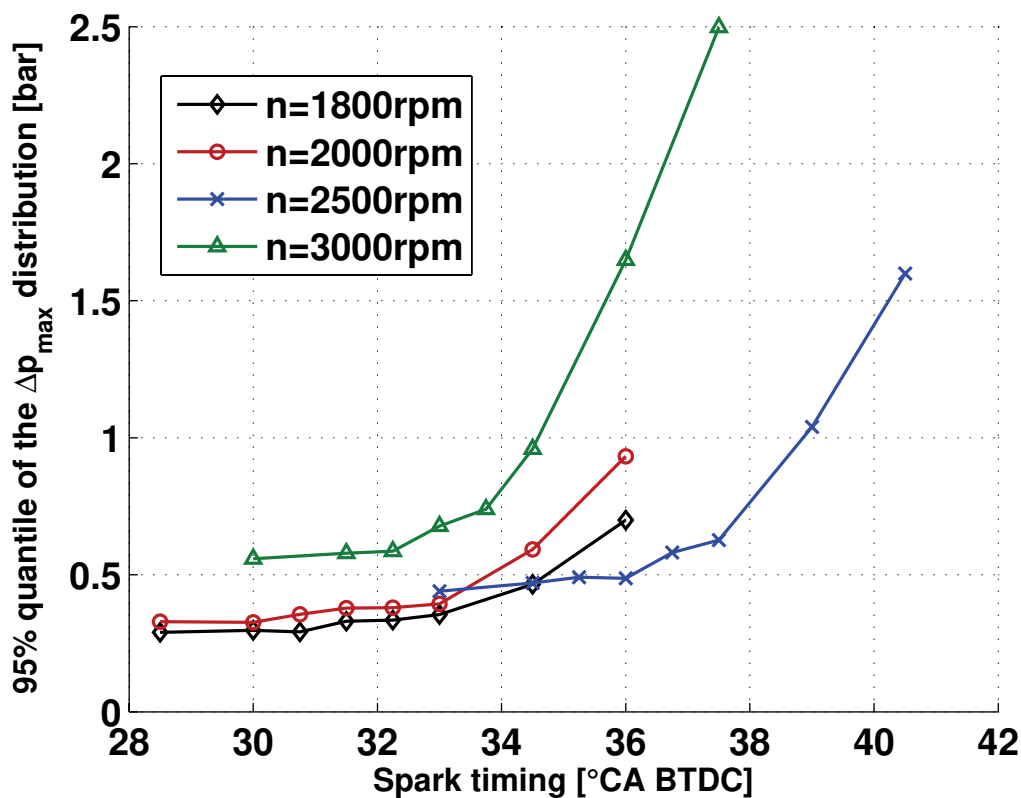
Figure 4.5:   95% quantiles of the Δp_{max} distribution for operating point G20, p_{intake}=1.4bar, T_{inake}=40°C

This investigation clearly shows that the 95% quantiles are dependent on the selected operating point. Figure 4.5 shows that the maximum amplitude of the

pressure oscillations increases with engine speed. In [41] a similar behaviour was found for gasoline engines where the 98.5% quantile was used.

This examination with statistical methods corresponds very well to the subjective impression during the measurements on the test bench. During the experiments the instantaneous cylinder pressure was visualised on an oscilloscope and it was observed, that at low engine speeds, low Δp_{max} occurred where „deformations" of the pressure curve have been very often seen. The following figure shows the heaviest knocking cycle found and two typical knocking cycles for p_{intake}=1.2bar and n=1600rpm.
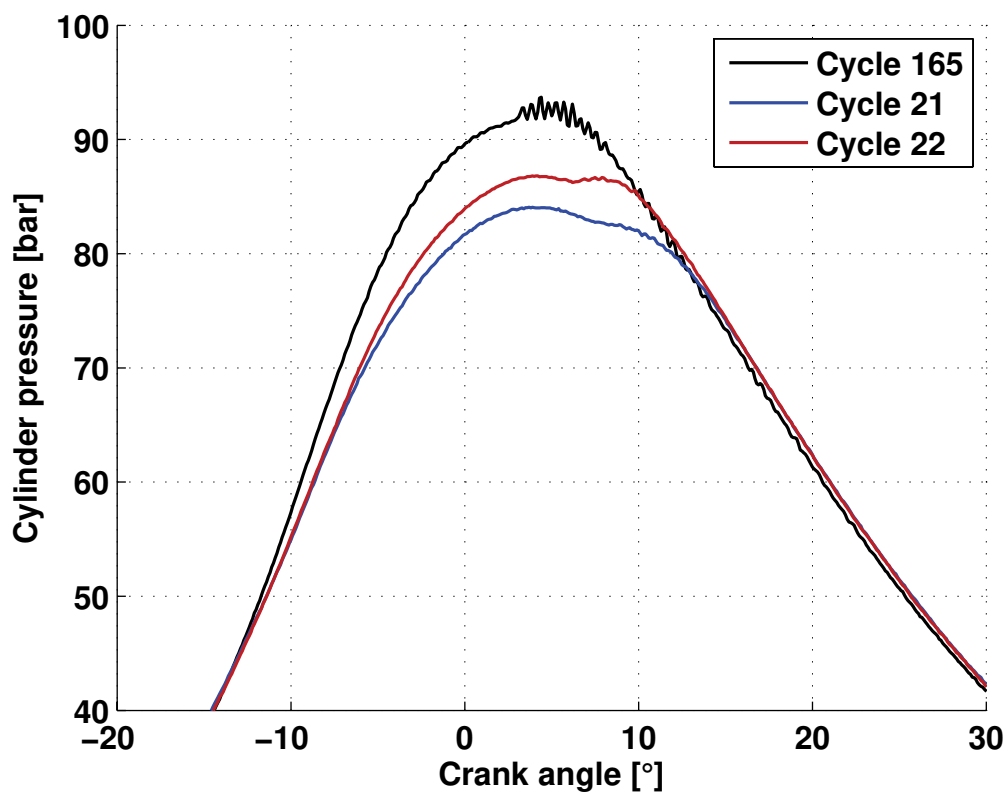
Figure 4.6:   Pressure oscillations at low engine speed, G20, p_{intake}=1.2bar, T_{intake}=40°C, n=1600rpm, spark timing=37.5° CA

As it was often seen in the literature the crank angle of knock occurrence was defined as the first remarkable pressure oscillation. Figure 4.6 clearly indicates that it will be rather challenging to detect the crank angle of knock occurrence reliable based on the pressure signal for low engine speeds.

For these reasons a new knock detection method has been developed which is based on the analysis of the burn rate. The burn rate was investigated because it is the cause of the knock phenomena and the pressure oscillations are the effects. Figure 4.7 shows the burn rate of a heavy knocking cycle, the filtered burn rate and the corresponding cylinder pressure in the upper part. In the lower part of the graph the cumulative burn rate is displayed. Further details of two points have been investigated. On one hand a local minimum and on the other hand a local maximum of the burn rate have been defined as indicated by the dashed lines.
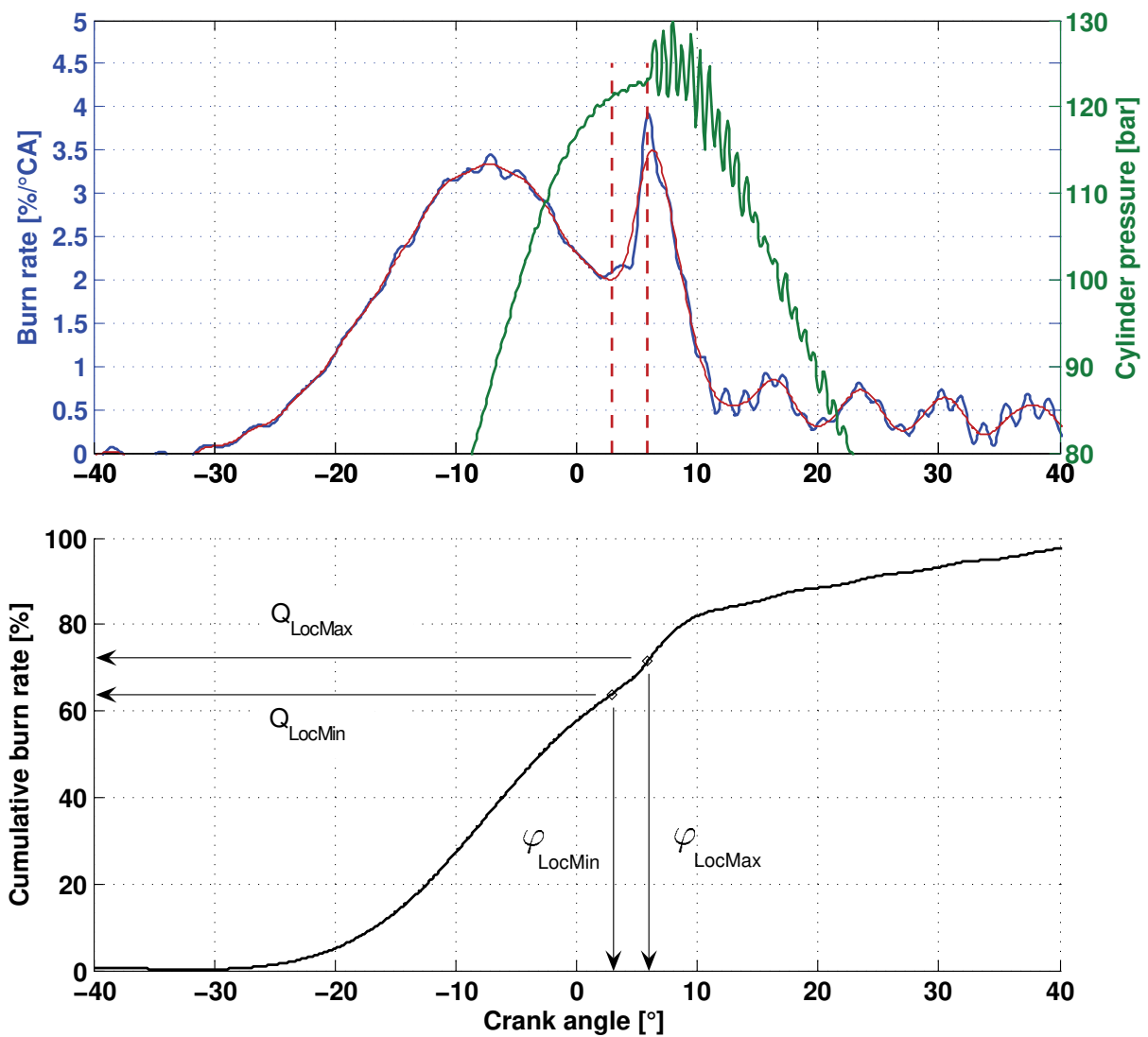

Figure 4.7:   Definition of the knock indicator dQ/dφ$_{LocMinMax}$

It is noticeable that an increase of the burn rate in the late part of the combustion can be observed compared to non-knocking combustion (see for example

figure 2.2 and figure 2.3 for the shape of the burn rate curve in case of non-knocking combustion). This increase indicates the burned mixture due to knock.

The mean burn rate from local minimum to local maximum was calculated. Due to the local variations of the burn rate this gradient has been defined based on the cumulative burn rate which is much more insensitive to experimental fluctuations. This „mean knock burn rate" was introduced to characterise the burn rate due to knock.

$$\frac{dQ}{d\varphi}_{LocMinMax} = \frac{Q_{LocMax} - Q_{LocMin}}{\varphi_{LocMax} - \varphi_{LocMin}} \qquad 4.6$$

Similar to the frequency analysis of the Δp_{max} distribution statistical methods have been used to analyse $dQ/d\varphi_{LocMinMax}$. A frequency distribution was computed and the cumulative frequency has been analysed. The same three spark timings at the same operating point as shown in figure 4.4 are plotted in the following figure.
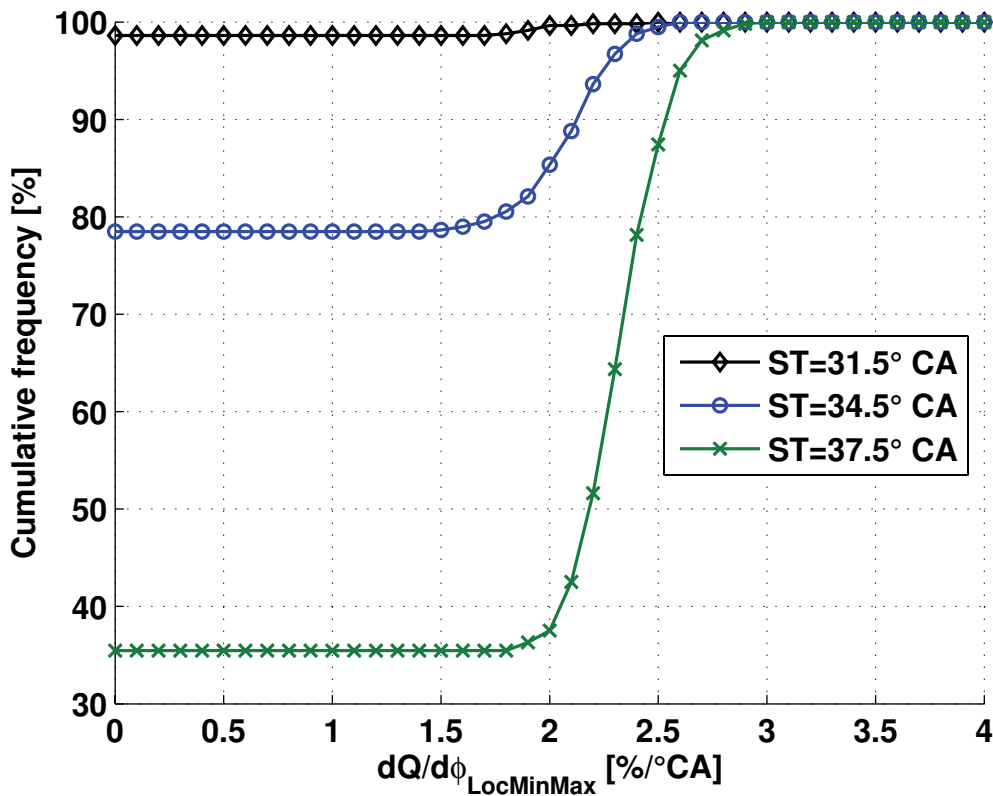

Figure 4.8:   Cumulative frequency plot of $dQ/d\varphi_{LocMinMax}$ for operating point G20, p_{intake}=1.4bar, T_{intake}=40°C, n=3000rpm

Some of the cycles again do not knock. But in contrast to the Δp_{max} distribution, the curves are not continuously increasing. This knock detection method allows a sharp separation between knocking and non-knocking cycles due to the fact that no knocking cycles can be found up to 1.5%/°CA. The curves increase if $dQ/d\varphi_{LocMinMax}$=1.5%/°CA is exceeded. To have a fine resolution the „bins" have a equidistant width of 0.1%/°CA. Analogous to the cylinder pressure examinations a comparison for various operating conditions was found by analysing the 95% quantiles of the $dQ/d\varphi_{LocMinMax}$ distribution. The following graph shows the result for the engine speed variation at p_{intake}=1.4bar similar to figure 4.5.
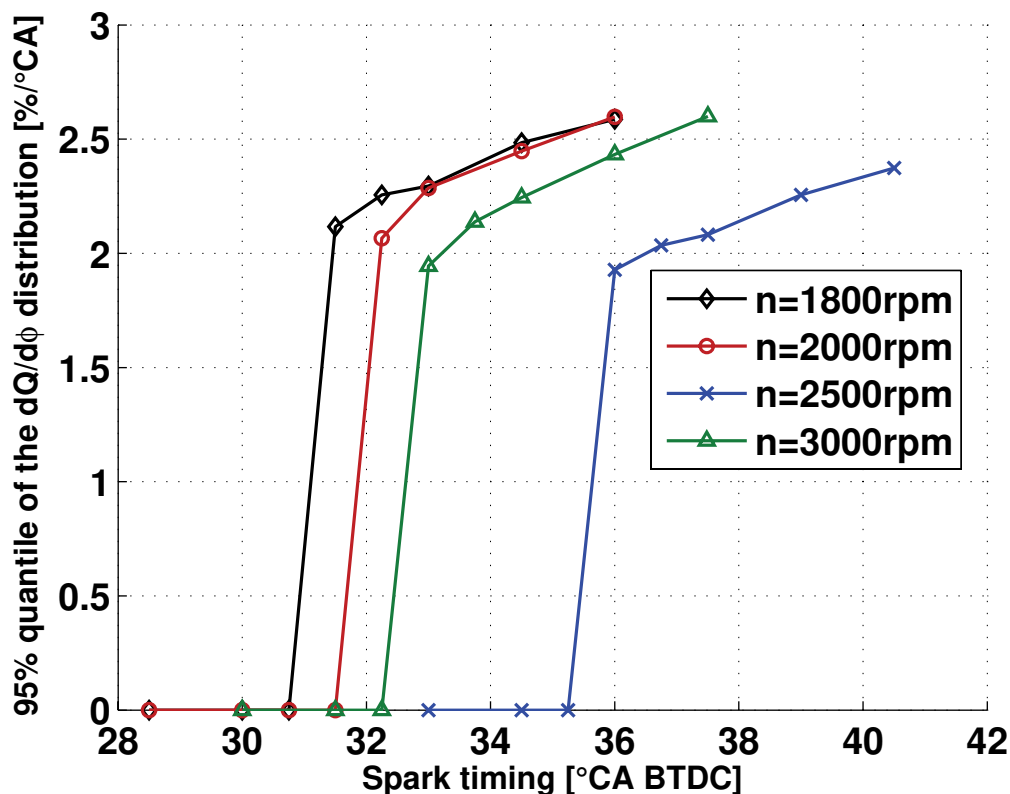
Figure 4.9:   95% quantiles of the $dQ/d\varphi_{LocMinMax}$ distribution for operating point G20, p_{intake}=1.4bar, T_{inake}=40°C

Each of these lines corresponds to one operating point where the markers indicate different spark timings. By analysing one engine speed it can be observed, that the 95% quantiles start at 0%/°CA, increase suddenly and then further increase rather smoothly with later spark timings. A sharp separation between non-knocking and knocking operating points was found where the separation line is independent of the engine speed. Therefore, the knock detection method can be summarised as follows:

CRITERION:

The operating point analysed does knock for a specific spark timing if 5% of the cycles exceed $dQ/d\varphi_{LocMinMax}$***=1.5%/°CA. Taking one operating point, the first 95% quantile exceeding 1.5%/°CA is defined as the spark timing at start of knock.***

Finally, all investigated operating points for one gas composition are plotted in the following figure. This means that the 20 operating points shown in figure 4.2 and all tested spark timings - six to eight depending on the operating point and knock intensity - can be seen where in total 152 measurements have been analysed and plotted for G20. Figure 4.10 clearly shows that this knock detection method is independent of the operating point. The colours indicate the intake temperature (see figure 4.2). The analysis of the other gas compositions can be found in appendix A.3 where it can be observed that this knock detection method is even independent of the fuel composition.
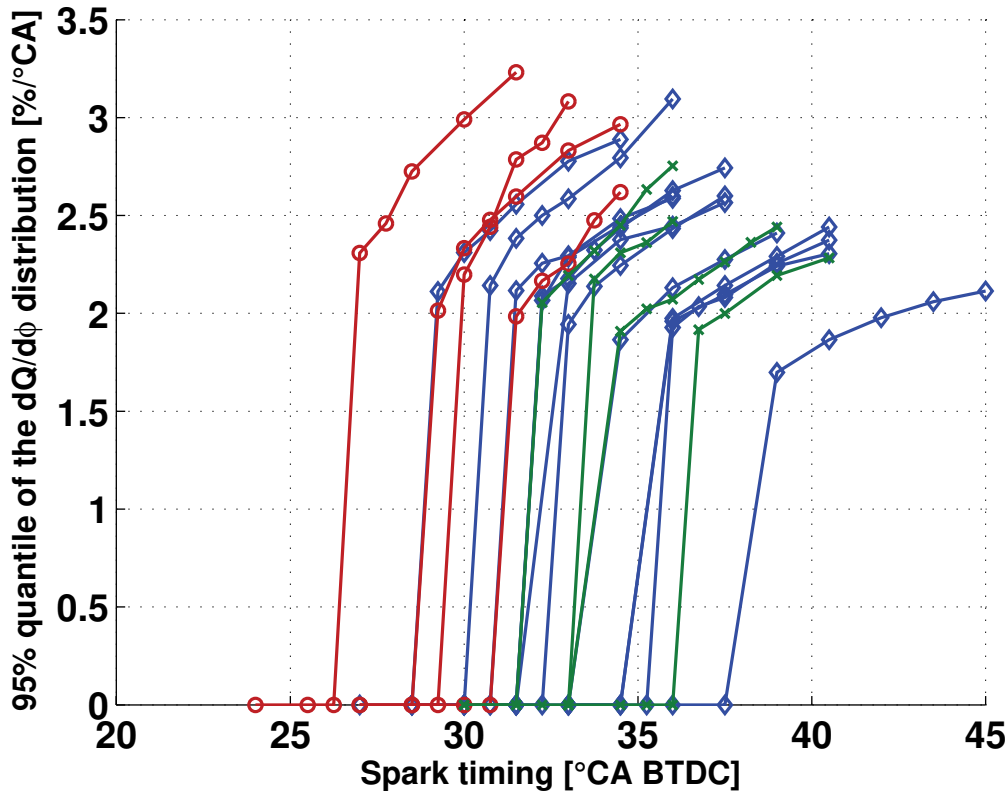

Figure 4.10: *95% quantiles of the* $dQ/d\varphi_{LocMinMax}$ *distribution for all investigated operating points for G20, red:* T_{intake}=60°C, *blue:* T_{intake}=40°C, *green:* T_{intake}=20°C

A global trend can be observed: knock strength seems to increase with later spark timings. By following one line, representing one operating point with its different spark timings indicated by the markers, the expected trends can be seen. The „mean knock burn rate" increases with earlier spark timings.

One of the major advantages of this knock detection method is that for low engine speeds a well-defined start of knock can be found in contrast to the direct pressure signal based method. On the other hand the burn rates for the individual cycles have to be calculated which is a slow process and is computationally expensive. In this work, where the aim is to define the knock parameters as accurate as possible and an off-line application is applied, the computing time is secondary.

As shown earlier in figure 4.6, it is challenging to detect the crank angle of knock occurrence based on the pressure signal. The following diagram shows the burn rate curves for the same conditions, where the local minima and therefore the crank angle of knock occurrence can be defined for these individual cycles.
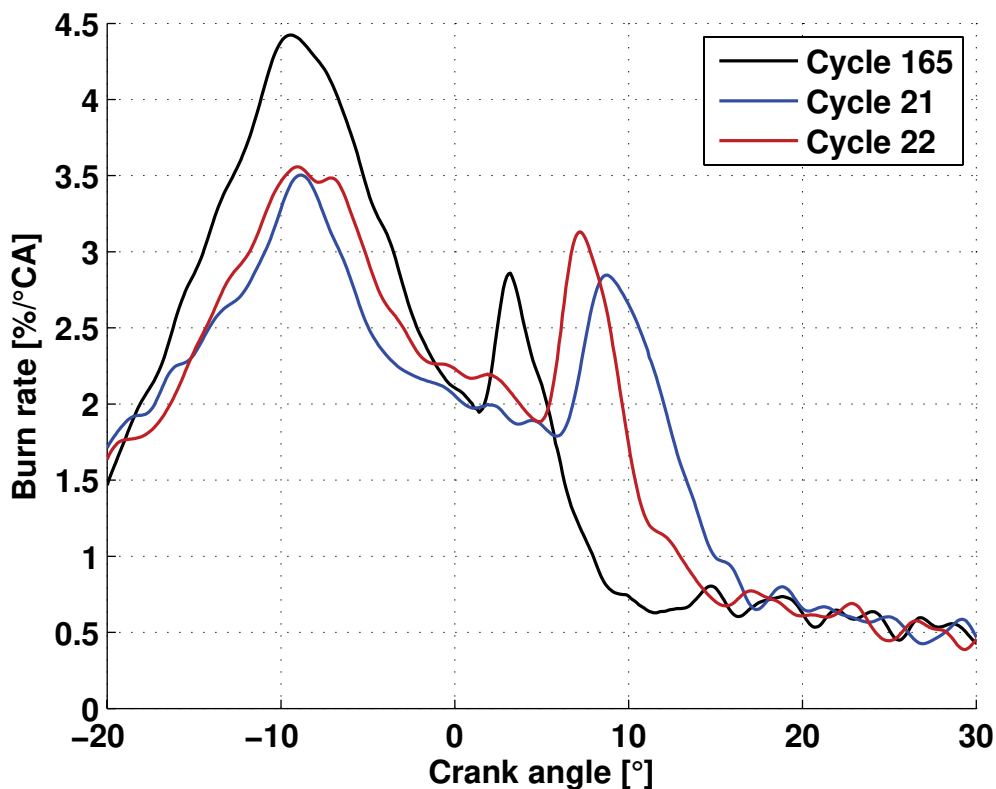

Figure 4.11: Burn rate curves for knocking combustion at low engine speed for G20, p_{intake}=1.2bar, T_{intake}=40°C, n=1600rpm, spark timing=37.5° CA

4.4   Sensitivity Analysis

During the development process of the new knock detection method two parameters have been investigated separately. To localise the local minimum and the local maximum filtered burn rate curves have been used. A lowpass Butterworth filter [113] was used for this application due to its flat passband response. Therefore the filter parameters - the cut-off frequency and the order of the filter - of a Butterworth filter have been varied.

Furthermore, some of the cycles show „mean knock burn rates" which can be either knock or experimental uncertainties whereas a threshold value for the difference of the burn rate at local maximum and the burn rate at local minimum was introduced.

The data analysis was performed using a filter algorithm [113] combined with a Butterworth filter. The filter algorithm applies the filter to the signal in the forward direction, reverses the filtered sequence and then runs back through the filter to obtain zero phase distortion.

Meaningful filter parameter ranges have been estimated first whereon different setups have been tested and the effect on the crank angle of knock occurrence – the crank angle of the local minimum – was investigated. Figure 4.12 shows the mean crank angle of knock onset for different orders and normalised cut-off frequencies for one representative operating condition.

The range for the crank angle of knock occurrence was found to be within 2 degrees crank angle for all combinations of filter parameters investigated, where in most cases the difference is within half a degree. A small dependence on the order of the filter can be observed where, as expected, the cut-off frequency is more important.

Starting at a normalised frequency of 0.1 the crank angle of knock onset occurs slightly earlier before it increases again near the chosen boundary. Based on this graph the decision for the cut-off frequency can not be well-defined whereas the filter order was set as low as possible. Finally, the order of the filter was set to 3 to avoid the variations observed for lower orders in some frequency ranges.

A lot of single burn rate curves for individual cycles for various operating conditions and filter parameters have been plotted to obtain more information about the filter applied. Priorities have been defined for the filter algorithm. First, the detection of the local minimum must be reliable and second the shift of the detected

crank angle at local minimum should be as small as possible. These observations have lead to a normalised cut-off frequency of 0.05. It should be underlined once again, that the variations are within an acceptable range of 0.5° CA as it can be seen from figure 4.12 and it was observed that for lower engine speeds this range decreased.
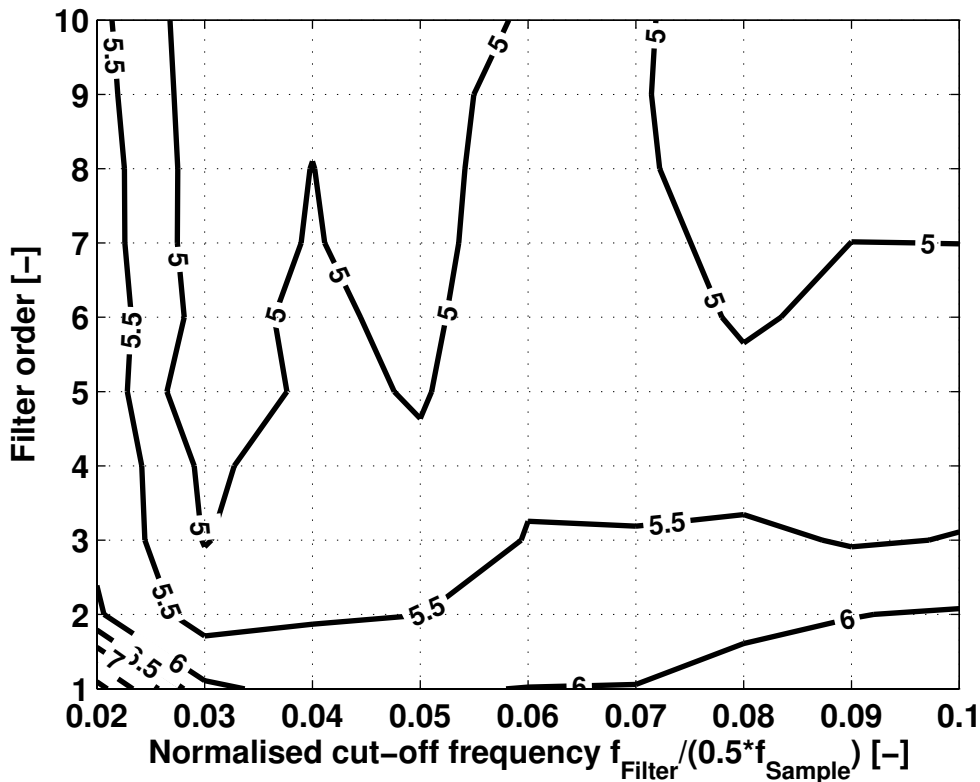
Figure 4.12: Dependence of the mean crank angle of knock occurrence [°CA ATDC] on the filter parameters

As mentioned earlier, a second parameter was investigated separately. After detecting the local minimum and local maximum the „mean knock burn rate" is computed and compared with a threshold value. This threshold value, the critical „mean knock burn rate", was defined as

$$\Delta\frac{dQ}{d\varphi}_{crit} = \frac{dQ}{d\varphi}_{LocMax} - \frac{dQ}{d\varphi}_{LocMin} \qquad 4.7$$

A graphical representation of this critical value is given in figure 4.13.

This value was introduced because in some cases it was not easy to distinguish whether the „mean knock burn rate" occurred due to experimental variations or due to knock. Figure 4.13 shows one of these „critical" burn rate curves and the threshold value definition. This cycle has a „mean knock burn rate" of 2.57%/°CA and Δp_{max} is 0.18bar.
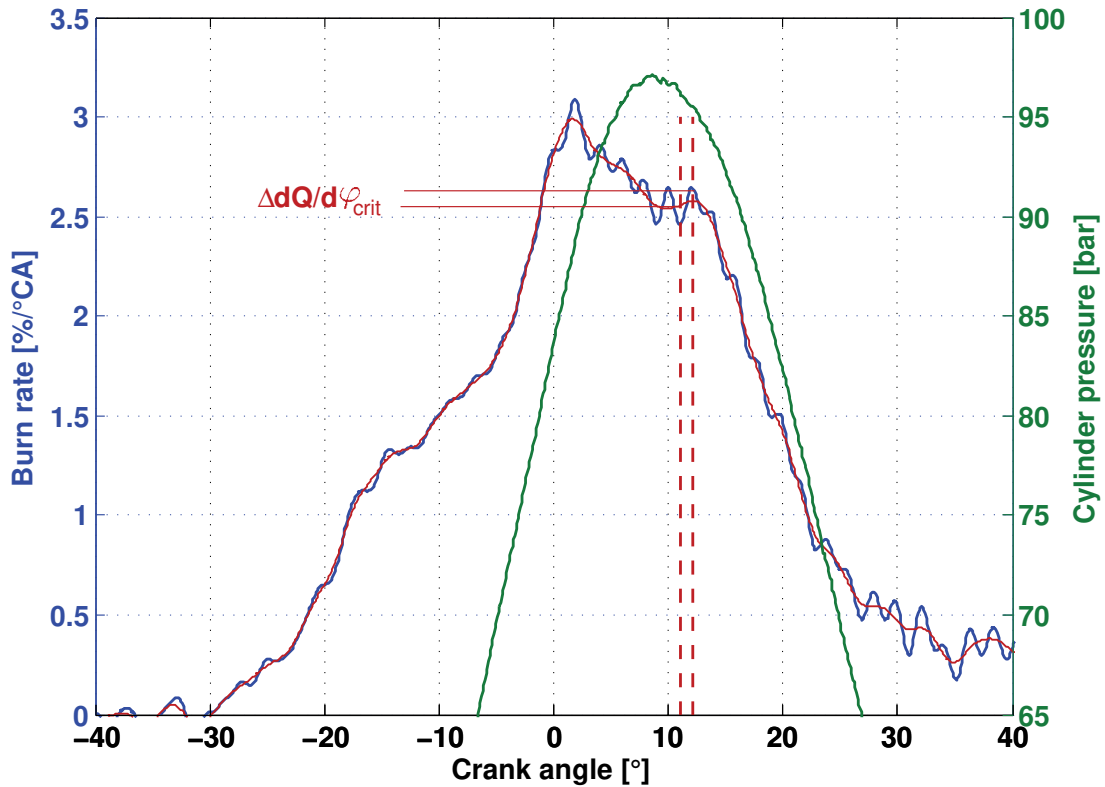
Figure 4.13: Definition of the threshold value for $dQ/d\varphi_{LocMinMax}$

The critical „mean knock burn rate" was defined based on the filtered curve and can be used to adjust the knock intensity. Figure 4.14 displays the resulting spark timing at start of knock - based on the definition shown in figure 4.9 - as a function of the threshold value.

It can be seen that if $\Delta dQ/d\varphi_{crit}$ is increased the resulting spark timing at start of knock increases, which means that knock occurs at earlier spark timings. The knock model is supposed to indicate whether knocking combustion starts and not to indicate heavy knocking operating conditions. Therefore, $\Delta dQ/d\varphi_{crit}$ was set to 0.4%/°CA here to ensure a clearly defined differentiation between knocking and non-

knocking operating points on one hand and on the other hand to indicate start of knocking combustion.

Figure 4.14: Spark timing at start of knock as a function of $\Delta dQ/d\varphi_{crit}$, operating point used: G20, $p_{intake}=1.4bar$, $T_{intake}=40°C$, n=3000rpm

4.5   Data Analysis

4.5.1 Spark Timing at Start of Knock

The new knock detection method was applied to define the spark timings at start of knock for all operating points and gas compositions investigated. On the left hand side of figure 4.15 the spark timi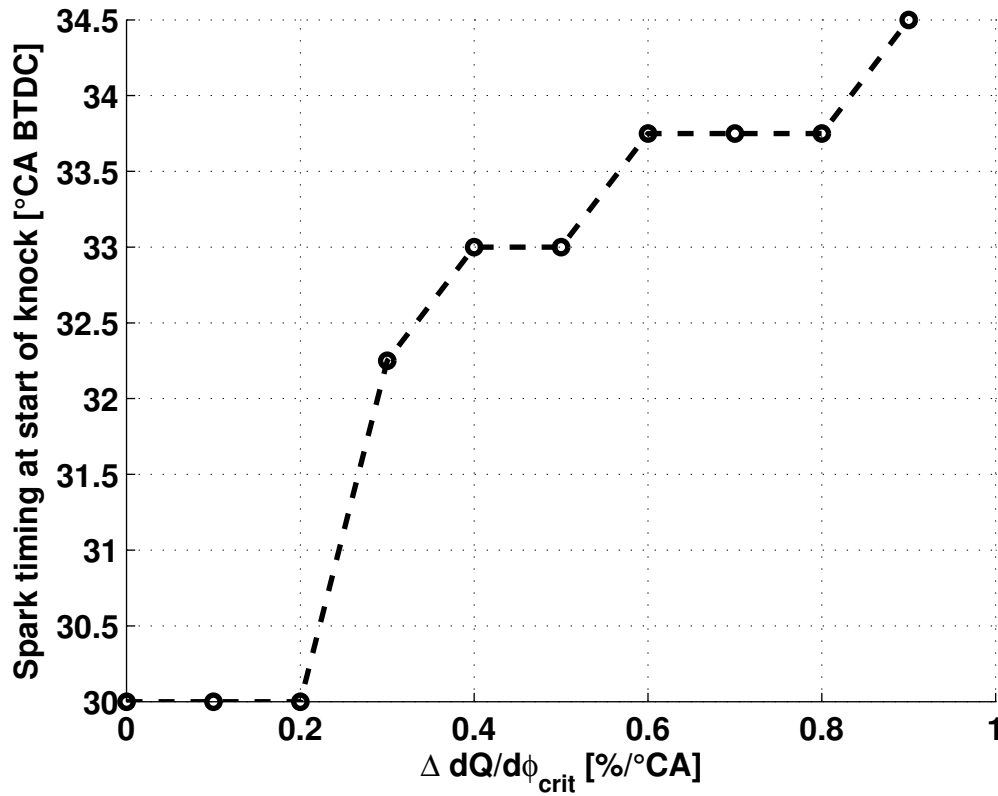ngs at start of knock are summarised for G20 and T_{intake}=40°C. On the right hand side of figure 4.15 the same procedure was applied to T_{intake}=20°C and T_{intake}=60°C.
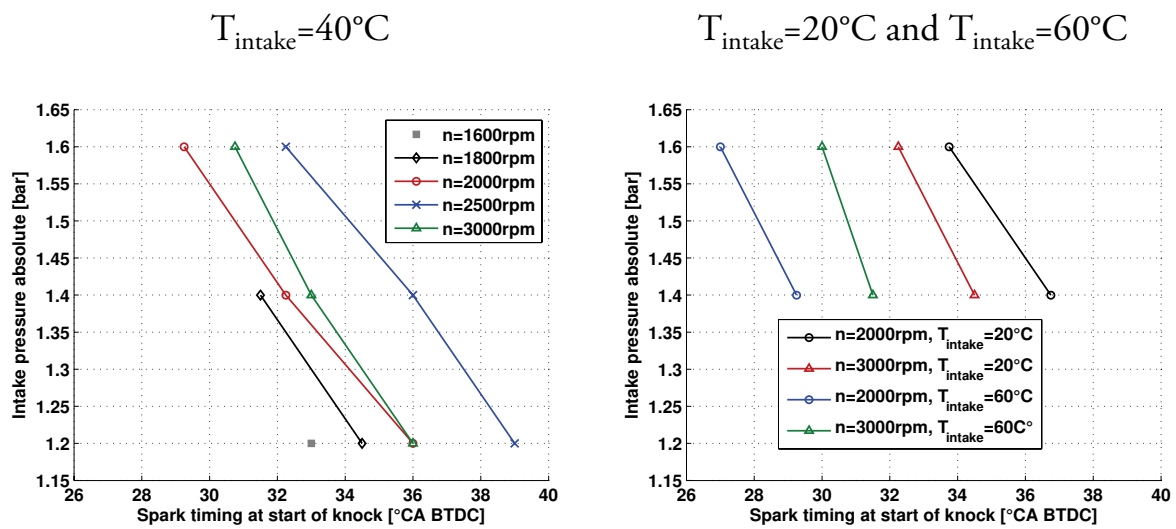
Figure 4.15: Spark timings at start of knock, G20 and different operating points

It follows from figure 4.15 that as the intake pressure is increased, the spark timing for knock occurrence has to be retarded, as expected. Moreover, it can be summarised that the higher the engine speed, the earlier the spark timing at start of knock can be applied. For all the measurements carried out, n=2500rpm behaved different where an increased spark advance had to be chosen. It was found, that the volumetric efficiency was lower for n=2500rpm than for the other engine speeds for the same conditions in the intake manifold. The right diagram indicates, that later spark timings have to be chosen if the intake temperature increases, as expected too. The behaviour on engine speed is reversed for T_{intake}=20°C what is surprising.

The methane number (MN) definition described in [69] has been tested to visualise the spark timing at start of knock as a function of the gas composition, but

no meaningful result was obtained for G25 containing 14% N_2 by volume. Thus, the methane mass fraction was used as base. If ethane or propane content increases, spark timings have to be retarded to lower the temperature in the unburned mixture and the pressure in the combustion chamber for knock tendency to remain the same. The dilution with N_2 leads to increased knock resistance as the earlier drivable spark timings indicate.
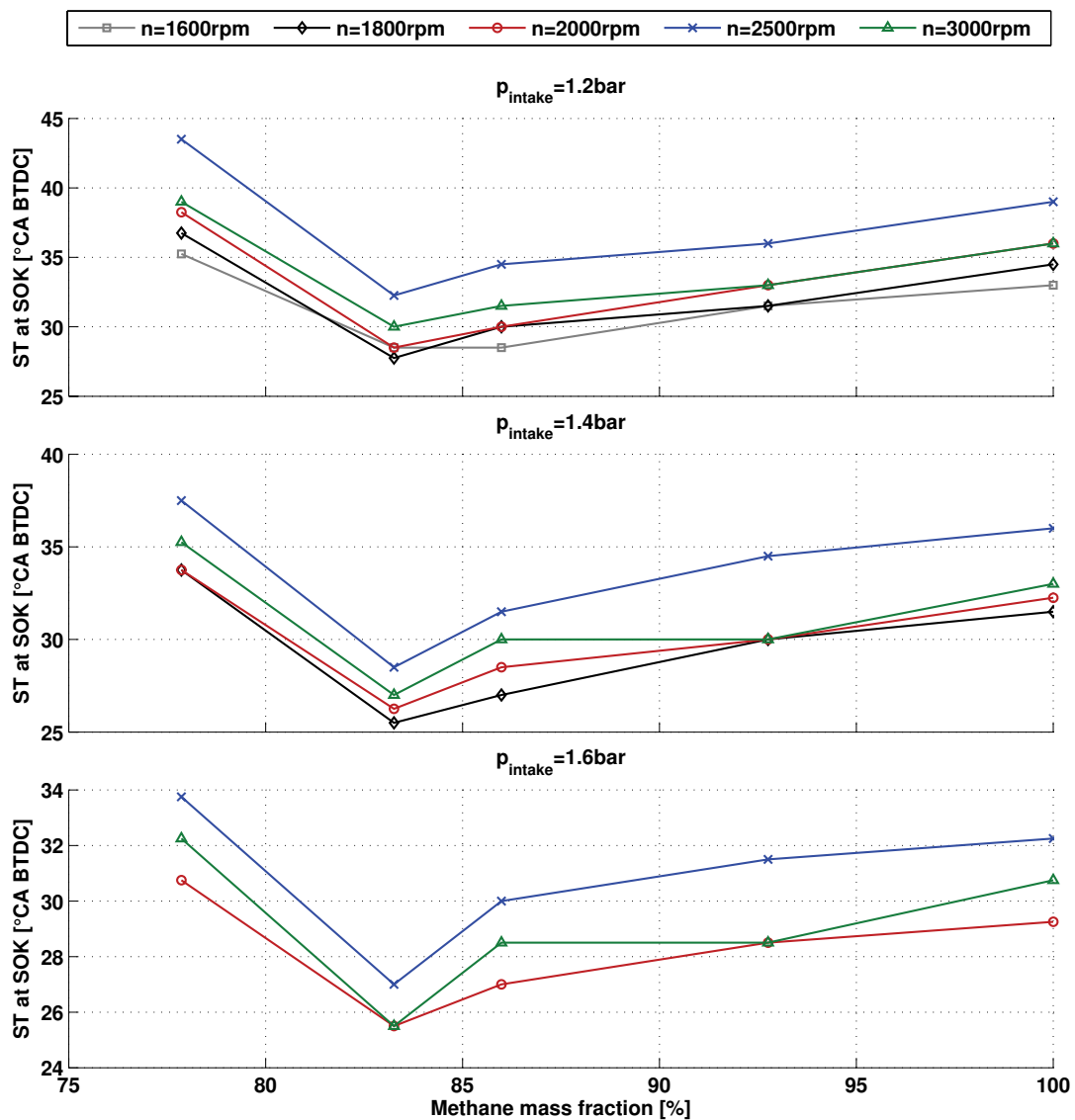
Figure 4.16: Spark timings at start of knock for different intake pressures and engine speeds as a function of the methane mass fraction of the fuel, $T_{intake}=40°C$

It is noticeable that for G4E - which has a methane mass fraction of 92.76% - some spark timings at start of knock are identical for different engine speeds. It has to be taken into account that the resolution of the spark timing variation is limited and so the uncertainty is almost one crank angle degree. Nevertheless, the general trends are as expected.

4.5.2 Knock Frequency Analysis

A fast Fourier transform was applied to determine the frequency components of the pressure signal, whereas each cycle for all investigated operating points has been analysed. The frequency, where the maximum magnitude occurred, was stored and found to be constant for all operating points investigated. This finding confirms the expectation that knock frequency is equal to the resonance frequency of the combustion chamber. The following figure displays the results obtained for one heavy knocking operating condition.
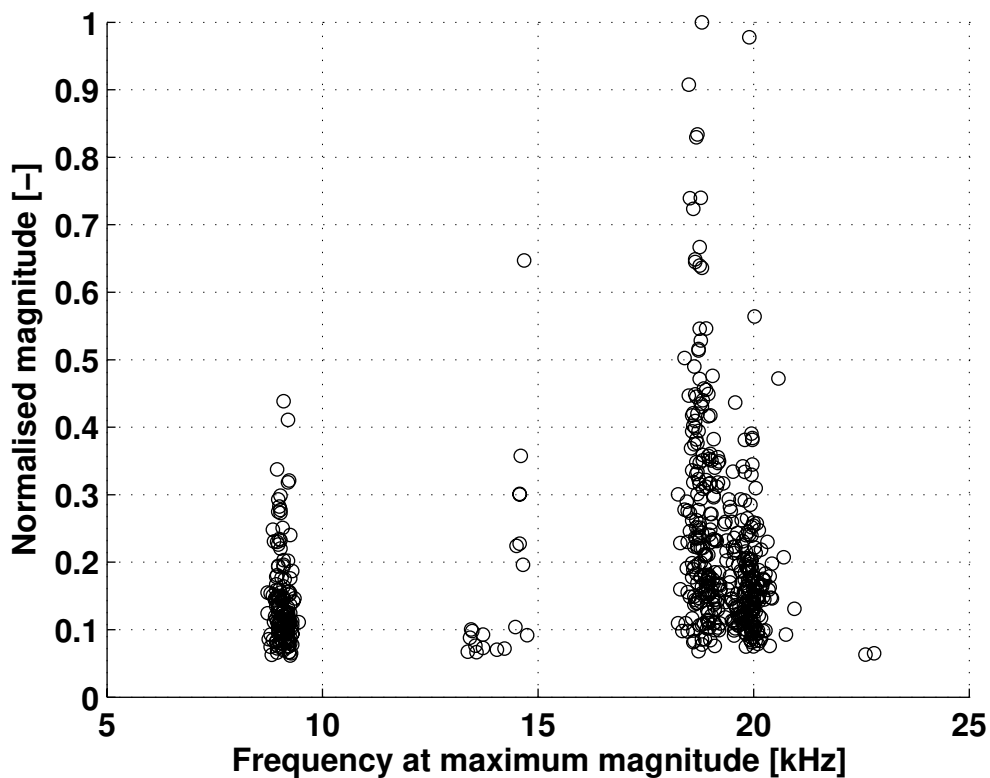
Figure 4.17: Fast Fourier transform for G20, p_{intake}=1.4bar, T_{intake}=40°C, n=3000rpm, ST=37.5° CA, 581 individual cycles

Most of the pressure waves analysed have a characteristic frequency of about 18.8kHz, where some frequency components can be found around 9.2kHz. Further modes can be observed at about 14.5kHz and 20kHz.

It can be shown that the maximum magnitude of the frequency components and the maximum amplitude of the pressure oscillations correlate well. Theoretical considerations describe the knock frequency as a function of the bore [5, 41].

It is noticeable that the highest magnitudes occur out of the range of audibility but anyhow, the typical sound of knocking combustion was heard during the tests, what may be a consequence of the magnitudes around 9.2kHz.

The speed of sound can be estimated based on the temperatures in the combustion chamber. Taking the mean temperature at start of knock - meaning that a typical value is T_{mean}=2000K - and assuming that κ=1.25 and R=300J/kgK leads to

$$c_{Tmean} = \sqrt{\kappa R T_{mean}} \approx 866\,m/s \qquad 4.8$$

The knock frequency can be estimated by assuming radial and azimuthal modes. The axial modes change due to the moving piston and are neglected here, because knock occurs near top dead centre. It was assumed that knock occurs near the wall and therefore, the bore and the circumference of the combustion chamber have been used as characteristic lengths for the radial and azimuthal modes, respectively. This leads to the following simplified formulation:

$$f_n = n_f \cdot \frac{c_{Tmean}}{2R_{cyl}}$$

$$4.9$$

$$f_m = m_f \cdot \frac{c_{Tmean}}{2\pi R_{cyl}}$$

The harmonics appearing in an oscillating system are described by the parameters n_f and m_f. Based on equation 4.9 and together with the speed of sound the frequencies for various modes can be estimated. These resulting frequencies are displayed in figure 4.18.

It seems, that the frequency components at 9.2kHz and 20kHz result from the azimuthal mode for m_f=2.5 and m_f=5, whereby the radial mode for n_f=1.5

corresponds to 18.8kHz, if it is assumed, that the estimated frequencies are slightly too high.

It has to be taken into account, that the mean speed of sound is difficult to determine and the combustion chamber shape was simplified. Furthermore, the place of knock occurrence is unknown and was assumed to occur at the cylinder liner here.
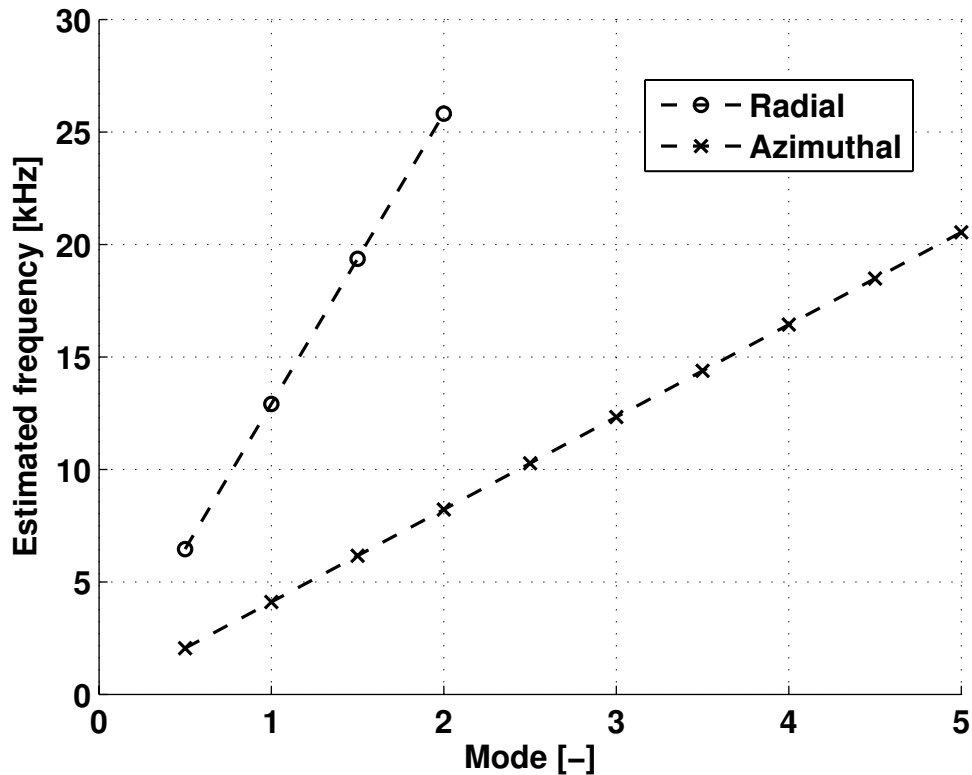
Figure 4.18: Knock frequency estimation by approximating the speed of sound and by assuming radial and azimuthal modes in the combustion chamber

4.5.3 Combustion Progress Variable at Knock Onset

The unburned gas mass fraction at knock onset has been investigated by several researchers. Due to the boundary layer a critical combustion progress can be found where knock can occur latest. Boulouchos and Eberle [16] developed a simple correlation for the thermal boundary layer as a function of the stroke. Soltic [101] applied this approach to determine the upper integration limit of the knock integral.

$$\delta_{BL} = 0.0048 \cdot S^{0.68} \qquad\qquad 4.10$$

where S is the stroke and δ_{BL} the boundary layer thickness, both in meters. For the engine used in this work the boundary layer thickness is therefore roughly 0.8mm.

The following figure shows the mean $dQ/d\varphi_{LocMinMax}$ as a function of the mean unburned gas mass fraction at knock onset for all knocking operating conditions of one gas composition.
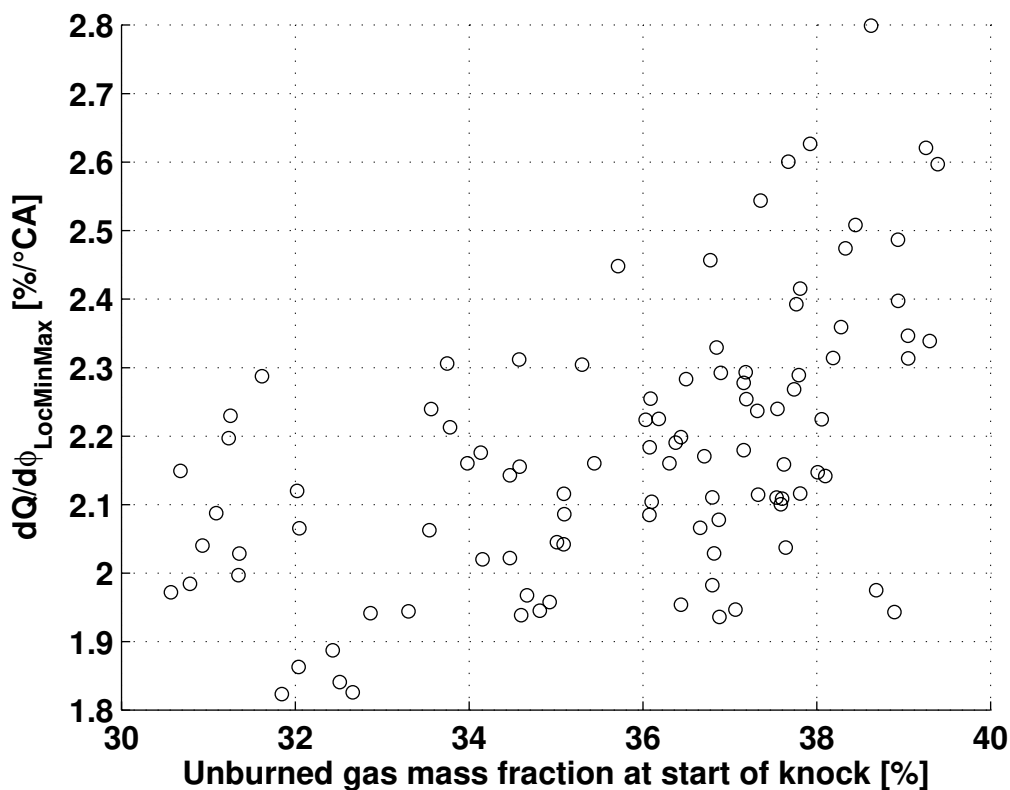
Figure 4.19: Knock intensity as a function of the unburned gas mass fraction based on experimental data, G20

Mean values have been used here to compare all the investigated operating conditions in one diagram and have been computed by taking the average of the individual values of each cycle, whereas only the knocking cycles have been considered. The unburned gas mass fraction was detected at local minimum.

For all investigated operating conditions 30 to 40 percent of the unburned gas mass is remaining when knock occurs. This finding is in good agreement with the observations reported by Franzke [43] who found that knock occurs only up to a combustion progress of $x_B=0.75$. A general trend can be observed concerning knock strength. Knock intensity increases with increasing unburned gas mass fraction at knock onset. But figure 4.19 further indicates that some more effects seem to be important because the correlation can be observed, but it is rather weak. The influences on $dQ/d\varphi_{LocMinMax}$ could not completely be explained.

The thickness of the remaining unburned zone at start of knock, which can be interpreted as the distance from the flame to the wall δ_{FW}, can be estimated by assuming an annulus:
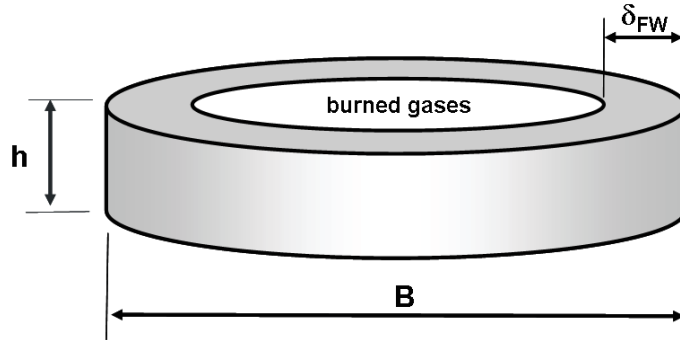
Figure 4.20: Definition of the flame-wall distance δ_{FW} at start of knock by assuming a disc shaped flame propagation

The volume of the remaining unburned zone is

$$V_U = [B^2 - (B - 2\delta_{FW})^2] \cdot \frac{\pi}{4} \cdot h \qquad\qquad 4.11$$

The instantaneous combustion chamber height h can be expressed as a function of the cylinder volume V_{cyl} and the bore B by $h = (4V_{cyl})/(B^2\pi)$. It follows that

$$V_U = [B^2 - (B - 2\delta_{FW})^2] \cdot \frac{V_{cyl}}{B^2} \qquad\qquad 4.12$$

After introducing $V_U = m_U / \rho_U$ - where m_U denotes the mass and ρ_U is the density of the unburned mixture - the distance between flame and wall at start of knock can be derived by solving equation 4.12 for δ_{FW}.

$$\delta_{FW} = \frac{B}{2} \cdot \left[1 - \left[1 - \frac{m_U}{\rho_U} \cdot \frac{1}{V_{cyl}} \right]^{0.5} \right] \qquad\qquad 4.13$$

If the volume of the combustion chamber is replaced by the total cylinder mass and the mean combustion chamber density $V_{cyl} = m_{cyl} / \rho$ and if the combustion progress variable $m_U / m_{cyl} = 1 - x_B$ is introduced, δ_{FW} can be expressed as a function of x_B.

$$\delta_{FW} = \frac{B}{2} \left[1 - \left[1 - \frac{\rho}{\rho_{FW}} (1 - x_B) \right]^{0.5} \right] \qquad\qquad 4.14$$

The mean temperature of the remaining unburned zone was defined by the average of the wall temperature and the temperature of the unburned mixture. The density in the remaining unburned zone was defined based on this averaged temperature. This is a simplification and includes the assumption that the low wall temperature is of importance for the density distribution within this zone.

The density in the remaining unburned zone is about 33% higher than the density of the unburned mixture calculated with the burn rate analysis and about twice the mean density.

Figure 4.21 shows δ_{FW} at start of knock as a function of the unburned gas mass fraction at start of knock.

The analysis of the individual cycles and figure 4.19 showed that these results agree well with the critical combustion progress of 75% reported by Franzke - which leads to $\delta_{FW} \approx 1\,mm$ - and the boundary layer correlation shown in equation 4.10 for the engine used in this work although the correlations are weak. Here, knocking combusting still occurs if the unburned gas mass fraction approaches 70% as it can be seen in figure 4.19.
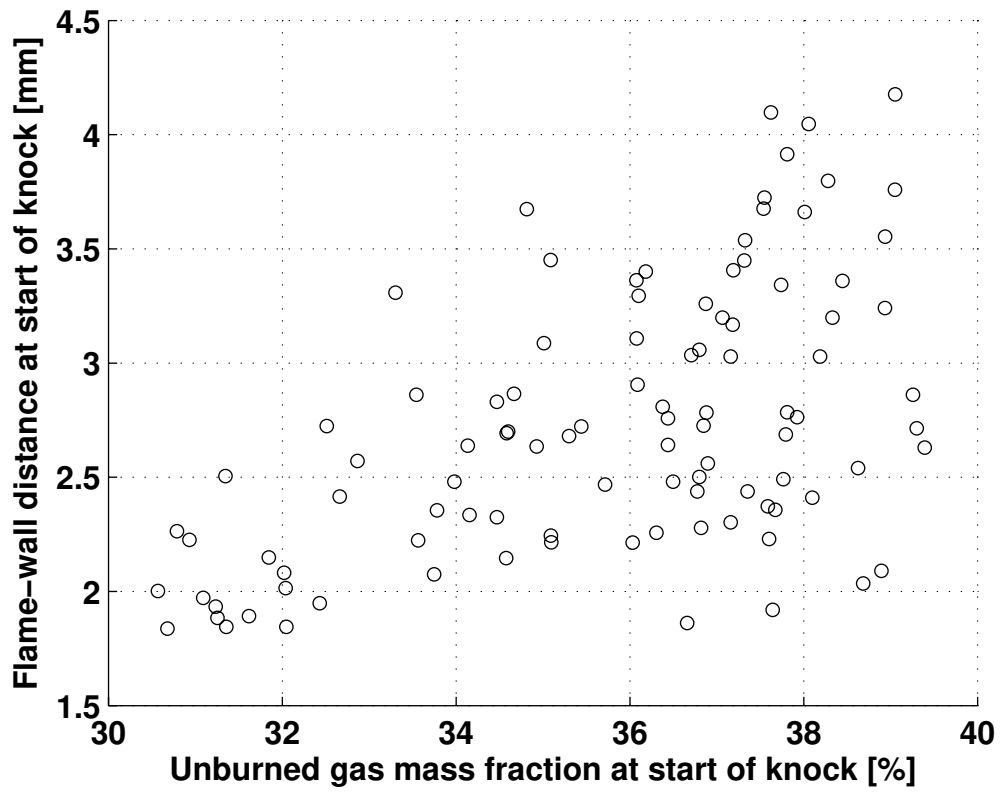
*Figure 4.21: Flame-wall distance at start of knock as a function of the un-
burned gas mass fraction at start of knock*

4.5.4 Knock Behaviour as a Function of Engine Speed

As already mentioned in this chapter the engine speed is one of the key parameters. The maximum amplitude of the pressure oscillations is strongly dependent on the engine speed and it can be shown that the „mean knock burn rate" increases with increasing engine speed, if it is plotted in %/s. The following diagram displays the maximum amplitude of the pressure oscillations Δp_{max} as a function of $dQ/dt_{LocMinMax}$ in %/s. The individual cycles of three heavy knocking operating conditions have been plotted in figure 4.22.
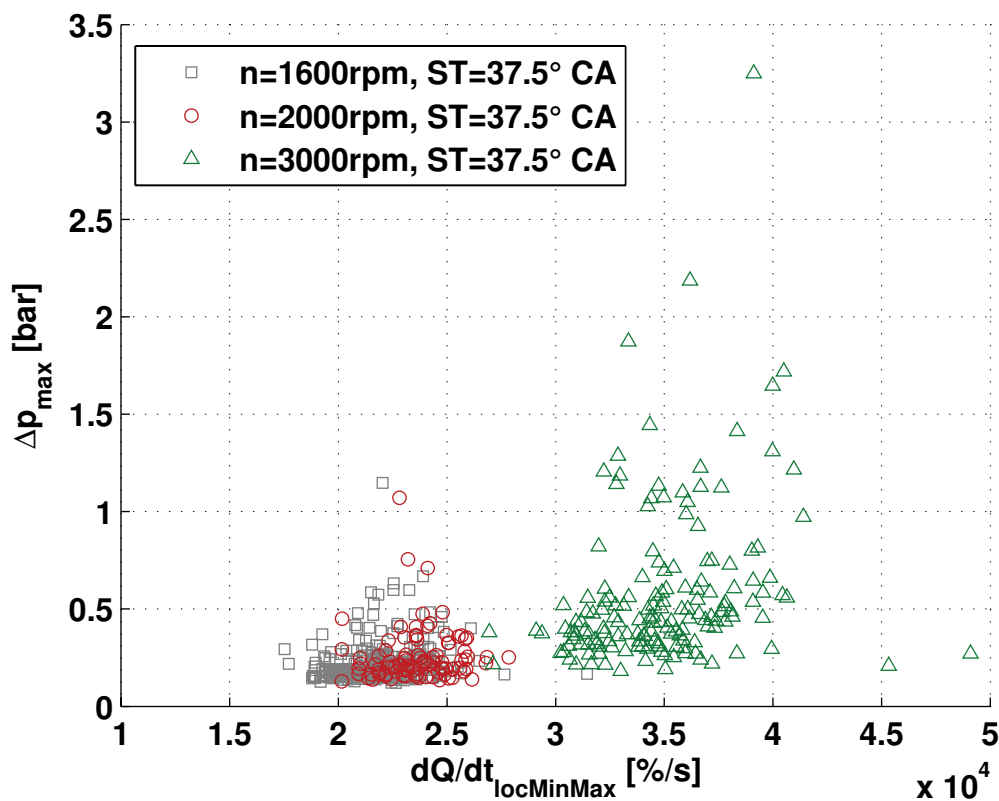
Figure 4.22: Δp_{max} as function of $dQ/dt_{LocMinMax}$ in %/s for three operating conditions and their individual cycles (581 per operating point), p_{intake}=1.2bar, T_{intake}=40°C

It can be seen that $dQ/dt_{LocMinMax}$ increases for increasing engine speed if plotted in %/s. Furthermore, it seems that high „mean knock burn rates" lead to high Δp_{max}, in general.

In principal, two types of combustion can be distinguished. On one hand a chemical kinetic driven combustion in a homogenous reactor can occur, on the other

hand flame propagation as shown in chapter 3 may be observed. Simplified models have been used to investigate knocking combustion for both combustion types.

The combustion in a homogenous reactor for a one step chemistry approach can be approximated as

$$\frac{dQ_B}{dt} \sim \frac{1}{\tau_{reac}} = (x_{Bcrit} - x_B)^\beta \cdot \frac{1}{A} \cdot \left(\frac{p_{cyl}}{p_0}\right)^\alpha \cdot e^{-T_A/T} \qquad 4.15$$

In this formulation the knock integral method approach developed in chapter 4.6 is used. Based on the flame propagating formulation shown in chapter 3.3 the burn rate can be expressed as

$$\frac{dQ_B}{dt} \sim S_T = S_L + S_L^{1-n_{ST}} \cdot A_G \cdot \left(\frac{li \cdot \rho_U}{\eta(T_U)}\right)^{m_{ST}} \cdot u'^{n_{ST}+m_{ST}} \qquad 4.16$$

While the chemical kinetic driven combustion is - in general - independent of the engine speed, the turbulent flame speed increases with increasing engine speed because $u' \sim s_{mp}$, if s_{mp} is the mean piston speed. It should be noted that - due to the higher wall temperatures - the temperature of the unburned mixture may be slightly higher with increasing engine speed and therefore higher reaction rates may result for the homogenous reactor.

The „flame propagation hypothesis" was tested by describing the burn rate based on the overall burn duration t_{BD} taken from the experimentally determined cumulative burn rate:

$$\overline{\frac{dQ_B}{dt}} \sim \frac{1}{\tau_{BD}} \qquad 4.17$$

The simplified models described in equation 4.15 and 4.17 have been used to discuss the type of combustion. The first operating point analysed has been used as reference and so both approximations have been normalised by this reference point.

Figure 4.23 shows the results for both models as a function of the normalised experimentally determined „mean knock burn rate". All these investigations have been performed using the averaged cycles where the 20 operating points at start of knock for G20 are displayed.
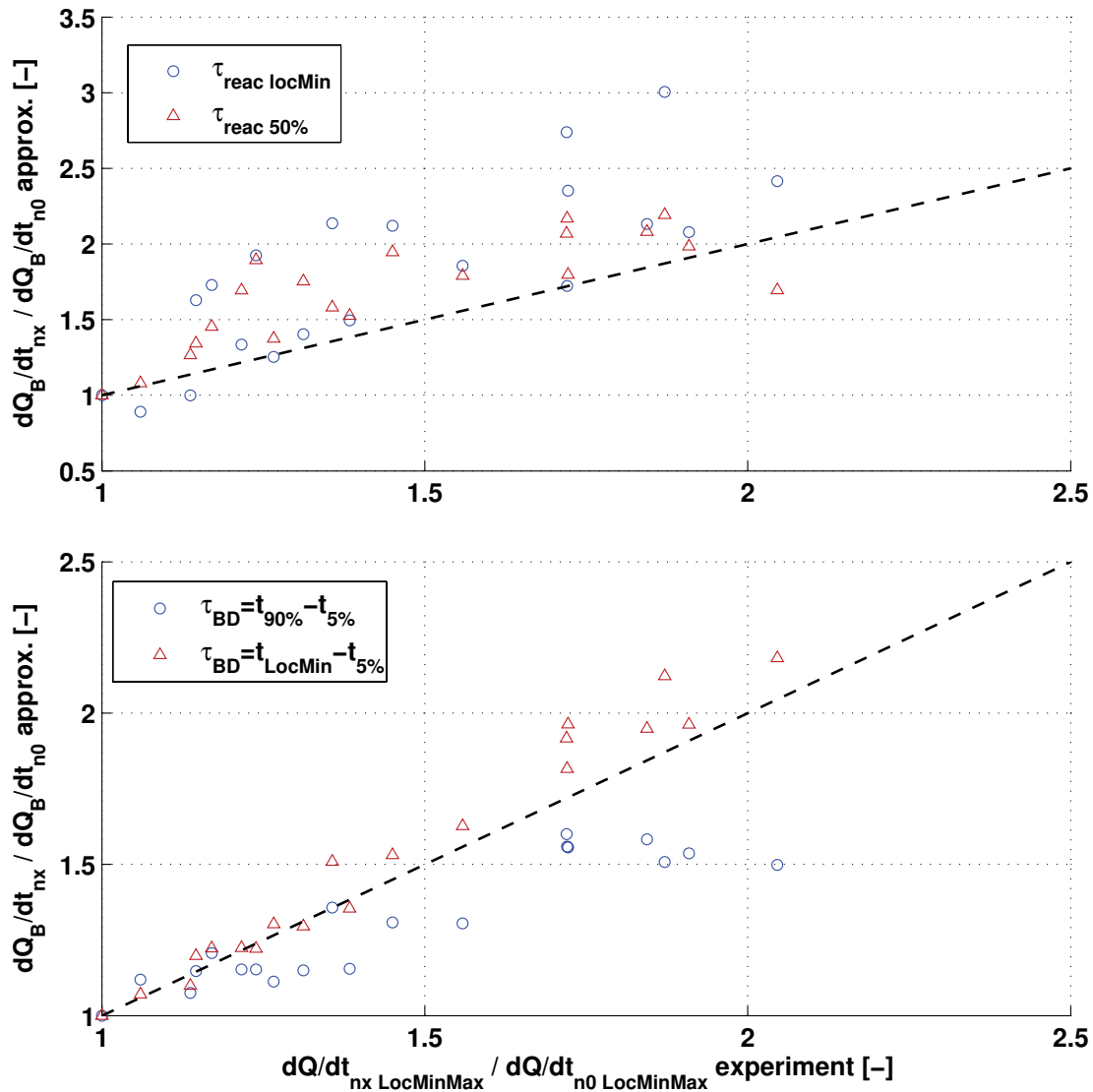
Figure 4.23: *Knock intensity estimation for two types of combustion approximations, a) combustion in a homogenous reactor and b) combustion due to flame propagation*

For the combustion in a homogenous reactor a temperature and pressure at a certain crank angle have been utilised. In the first approximation the temperature of the unburned mixture and the pressure at local minimum have been used - denoted by $\tau_{reaclocMin}$ - where for $\tau_{reac50\%}$ the corresponding values at the crank angle at 50% burned have been employed.

This approximation leads to higher „mean knock burn rates" than experimentally observed, resulting in values above the dashed line. The results

obtained with the values at the crank angle at 50% burned agree quite well. Several tests with mean temperature and pressure values did not improve the predictions.

Two different burn durations have been tested for the flame propagation assumption. On one hand the overall burn duration defined as $t_{90\%}$-$t_{5\%}$ and on the other hand the burn duration up to knock onset has been used. As it is indicated in figure 4.23 the knock intensity can be quite well approximated by the flame propagation assumption if the burn duration is defined as $\tau_{BD}=t_{LocMin}$-$t_{5\%}$. Furthermore, it can be seen that low burn durations lead to high knock intensities.

It can be concluded that knock intensity defined as $dQ/dt_{LocMinMax}$ can be quite well approximated by a flame propagation approach. The major disadvantage of the homogenous reactor assumption is that the values have to be defined at a certain crank angle which leads to an instantaneous reaction rate. Based on these observations the chemical kinetic combustion approximation can not be definitely excluded.

The results shown here may lead to the conclusion that at high engine speeds high „mean knock burn rates" can be observed (low burn durations on a time basis) which are necessary to cause high pressure oscillations. This could be an explanation for the various types of pressure curves seen at different engine speeds.

4.6   Knock Model Approach

The knock integral method was applied where the findings described in chapter 4.5 have been used. Several investigations show that the Arrhenius approach works well for methane and methane mixtures [58, 60, 85, 105] because no negative temperature coefficient behaviour is observed in contrast to most hydrocarbons used in engines. Inhelder [59] and Soltic [101] show, that it is quite difficult to approximate the ignition delay over the temperature range found in engines for n-heptane-air mixtures.

The instantaneous reaction rate is integrated from inlet valve close to start of knock, where knock does occur if

$$KI = \frac{1}{c_{iknock}} \cdot \int_{t_{IVC}}^{t_{LocMin}} \frac{dc_i}{dt} dt = \int_{t_{IVC}}^{t_{LocMin}} \frac{1}{\tau_{reac}} dt \qquad \geq 1 \qquad 4.18$$

The characteristic reaction time τ_{reac} is expressed by an Arrhenius function.

$$\tau_{reac} = A \cdot \left(\frac{p_{cyl}}{p_0}\right)^{-\alpha} \cdot e^{\left(\frac{TA}{T_U}\right)} \qquad 4.19$$

The cylinder pressure p_{cyl} has been normalised by a reference pressure p_0 here. A is a multiplier, α is a pressure exponent, TA is the activation temperature and T_U is the temperature of the unburned mixture.

In this work, the standard knock integral method approach was extended by the combustion progress variable x_B, based on the observations made in chapter 4.5.3, where the critical combustion progress was set to x_{Bcrit}=0.75 corresponding to about 1mm boundary layer thickness.

$$KI = \int_{t_{IVC}}^{t_{LocMin}} \frac{1}{\tau_{ID}} dt = \int_{t_{IVC}}^{t_{LocMin}} (x_{Bcrit} - x_B)^\beta \cdot \frac{1}{A} \cdot \left(\frac{p_{cyl}}{p_0}\right)^\alpha \cdot e^{-\frac{TA}{T_U}} \cdot dt \qquad 4.20$$

The extension (x_{Bcrit}-x_B) can be interpreted as the probability that knock can occur, because it indicates the available remaining „energy" in the unburned mixture.

For all engine parameters used in equation 4.20 - meaning the combustion progress x_B, the cylinder pressure p_{cyl} and the temperature of the unburned mixture T_U - the mean cycles at start of knock have been applied. Each of these mean cycles is representative for one operating point and has been assumed to include all the information needed. If the knock integral indicates knocking operation based on the mean cycle, it is known from the statistics that the operating point does knock. The integration starts at inlet valve close and ends with the crank angle of knock occurrence, which was calculated by the average of the crank angles at start of knock (local minimum) of all individual knocking cycles. This means, that the cycles have to exceed $dQ/d\varphi_{LocMinMax}$=1.5 %/°CA to be detected as knocking.

The bio-inspired algorithm - described in section 2.3.3 - was applied to identify the parameters A, α, β and TA. For each gas composition 20 operating points are available, where ten of them have been used for the identification process and all of them to verify the parameters found. The mean cycles for the spark timings at start of knock have been used to solve the knock criterion indicating the start of knock.

$$KI_{t_{knock}} = 1 \qquad\qquad 4.21$$

The resulting crank angles of knock occurrence for the ten selected operating points used for the parameter identification have been compared with the experimentally determined crank angles of knock onset and the square of the deviation of experimentally determined and computed crank angles of knock occurrence was minimised.

Several possible solutions have been found for every gas composition. These results can be interpreted as a sensitivity analysis of the bio-inspired algorithm. Figure 4.24 shows the results obtained for the parameters of the knock integral. The gas composition used was G20.

It can be seen from figure 4.23 that a linear correlation was found for the pressure exponent α as a function of the activation temperature TA meaning that the time dependent knock integral is getting „steep" with increasing parameters α and TA. The parameter A in contrast decreases for increasing TA. The axis on the right is plotted in a logarithmic scale and it was found that A „compensates" the exponential

temperature behaviour. The influence of the combustion progress is more difficult to interpret. It seems that it slightly increases with increasing activation temperature, where a balance between the parameters has to be achieved. The parameter range was set from β=0 to β=3 and therefore, the algorithm was allowed to choose β=0. For all gas compositions used in this work the algorithm chose β>0. It seems that the extension of the standard knock integral approach with a combustion progress variable is meaningful.
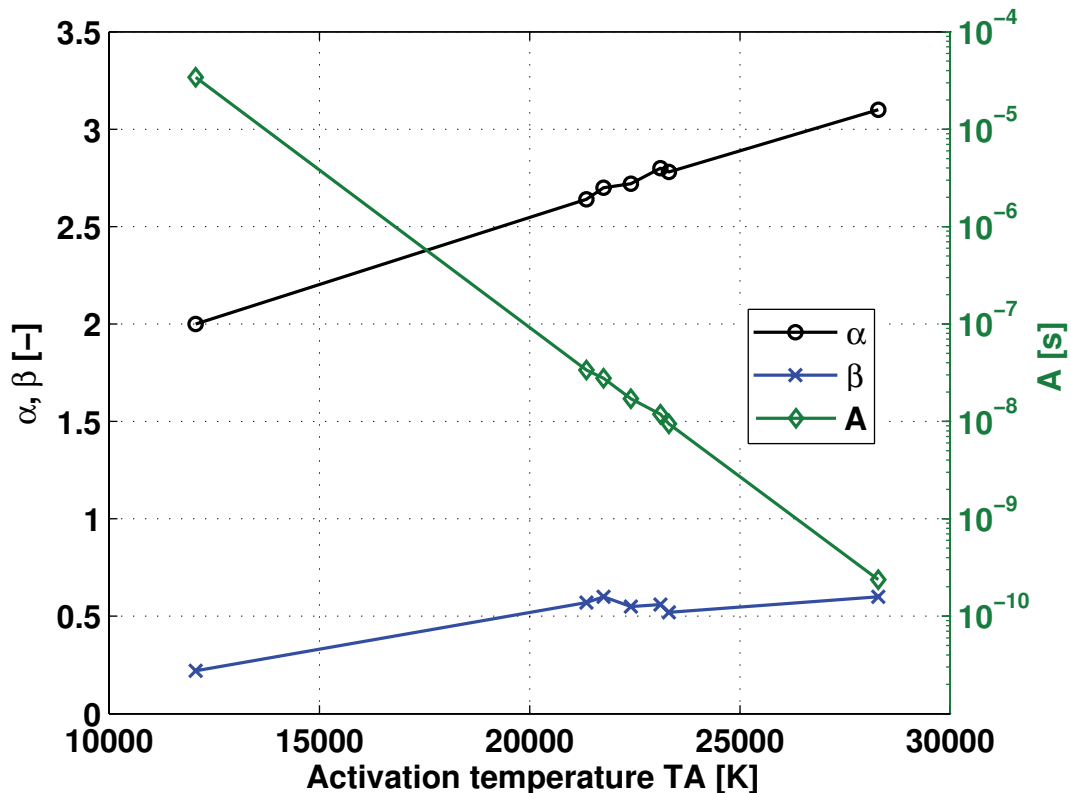
Figure 4.24: Parameter setups found for G20 by the bio-inspired algorithm for the ten operating points used for the identification process

All the parameter combinations displayed in figure 4.24 have led to reasonable results. The following figure shows the results for the computed crank angles of knock occurrence as a function of the experimentally determined crank angles of knock occurrence for low TA=12060K and high TA=23110K. These two activation temperatures will be used as denotation for the next few figures. Together with figure 4.24 the parameter setup can be clearly identified.

TA=12060K   TA=23110K
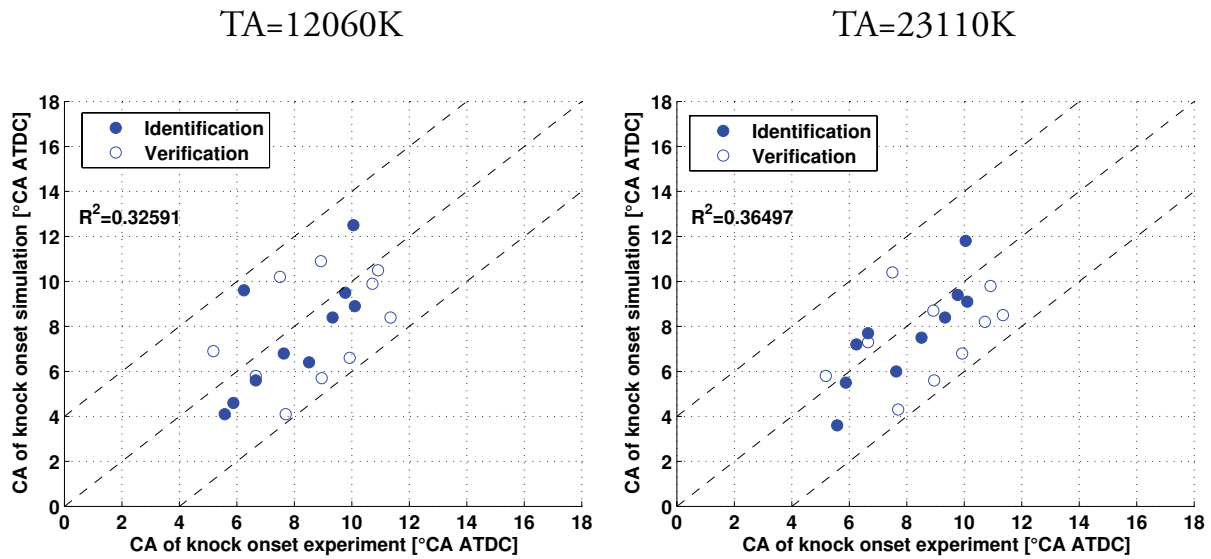
*Figure 4.25: Optimisation of model parameters for predicting the crank angle
of knock occurrence and comparison of the results obtained for
two different parameter setups*

The results displayed in figure 4.25 will be discussed in detail later. For the
moment, it can be noticed that both parameter setups lead to reasonable results,
meaning that all computed crank angles of knock occurrence are within a range of
±4° crank angles compared to the experimentally determined ones.

Therefore, two more criterions have been introduced to clarify which
parameter setup should be chosen. First, the knock integral must be able to
distinguish between non-knocking and knocking combustion and second, the
prediction of the crank angle of knock occurrence for a spark timing variation for one
operating point should be as good as possible. The first condition is very hard to
fulfil, but it is very important for the quality of the knock prediction capability.

The following figure compares the time dependent knock integral for two
parameter setups. The knock integral was applied to one operating point and
different spark timings, where for both parameter setups the same conditions have
been used. The non-knocking and knocking cycles are distinguished by the line
colour. The red lines indicate knocking combustion, the blue lines non-knocking
combustion.
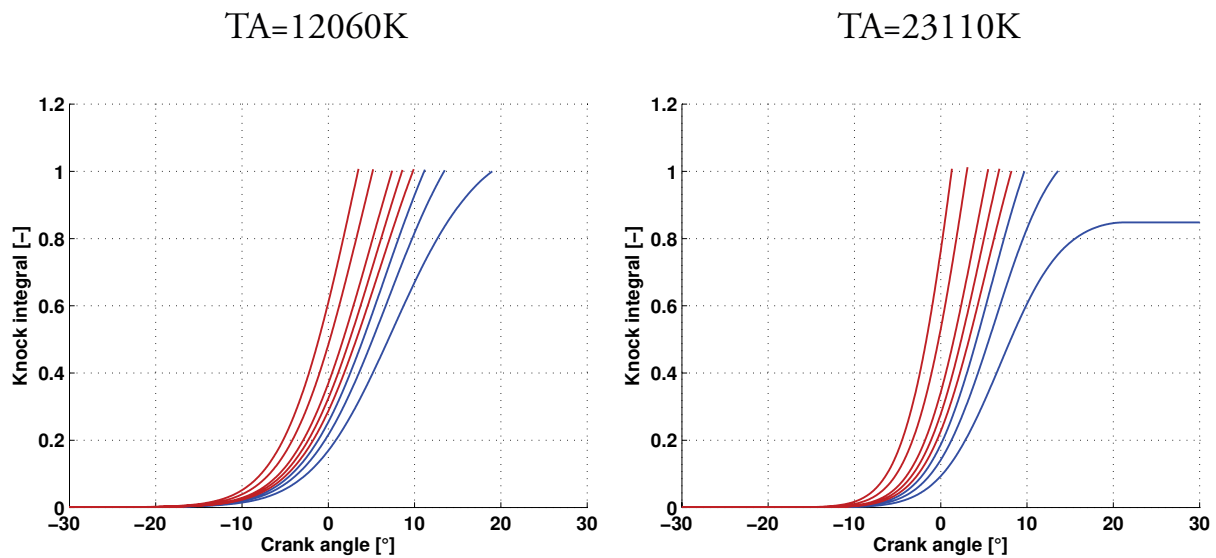
Figure 4.26: *Knock integral as a function of the crank angle for two parameter setups, operating point: G20, p_{intake}=1.4bar, T_{intake}=40°C, n=3000rpm, red: knocking conditions, blue: non-knocking conditions*

It can be seen that one non-knocking cycle was detected as non-knocking for the high activation temperature case, because the critical combustion progress is achieved and therefore, the knock integral remains constant. On the other hand all knock integrals achieve the critical value for TA=12060K.

By analysing the time derivative of the knock integral - which can be interpreted as the instantaneous reaction rate - it was observed, that this behaviour results from the decreasing temperature and pressure in the combustion chamber near top dead centre, where as a result the instantaneous reaction rate decreases. A high activation temperature leads to an intensified change in reaction rate. The instantaneous reaction rate will be analysed later.

Figure 4.26 further shows that the knock integral increases at the time, when combustion starts. Moreover, the curves are quite steep for both activation temperatures.

The second criterion was tested by computing the crank angles of knock occurrence for the same operating point and again all spark timings. The differences

between experimentally determined and computed crank angles of knock onset are displayed in figure 4.27.
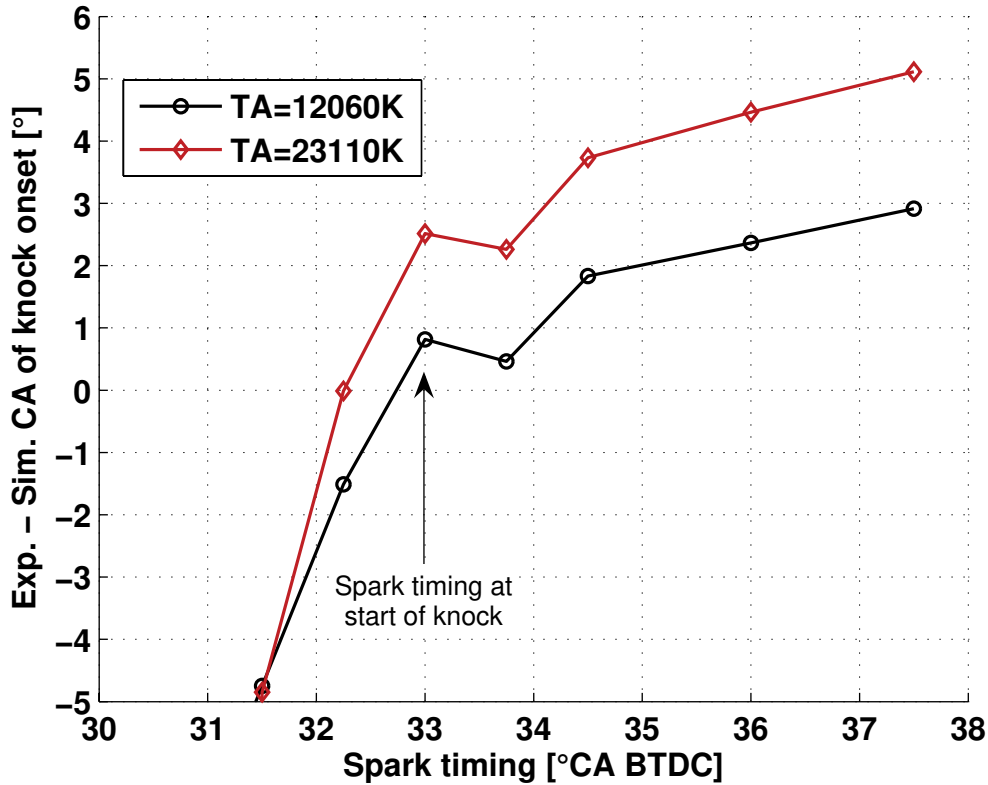
Figure 4.27: Comparison of experimentally determined and simulated crank angles of knock occurrence for a variation of spark timing, G20, p_{intake}=1.4bar, T_{intake}=40°C, n=3000rpm

The differences increase for high activation temperatures, where good results have been obtained for the low TA case over the entire range of spark timings. Due to the increased change of the reaction rate and the resulting steep knock integral curve the differences increase for TA=23110K. The spark timing at start of knock is marked by the arrow and it can be seen, that the non-knocking operating points for ST=31.5° CA and ST=32.25° CA do have a crank angle of knock occurrence. It has to be taken into account that the differentiation between non-knocking and knocking combustion was defined by a statistical analysis and therefore, some individual cycles can knock even though the operating point does not knock by definition.

The results obtained so far did not clearly exclude one parameter setup. Therefore, the instantaneous reaction rate, the time derivative of the knock integral, was additionally examined. Figure 4.28 shows the reaction rate for one operating

point and all spark timings. Again, the blue lines denote non-knocking, the red lines denote knocking combustion.
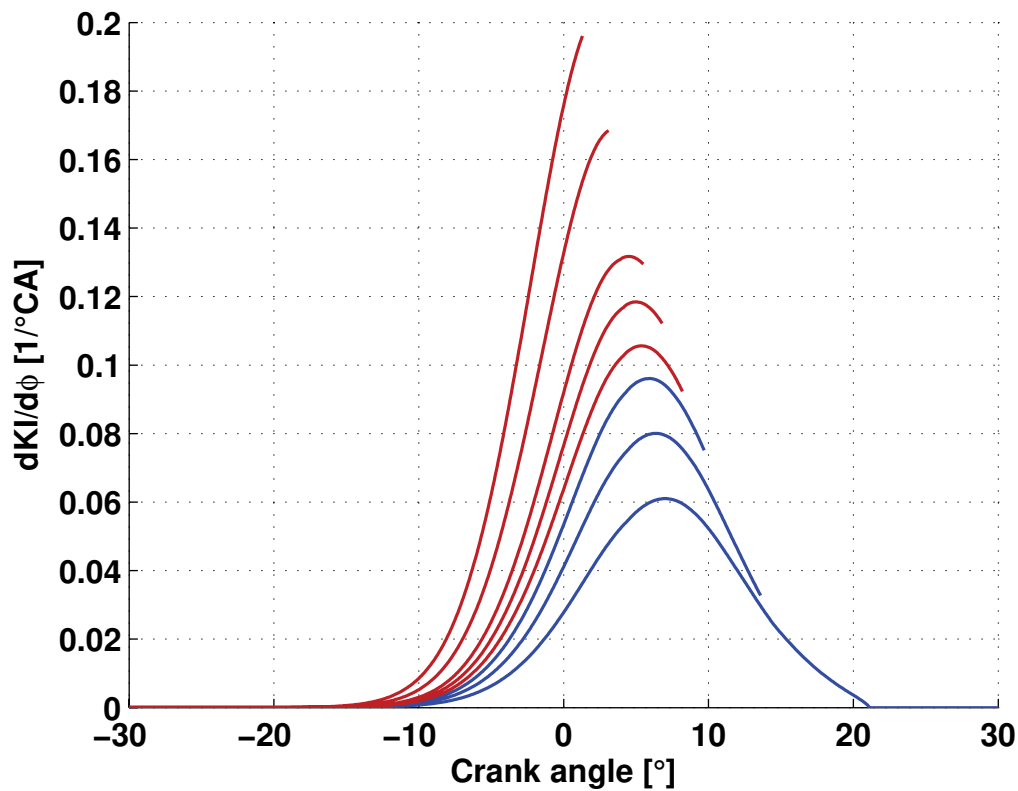
Figure 4.28: First derivative of the knock integral KI, G20, p_{intake}=1.4bar, T_{intake}=40°C, n=3000rpm, TA=23110K, red: knocking conditions, blue: non-knocking conditions

As mentioned before, the reaction rates increase first and decrease later due to the decreasing temperatures and pressures in the combustion chamber. Moreover, the maximum values occur after top dead centre and increase with increasing spark timing. In some cases, the crank angle of knock onset occurs after the maximum reaction rate is achieved.

Here, the maximum values of the first derivative of the knock integral are separated for the non-knocking and knocking operating points. Thus, the maximum values of the reaction rates have been investigated for all operating conditions and are displayed in the following figure.

If the knock integral remains below the critical value ($KI_{crit}=1$) - meaning that non-knocking combustion is indicated -, the maximum reaction rate was set to zero to provide a separation between non-knocking and knocking operating conditions.

TA=12060K   TA=23110K
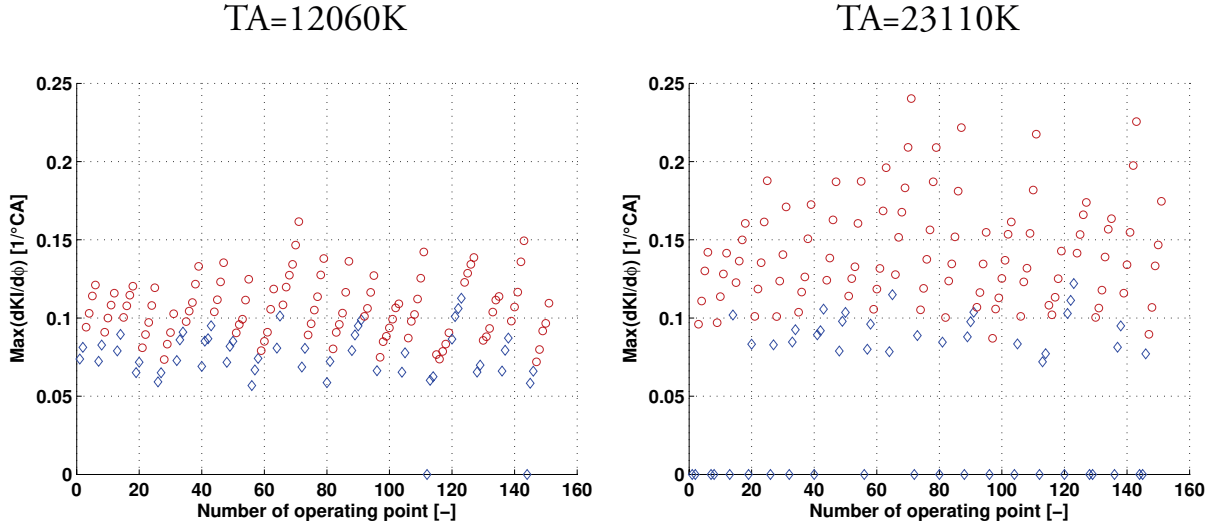
Figure 4.29: Maximum values of the knock integral derivative for all operating points for G20, red: knocking operating conditions, blue: non-knocking operating conditions according to the 95% quantile analysis

Figure 4.29 indicates that a separation line can be drawn, leading to a correct detection as non-knocking or knocking for most operating conditions. Moreover, it can be seen, that it will be difficult to correctly detect some single operating conditions as non-knocking.

The threshold value for the maximum reaction rate has been investigated by a sensitivity analysis. Two quality indices allow a quick and easy evaluation of the threshold values. This investigation was done for all the available measurements for each gas composition.

The quality indices for non-knocking QI_{nok} and for knocking combustion QI_{k} can be defined as

$$QI_{nok} = \frac{detected\ nonknocking\ cycles}{total\ nonknocking\ cycles} \cdot 100 \quad [\%] \qquad 4.22$$

$$QI_{k} = \frac{detected\ knocking\ cycles}{total\ knocking\ cycles} \cdot 100 \quad [\%] \qquad 4.23$$

The following diagram shows the resulting quality indices as a function of the threshold value for the maximum reaction rate for both activation temperatures.
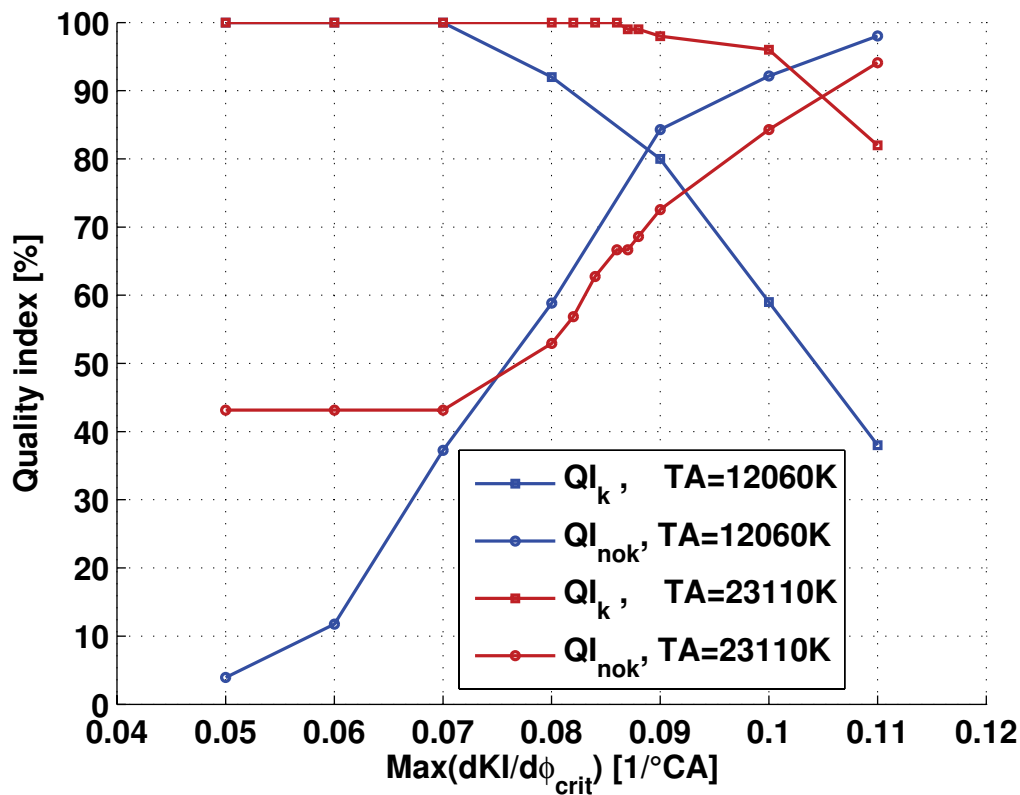
Figure 4.30: Quality indices of the knock prediction model as a function of the critical maximum reaction rate for two different activation temperatures and gas composition G20

If the low activation temperature is used, only about 4% of the non-knocking cycles are correctly detected if the threshold value is set to 0.05 1/°CA. This behaviour has already been observed earlier. In contrary, all of the knocking cycles are detected as knocking. If the threshold value increases, the quality index Q_{nok} increases continuously, whereas Q_k starts to decrease if the threshold value exceeds 0.07 1/°CA. The two lines cross around Max(dKI/dϕ)$_{Crit}$=0.89 1/°CA and both quality indices achieve about 81% at this time. If the threshold value further increases, it can be seen, that lots of knocking cycles are not correctly detected, whereby the quality for the non-knocking cycles still increases.

For TA=23110K the quality index for non-knocking cycles starts at about 42%, which is the result of the knock integrals remaining below the critical value. For threshold values below 0.086 1/°CA all of the knocking cycles and about 65% of the

non-knocking operating points are detected correctly. The same general trends can be observed for both activation temperatures, but for TA=23110K the curves cross at about Max(dKI/dϕ)$_{Crit}$=0.105 1/°CA and both quality indices achieve almost 90%.

These investigations clearly show that the parameter setup with high activation temperature leads to better results and was used as final formulation, although a high pressure exponent α has to be chosen. The critical maximum value of the reaction rate was set to 0.086 1/°CA to ensure the detection of all knocking operating conditions as knocking which is a conservative but a safe parameterisation. The quality indices for the other gas compositions can be found in appendix A.4.

4.6.1 Results for Different Gas Compositions

The bio-inspired algorithm has been applied to all gas compositions and five parameter sets have been found. The critical combustion progress variable x_{Bcrit}=0.75 and the pressure exponent α=2.8 have been fixed for all gas compositions, where the parameters A, TA and β were set free and had to be identified by the bio-inspired algorithm.

Figure 4.31 shows the results obtained at the spark timings at start of knock. The computed crank angles of knock occurrence are compared with the experimentally determined ones. The three dashed lines indicate an arbitrary range, meaning that the crank angles are within about 3% accuracy. The integration range is about 120° crank angle. The computed crank angles of knock onset occur too early if the markers are below the bisecting line. Furthermore, r-square is shown in the plots. It was observed, that r-square varies quite a lot, what may be a consequence of the low number of operating points at start of knock. The filled dots denote the operating points used for the identification procedure, the unfilled dots are the ten remaining operating points used for the verification. Several different combinations for the operating points used for the identification process have been tested, but no differences were found.

If pure methane (G20) is used all operating points are within 3.5° crank angle and some differences between identification and verification can be observed. The crank angles of knock occurrence are within six degrees and the overall trend can be reproduced well.

G20

G4E

G8E

G44

G25
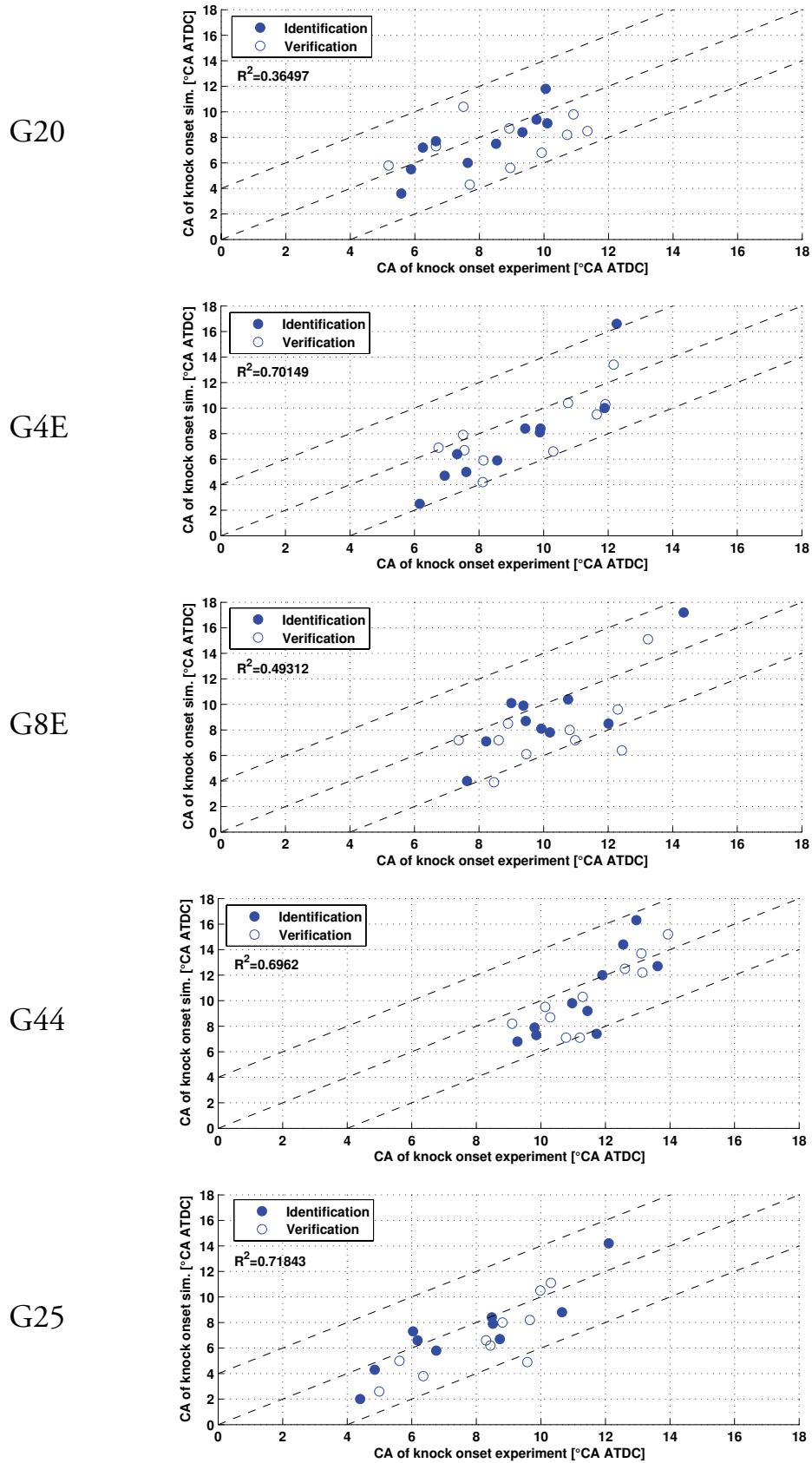
Figure 4.31: Final results for the predicted crank angle of knock occurrence

If G4E is used, the predictions are within 4° crank angle for the operating points investigated. Most of the computed crank angles are slightly too early and again, the overall trend can be reproduced well. The range is within 6° and the correlation coefficient r-square was observed to be quite high.

By analysing the results for G8E it is noticeable, that about half of the crank angles of knock occurrence are between 9° and 11° crank angle after top dead centre what makes it quite difficult for the algorithm to find the best solution. Nevertheless, the results obtained are meaningful. A quite late knock onset can be observed for two operating points. The trends can be predicted well.

The crank angles of knock onset occur later, if G44 is used as fuel. The computed values are within an acceptable difference where it can be seen, that two operating points are out of the arbitrary limits. The range is about 5° crank angle and the trends can be reproduced well.

Good agreements between experiments and predictions can be observed for G25 except for one operating point. The range for the crank angles of knock occurrence is increased compared to the other gas compositions and again the trend can be predicted well. No significant difference between identification and verification can be observed.

As a summary it can be noticed that the experiments and predictions agree quite well for all gas compositions tested. Some single operating points are out of the arbitrary boundaries. It has to be reminded that knock is a stochastic phenomena and the knock integral approach is rather simple and can not consider local effects.

Table 4.2 summarises the parameters found for the five synthetic gas compositions.

Para-meter	Unit	G20	G4E	G8E	G44	G25
A	s	$1.18084 \cdot 10^{-8}$	$2.66993 \cdot 10^{-8}$	$4.25495 \cdot 10^{-8}$	$9.28303 \cdot 10^{-8}$	$1.9368 \cdot 10^{-8}$
α	-	2.8	2.8	2.8	2.8	2.8
TA	K	23110	22250	21740	20590	22990
β	-	0.56	0.41	0.25	0.21	0.33
x_{Bcrit}	-	0.75	0.75	0.75	0.75	0.75

Table 4.2:   Parameter setups found for the gas compositions used

As expected, the activation temperature decreases if the ethane and propane content increases due to the different chemical properties of the higher hydrocarbons. The activation temperature of G25 compared to G20 is within the accuracy of the solution found by the bio-inspired algorithm. It has to be taken into account, that the G25 gas composition contains 86% methane and 14% nitrogen and therefore, only the concentration of methane changes but not the properties compared to G20 (100% methane).

Furthermore, it was observed that a correlation between the pre-coefficient $(x_{Bcrit} - x_B)^{\beta} \cdot 1/A$ and the fuel concentration exists. It should be mentioned that the pressure dependence is also part of the concentration but the pressure exponent α has been fixed for all gas compositions. Figure 4.32 displays the pre-coefficient as a function of the fuel concentration at inlet valve close multiplied by the volume at inlet valve close (x_B=0 at inlet valve close).

The experimentally determined fuel concentrations have been calculated based on the measured fuel mass flow where for G25 only the methane content has been considered. Figure 4.32 shows that the higher the concentration is the higher the pre-coefficient is. This means that the pre-coefficient does consider the influence of the fuel concentration on the reaction rate for the different gas compositions. The dependence of the fuel concentration on the operating point observed in figure 4.32 is not considered by the pre-coefficient but taken into account by the combustion

progress, the pressure, the temperature and the time dependence in the knock integral approach.
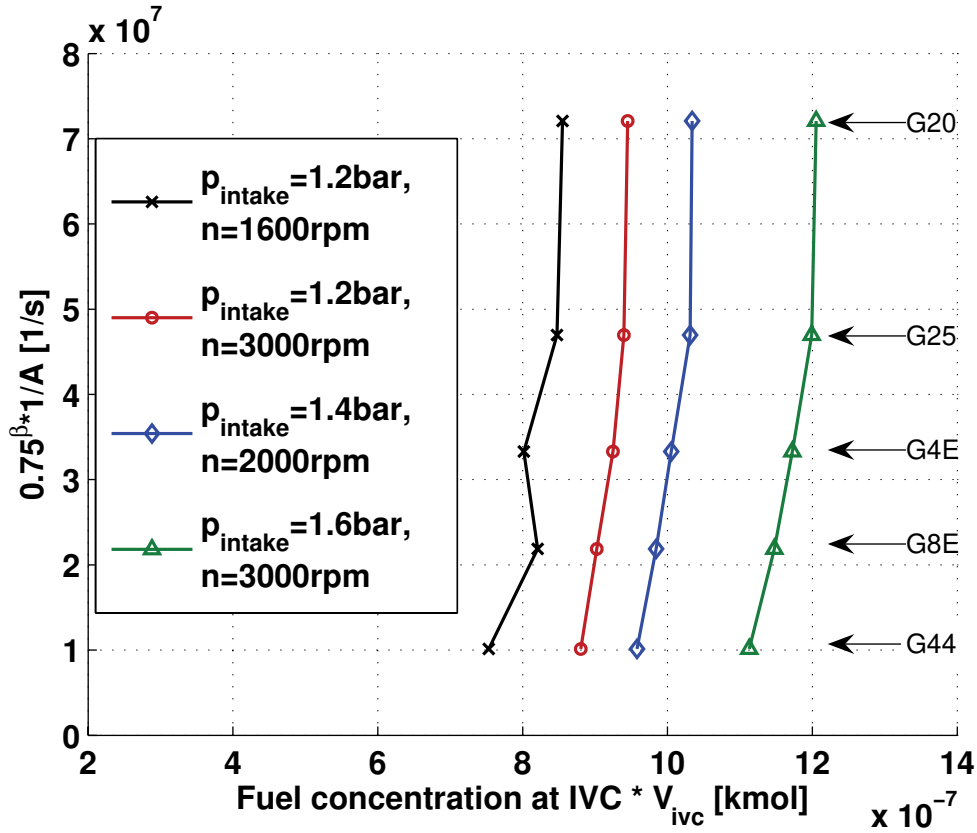
Figure 4.32: Pre-coefficient of the knock integral as a function of the fuel concentration at inlet valve close for four operating points

Based on the results listed in table 4.2 the parameters of the knock integral can be expressed as a function of the volume fraction of the individual components f_{xi}, where $(A, TA, \beta) = \sum X_i \cdot f_{xi}$. Table 4.3 summarises the coefficients X_i.

Parameter	Unit	f_{CH_4}	$f_{C_2H_6}$	$f_{C_3H_8}$	f_{N_2}
A	s	$1.18084 \cdot 10^{-8}$	$3.9607 \cdot 10^{-7}$	$1.65309 \cdot 10^{-6}$	$6.5806 \cdot 10^{-8}$
TA	K	23110	5985	-22765	22253
β	--	0.56	-3.315	-4.315	-1.083

Table 4.3: Parameter estimation for the knock integral as a function of the gas components

These functions allow estimating the activation temperature TA, the collision factor A and the influence of the combustion progress expressed by the parameter β for various compositions of compressed natural gas.

Finally, figure 4.33 visualises the different knock behaviour for the five gas compositions where for all gases the same pressure, temperature and burn rate curve was used to show the influence of the final parameters listed in table 4.2 exclusively.
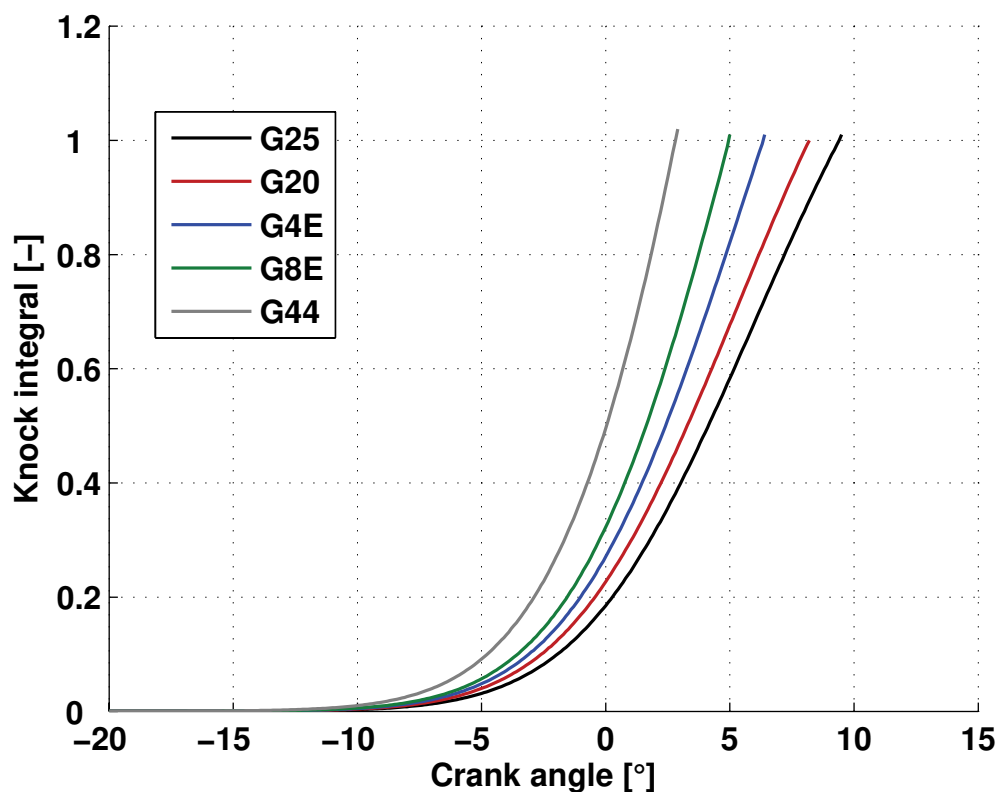
Figure 4.33: Comparison of the knock integral for five gas compositions for the same pressure, temperature and burn rate curve

As expected, the latest crank angle of knock onset can be found for the gas containing dilute gases (G25). Knocking combustion starts earlier if the amount of higher hydrocarbons increases in the gas composition. Furthermore, it can be observed that the pre-reactions, the reactions before combustion starts, are very low for all gases as already seen in figure 4.26.

4.7 Knock Intensity Estimation

Based on the flame propagation hypotheses set up in chapter 4.5.4 the knock intensity can be estimated. Equation 4.17 was extended by a factor K which can be defined by a characteristic curve describing the relationship between the mean burn rate based on the experimentally determined burn duration and the experimentally determined „mean knock burn rate".

$$\overline{\frac{dQ_B}{dt}} = K \cdot \frac{1}{\tau_{BD}} \qquad\qquad 4.24$$

The characteristic curve is shown in figure 4.34 for all operating points at start of knock for G20.
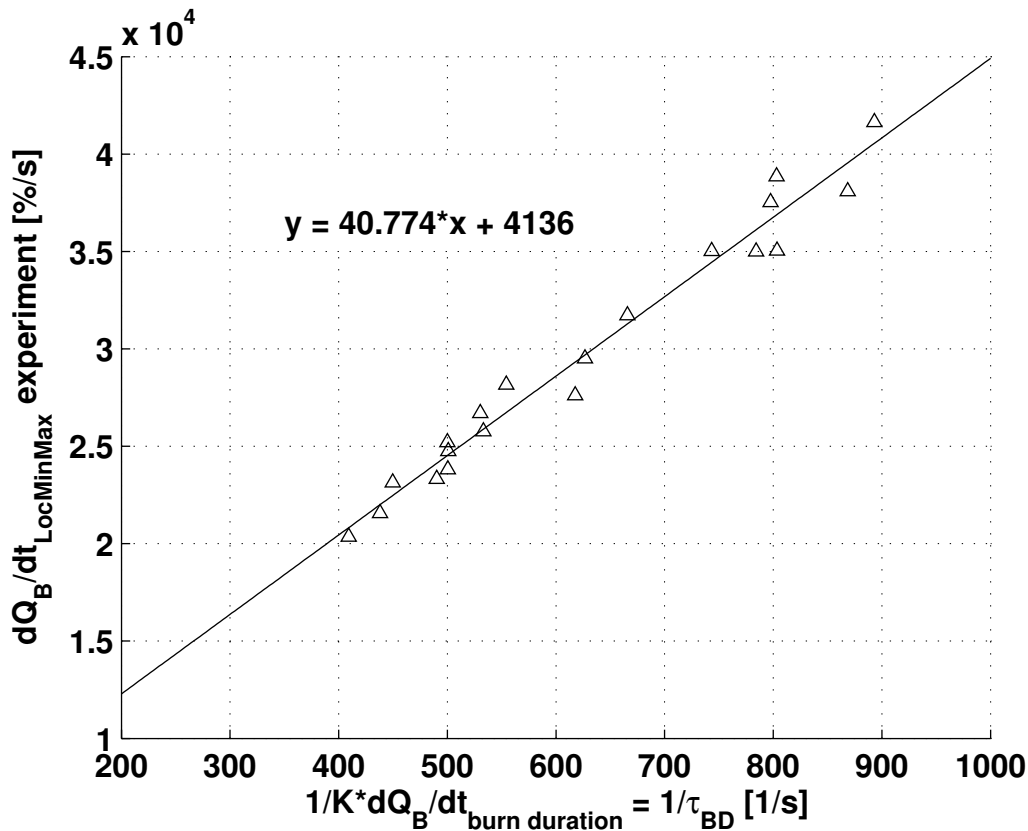
Figure 4.34: Relationship between knock intensity and mean burn rate based on the experimentally determined burn duration for all operating points at start of knock, G20

A linear behaviour can be observed between the estimations and the experimentally determined knock intensities. This characteristic curve was defined

for all gas compositions used in this work (see appendix A.5 for the other gas compositions).

The knock intensity estimation was applied to the operating points at start of knock for G20. The knock integral was computed and the burn duration was defined as the difference of the computed crank angle of knock occurrence and the crank angle at 5% burned.

The results obtained show quite well knock intensity estimations. These estimations can be used additionally to the basic knock integral approach to have an approximation of the expected knock intensities.
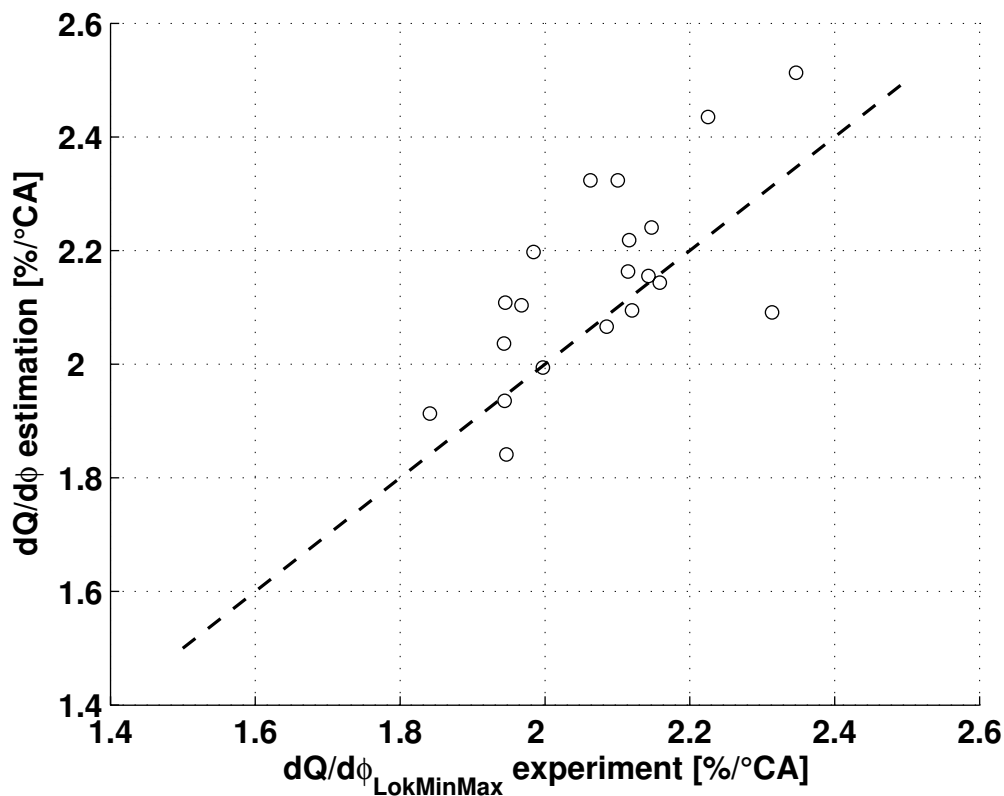
Figure 4.35: Estimated and experimentally determined knock intensity at start of knock for G20

The reason for the deviations is, that the simulated crank angles of knock occurrence have been used to define the burn duration. Therefore, some differences can be found in estimated and experimentally determined burn duration.

Chapter 5

Summary and Conclusions

A typical optimisation task in the engine development process with concern to new IC engine concepts was presented in the beginning of this work. The complexity and requirements will further increase in the future. Experimental work combined with computations will significantly accelerate the development process and support the understanding of the results obtained. Simulations therefore should not be interpreted as a competing but as a complementary process to measurements and are necessary to reduce costs and time to market. Moreover, increasing computational power leads to further reduced time demands.

A key parameter is the capability to predict fuel consumption. The validation of different driving strategies, aiming at increasing the engine efficiency, has to be carried out, where the strategies are often limited by the knock phenomena occurring at fuel load operating conditions. These contradictory requirements clearly indicate the necessity of accurate physical formulations of the combustion and knock behaviour.

The aim of this work was to develop an empirical and a phenomenological combustion model dedicated to compressed natural gas engines. The main focus was held on the knock model approach, whereas a systematic investigation of the effect of chemical compositions found in compressed natural gas was carried out.

First, an empirical combustion model was used to predict fuel consumption for different engine driving strategies. The comparison between experimental data and predictions lead to the conclusion, that global qualitative trends can be predicted quite well. If this model is applied to different combustion chamber geometries, the limitations can be clearly observed. Some of the conversion functions should be redefined or a conversion function for different combustion chamber geometries may be introduced, if not only trends but absolute values play a decisive role.

The phenomenological model in contrast does consider to some degree physical, chemical and geometrical effects during combustion. This model has therefore the potential to be useful in understanding and predicting fluid mechanical phenomena for extended deviations from measured operating conditions. It however also needs some calibration through experiments as it was shown by comparing two different combustion chamber designs. Moreover, the phenomenological model allowed clarifying how the piston geometry affects the flame propagation. Finally, the model was tested for gasoline applications and it was found, that meaningful results have been obtained.

Based on these observations it can be noticed, that phenomenological models should be preferred for future developments. No differences in computing time have been observed, what may be a consequence of the complexity of the entire engine model. This indicates that the combustion model formulation is not the limiting factor, if cycle simulation tools are used.

It was shown, that compressed natural gas engines burn slower than gasoline engines. High turbulence intensities are important for CNG engines to further increase the efficiency and to allow high EGR rates. For part load operation, the EGR should not be cooled whereon the temperature will increase in the combustion chamber leading to slightly higher flame speeds compared to cooled EGR. On the other hand, the potential to reduce NOx-emissions can not be fully utilised in this case.

The 3-Dimensional calculations revealed interesting local effects of flame propagation in support of the phenomenological model. Although not free of model parameters adjustment, this class of tools can be used nowadays efficiently to interpret and understand in-depth experimental findings and partially to predict changes of parameters, which are out of reach for the empirical and phenomenological combustion model.

Some more engines should be tested to gain more information about the flame front area function for various combustion chamber designs and to improve the capability in predicting the combustion behaviour.

At high load operation, part of the unburned mixture can self-ignite leading to knocking combustion. A simple knock model based on the knock integral approach has been developed for different gas compositions. One of the key parameters was found to be the differentiation between non-knocking and knocking combustion. The widely-used analysis of the maximum amplitudes of the pressure oscillations has

been replaced by the analysis of the burn rate, where a new knock detection method has been developed. A clearly defined initiation of knocking combustion could then be observed without ambiguity.

The standard knock integral approach was extended with the combustion progress leading to a correct detection of non-knocking cycles in most cases. The activation temperature decreases if the compressed natural gas contains higher hydrocarbons leading to higher risk of knock occurrence. The spark timing has to be retarded by about two degrees if 4% ethane and about four degrees if 4% propane is added whereas earlier spark timings can be employed if the compressed natural gas contains nitrogen.

The knock intensity can be accurately described by the burn duration up to the crank angle of knock occurrence, meaning that knock intensity can be approximated by a flame propagation assumption. The „homogenous reactor hypotheses" could not definitely be excluded.

Quite good agreements between experimentally determined and predicted crank angle of knock occurrence have been observed. Most of the predictions are within 3% deviation. It has to be taken into account, that knock is a highly statistical phenomenon and was approximated by a simple approach based on the mean cycles. Therefore, the results obtained are quite satisfying.

The detection of non-knocking cycles as non-knocking has been improved by using high activation temperatures for the knock integral on one hand and on the other hand by introducing a threshold value for the instantaneous reaction rate. Finally, a conservative parameter setup was used so that all knocking operating points are detected correctly.

The knock model should be applied to different engines and some more gas compositions should be tested to examine the limitations of the developed approach. Furthermore, the capability of EGR to reduce knock intensity could be investigated.

The new knock detection method is appropriate for CNG and gasoline engines to support the adaptation of knock systems on engine test benches, where non-knocking and knocking combustion can be distinguished at low engine speeds.

Chapter 6

References

[1]   Monitoring of ACEA's Commitment of CO2 Emission Reductions from Passenger Cars, Final Report, September 2003

[2]   Communication from the commission   (...) on alternative fuels for road transportation and on a set of measures to promote the use of biofuels, COM(2001) 547 final, 2001

[3]   **Abdel-Gayed, R., Bradley, D.:** *Dependence of Turbulent Burning Velocity on Turbulent Reynolds Number and Ratio of Laminar Burning Velocity to R.M.S. Turbulent Velocity*, Sixteenth Symposium (International) on Combustion, The Combustion Institute, p. 1725-1735, 1976

[4]   **Achuth, M., Mehta, P. S.:** *Predictions of tumble and turbulence in four-valve pentroof spark ignition engines*, International Journal of Engine Reseach, Volume 2, Number 3, p. 209-226, 2001

[5]   **Adolph, N.:** *Messung des Klopfens an Ottomotoren*, Disseration RWTH Aachen, 1983

[6]   **Alt, N., Nehl, J., Weihagen, N., Steidten, T.**: *Methoden zur Klopfoptimierung im Motorenentwicklungsprozess*, 1. Tagung Klopfregelung im Ottomotor - Trends für Serienentwickler, 2003

[7]   **Ando, H., Takemura, J., Koujina, E.:** *A Knock Anticipating Strategy Basing on the Real-Time Combustion Mode Analysis*, SAE Paper 890882, 1989

[8]   **Auto-Schweiz:** *9. Berichterstattung im Rahmen der Energieverordnung über die Absenkung des spezifischen Treibstoff-Normverbrauchs von Personenwagen 2004*, 2005

[9]   **Bach, C., Laemmle, Ch., Bill, R., Soltic, P.:** *Clean Engine Vehicle - A Natural Gas Driven Euro-4/SULEV with 30% Reduced CO$_2$-Emissions*, SAE Paper 2004-01-0645, 2004

[10]   **Bargende, M.:** *Ein Gleichungsansatz zur Berechnung der instationären Wandwärmeverluste im Hochdruckteil von Ottomotoren*, Dissertation TH Darmstadt, 1991

[11]   **Bargende, M.:** *Schwerpunkt-Kriterium und automatische Klingelerkennung*, MTZ 56 (10), p. 632-638, 1995

[12]   **Beretta, G., Rashidi, M., Keck, J.:** *Turbulent Flame Propagation and Combustion in Spark Ignition Engines*, Combustion and Flame 52, p. 217-245, 1983

[13]   **Blizard, N., Keck, J.:** *Experimental and Theoretical Investigation of Turbulent Burning Model for Internal Combustion Engines*, SAE Paper 740191, 1974

[14]   **Bloss, W., Wodarz, J., Köhler, J.:** *Einfluss realer Motorbedingungen auf die Flammenkernbildung*, MTZ 63 (6), p. 300-308, 1993

[15]   **Boulouchos, K.:** *Motorische Verbrennungsverfahren und -systeme*, Lecture Notes, LAV, ETH Zurich, 2003

[16]   **Boulouchos, K., Eberle, M. K.:** *Aufgabenstellungen der Motorthermodynamik heute - Beispiele und Lösungsansätze*, MTZ 52 (11), p. 574-583, 1991

[17]   **Boulouchos, K., Zbiorczyk, A., Inhelder, J., Frouzakis, Ch.:** *Optimale Auslegung umweltfreundlicher Gasmotoren mit Hilfe von Simulationswerkzeugen*, MTZ 58 (9), p. 486-499, 1997

[18]   **Boulouchos, K., Steiner, T., Dimopoulos, P.:** *Investigation of Flame Speed Models for the Flame Growth Period During Premixed Engine Combustion*, SAE Paper 940476, 1994

[19]   **Boulouchos, K., Obrecht, P., Warth, M.:** *Kennfeldtaugliche Vorausberechnungen beim Dieselmotor*, MTZ 65 (11), p. 924-931, 2004

[20]   **Bradley, D., Kalghatgi, G. T., Golombok, M.:** *Fuel Blend and Mixture Strength Effects on Autoignition Heat Release Rates and Knock Intensity in S. I. Engines*, SAE Paper 962105, 1996

[21] **Bradley, D., Kalghatgi, G. T., Golombok, M., Yeo, J.:** *Heat Release Rates due to Autoignition, and their Relationship to Knock Intensity in Spark Ignition Engines*, Twenty-Sixth Symposium (International) on Combustion, The Combustion Institute, p. 2653-2660, 1996

[22] **Brecq, G., Bellettre, J., Tazerout, M.:** *A new indicator for knock detection in gas SI engines*, International Journal of Thermal Sciences 42, p. 523-532, 2003

[23] **Brecq, G., Bellettre, J., Tazerout, M., Muller, T.:** *Knock prevention of CHP engines by addition of N_2 and CO_2 to the natural gas fuel*, Applied Thermal Engineering 23, p. 1359-1371, 2003

[24] **Brohmer, A.:** *Berechnung des Brennverlaufs im Ottomotor unter Berücksichtigung von Einlassströmung und Brennraumgeometrie*, Dissertation RWTH Aachen, 1987

[25] **Burgdorf, K., Denbratt, I.:** *A Contribution to Knock Statistics*, SAE Paper 982475, 1998

[26] **Burkhardt, C., Bargende, M.:** *Applikationshilfen zur Volllastabstimmung von Ottomotoren*, 1. Tagung Klopfregelung für Ottomotoren - Trends für Serienentwickler, 2003

[27] **By, A., Kempinski, B., Rife, J. M.:** *Knock in Spark Ignition Engines*, SAE Paper 810147, 1981

[28] **Callahan, T. J., Ryan, Th. W., Buckingham, J. P., Kakaockzi, R. J., Sorge, G.:** *Engine knock rating of natural gases - expanding the methane number database*, Proceedings of the 18th Annual Fall Technical Conference of the ASME Internal Combustion Engine Division, ICE-Vol. 27-4, p. 59-64, 1996

[29] **CD-adapco:** *Star-CD Methodology*, Version 3.15A, 2002

[30] **Checkel, M. D., Dale, J. D.:** *Computerized Knock Detection from Engine Pressure Records*, SAE Paper 860028, 1986

[31] **Checkel, M. D., Dale, J. D.:** *Testing a Third Derivative Knock Indicator on a Production Engine*, SAE Paper 861216, 1986

[32] **Chun, K. M., Heywood, J. B.:** *Characterization of Knock in a Spark-Ignition Engine*, SAE Paper 890156, 1989

[33] **Cowart, J. S., Haghgooie, M., Newman, C. E., Davis, G. C., Pitz, W. J., Westbrook, C. K.:** *The Intensity of Knock in an Internal Combustion Engine: An Experimental and Modeling Study*, SAE Paper 922327, 1992

[34] **Csallner, P.:** *Eine Methode zur Vorausberechnung der Änderung des Brennverlaufes von Ottomotoren bei geänderten Betriebsbedingungen*, Dissertation TU München, 1981

[35] **Davis, G. C., Borgnakke, C.:** *The Effect of In-Cylinder Flow Processes (Swirl, Squish and Turbulence Intensity) on Engine Efficiency - Model Predictions*, SAE Paper 820045, 1982

[36] **Diana, S., Giglio, V., Iorio, B., Police, G.:** *Evaluation of the Effect of EGR on Engine Knock*, SAE Paper 982479, 1998

[37] **Dimitrov, D., Chmela, F., Wimmer, A.:** *Eine Methode zur Vorausberechnung des Klopfverhaltens von Gasmotoren*, 4. Dessauer Gasmotoren-Konferenz, p. 114-130, 2005

[38] **Douaud, A. M., Eyzat, P.**: *Four-Octane-Number Method for Predicting the Anti-Knock Behavior of Fuels and Engines*, SAE Paper 780080, 1978

[39] **Elia, M., Ulinski, M., Metghalchi, M.:** *Laminar Burning Velocity of Methane-Air-Diluent Mixtures*, Transactions of the ASME, Journal of Engineering for Gas Turbines and Power, Vol. 123, p. 190-196, 2001

[40] **Erdmann, H.-D., Königstedt, J., Fitzen, M.:** *Erster ULEV-Ottoturbomotor - der Audi 1.8-l-Fünfventil-Turbo mit 128kW*, MTZ 62 (2), 2001

[41] **Fischer, M., Günther, M., Röpke, K., Lindemann, M., Placzek, R.:** *Klopferkennung im Ottomotor*, MTZ 3, 2003

[42] **Fox, J., Cheng, W., Heywood, J.:** *Model for Prediction Residual Gas Fraction in Spark Ignition Engines*, SAE Paper 931025, 1993

[43] **Franzke, D. E.:** *Beitrag zur Ermittlung eines Klopfkriteriums der ottomotorischen Verbrennung und zur Vorausberechnung der Klopfgrenze*, Dissertation TU München, 1981

[44] **Fuchs, P.:** *Die Auswirkungen der Einblaszeit auf das Verhalten eines Erdgasmotors*, Semester Thesis, LAV ETH Zürich, 2002

[45] **Gamma Technologies:** *GT-Power - Users's Manual and Tutorial, GT-Suite Version 6.1*, 2004

[46] **Geiser, F., Wytrykus, F., Spicher, U.:** *Combustion Control with the Optical Fibre Fitted Production Spark Plug*, SAE Paper 980139, 1998

[47] **Grandin, B., Denbratt, I., Bood, J., Brackmann, C., Bengtsson, P-E.:** *A study of the influence of exhaust gas recirculation and stoichiometry on the heat release in the end-gas prior to knock using rotational coherent anti-Stokes-Raman spectroscopy thermoemtry*, International Journal of Engine Research, Volume 3, Number 2, p. 209-221, 2002

[48] **Grandin, B., Angström, H. E., Stalhammar, P., Olofsson, E.:** *Knock Suppression in a Turbocharged SI Engine by Using Cooled EGR*, SAE Paper 982476, 1998

[49] **Griffiths, J. F., MacNamara, J. P., Sheppard, C. G. W., Turton, D. A., Whitaker, B. J.:** *The relationship of knock during controlled autoignition to temperature inhomogeneities and fuel reactivity*, Fuel 81, p. 2219-2225, 2002

[50] **Griffiths, J. F., Nimmo, W.:** *Spontaneous Ignition and Engine Knock under Rapid Compression*, Combustion and Flame 60, p. 215-218, 1985

[51] **Gu, X., Haq, M., Lawes, M., Woolley, R.:** *Laminar Burning Velocity and Markstein Lengths of Methane-Air Mixtures*, Combustion and Flame 121, p. 41-58, 2000

[52] **Gülder, Ö. L.:** *Turbulent Premixed Flame Propagation Models for Different Combustion Regimes*, Twenty-Third Symposium (International) on Combustion, The Combustion Institute, p. 743-750, 1990

[53] **Halstead, M. P., Kirsch, L. J., Quinn, C. P.:** *The Autoignition of Hydrocarbon Fuels at High Temperatures and Pressures - Fitting of a Methematical Model*, Combustion and Flame 30, p. 45-60, 1977

[54] **Heywood, J. B.:** *Internal Combustion Engine Fundamentals*, McGraw-Hill International Editions, 1988

[55] **Hires, S., Tabaczynski, R., Novak, J.:** *The Prediction of Ignition Delay and Combustion Intervals for a Homogeneous Charge*, Spark Ignition Engine, SAE Paper 780232, 1978

[56] **Hudson, C., Gao, X., Stone, R.:** *Knock measurement for fuel evaluation in spark ignition engines*, Fuel 80, p. 395-407, 2001

[57] **Hunter, T., Wang, H., Litzinger, T., Frenklach, M.:** *The Oxidation of Methane at Elevated Pressures: Experiments and Modeling*, Combustion and Flame 97, p. 201-224, 1994

[58] **Hunter, T., Litzinger, T., Wang, H., Frenklach, M.:** *Ethane Oxidation at Elevated Pressures in the Intermediate Temperature Regime: Experiments and Modeling*, Combustion and Flame 104, p. 505-523, 1996

[59] **Inhelder, J.:** *Verbrauchs- und schadstoffoptimiertes Ottomotor-Aufladekonzept*, Dissertation Nr. 11948, ETH Zürich, 1996

[60] **Isogai, T., Furutani, M., Ohta, Y.:** *Ignition Characteristics Fluctuation of Fuel Gas and its Elimination for Natural Gas Engines*, 3. Dessauer Gasmotoren-Konferenz, 2003

[61] **Jenkin, R. J., James, E. H., Malalasekera, W.:** *Predicting the Onset of End-Gas Autoignition with a Quasi-Dimensional Spark Ignition Engine Model*, SAE Paper 972877, 1997

[62] **John, A., Kaminski, H., Kuhlbusch, T.:** *Entwicklung und Erprobung eines zweistufigen Impaktors zur Messung alveolengängiger Quarzfeinstaubemissionen und Durchführung von Validierungsmessungen*, Bericht des Instituts für Energie- und Umwelttechnik Bereich "Lufgetragene Partikel / Luftreinhaltung", Duisburg, 2004

[63] **Kaiser, T., Hoffmann, A.:** *Einfluss der Zündkerzen auf das Entflammungsverhalten in modernen Motoren*, MTZ 61 (10), p. 656-663, 2000

[64] **Karim, G. A., Gao, J.:** *A Predictive Model for Knock in Spark Ignition Engines*, SAE Paper 922366, 1992

[65] **Kleinschmidt, W.:** *Zur Simulation des Betriebes von Ottomotoren an der Klopfgrenze*, Fortschritt-Berichte VDI Reihe 12, Nr. 422, 2000

[66] **Koch, T.:** *Numerischer Beitrag zur Charakterisierung und Vorausberechnung der Gemischbildung und Verbrennung in einem direkteingespritzten, strahlgeführten Ottomotor*, Dissertation Nr. 14937, ETH Zürich, 2002

[67] **Kollmeier, H. P.:** *Untersuchungen über die Flammenausbreitung bei klopfender Verbrennung,* Dissertation RWTH Aachen, 1987

[68] **Kubesh, J., Brehob, D. D.:** *Analysis of Knock in a Dual-Fuel Engine*, SAE Paper 922367, 1992

[69] **Kubesh, J., King, R., Liss, W.:** *Effect of Gas Composition on Octane Number of Natural Gas Fuels*, SAE Paper 922359, 1992

[70] **Lämmle, Ch., Boulouchos, K., Bach, Ch.:** *Prediction and Interpretation of Combustion Processes in Natural Gas Engines - A comparative Overview of Simulation Methods for Practical Applications*, 4. Dessauer Gasmotoren-Konferenz, 2005

[71] **Li, H., Miller, D., Cernansky, N.:** *Development of a Reduced Chemical Kinetic Model for Prediction of Preignition Reactivity and Autoignition of Promary Reference Fuels*, SAE Paper 960498, 1996

[72] **Li, H., Miller, D., Cernansky, N.:** *A Study on the Application of a Reduced Chemical Reaction Model to Motored Engines for Heat Release Prediction*, SAE Paper 922328, 1992

[73] **Liao, S., Jiang, D., Cheng, Q.:** *Determination of laminar burning velocities for natural gas,* Fuel 83, p. 1247-1250, 2004

[74] **Lindemann, M., Funk, T.:** *Einfluss verschiedener Filterverfahren auf die Generierung druckbasierter Klopfmerkmale*, 1. Tagung Klopfregelung für Ottomotoren - Trends für Serienentwickler, 2003

[75] **Liu, J., Schorn, N., Schernus, Ch., Peng, L.:** *Comparison Studies on the Method of Characteristics and Finite Difference Methods for One-Dimensional Gas Flow through IC Engine Manifold*, SAE Paper 960078, 1996

[76] **Mastorakos, E., Wright, Y. M.:** *Simulations of Turbulent Spray Auto-ignition with Elliptic Conditional Moment Closure*, Proceedings of the European Combustion Meeting, 2003

[77] **Merker, G., Schwarz, Ch., Stiesch, G., Frank, O.:** *Verbrennungsmotoren - Simulation der Verbrennung und Schadstoffbildung*, 2., vollständig neubearbeitete und erweiterte Auflage, Teubner Verlag, 2004

[78] **Metghalchi, K., Keck, J.:** *Burning Velocities of Mixtures of Air with Methanol, Isooctane, and Indolene at High Pressure and Temperature*, Combustion and Flame 45, p. 191-210, 1982

[79] **Morel, T., Rackmil, C. I., Keribar, R., Jennings, M. J.:** *Model for Heat Transfer and Combustion in Spark Ignited Engines and Its Comparison with Experiments*, SAE Paper 880198, 1988

[80] **Morel, T., Keribar, R.:** *A Model for Predicting Spatially and Time Resolved Convective Heat Transger in Bowl-in-Piston Combustion Chambers*, SAE Paper 850204, 1985

[81] **Naber, J., Siebers, D., Westbrook, Ch., Caton, J., Di Julio, S.:** *Natural Gas Autoignition Under Diesel Conditions: Experiments and Chemical Kinetic Modelling*, SAE Paper 942034, 1994

[82] **Nellen, C., Boulouchos, K.:** *Aufgeladene Gasmotoren mit AGR und Dreiwege-Katalysator - der Weg zu niedrigsten Emissionen bei hohem Wirkungsgrad und grosser Leistungsdichte*, MTZ 61 (1), 2000

[83] **Nellen, C., Boulouchos, K.:** *Natural Gas Engines for Cogeneration: Highest Efficiency and Near-Zero-Emissions through Turbocharging, EGR and 3-Way Catalytic Converter*, SAE Paper 2000-01-2825, 2000

[84] **Obrecht, P.:** *WEG - Benutzerhandbuch und Programmdokumentation*, LAV, 2004

[85] **Petersen, E., Davidson, D., Hanson, R.:** *Kinetics Modeling of Shock-Induced Ignition in Low-Dilution CH4/O2 Mixtures at High Pressures and Intermediate Temperatures*, Combustion and Flame 117, p. 272-290, 1999

[86] **Pires Da Cruz, A., Dean, A. M., Grenda, J. M.:** *A Numerical Study of the Laminar Flame Speed of Stratified Methane/Air Flames*, Proceedings of the Combustion Institute, Volume 28, p. 1925-1932, 2000

[87] **Pischinger, R., Klell, M., Sams, Th.:** *Thermodynamik der Verbrennungskraftmaschine*, 2., überarbeitete Auflage, Springer Verlag, 2002

[88] **Pischinger, S., Geiger, J., Neff, W., Böwing, R., Thiemann, J., Koss, H.-J.:** *Einfluss von Zündung und Zylinderinnenströmung auf die ottomotorische Verbrennung bei hoher Ladungsverdünnung*, MTZ 63 (5), p. 388-399, 2002

[89] **Poulos, G., Heywood, J. B.:** *The Effect of Chamber Geometry on Spark-Ignition Engine Combustion*, SAE Paper 830334, 1983

[90] **Rahim, F., Elia, M., Ulinski, M., Metghalchi, M.:** *Burning velocity measurements of methane-oxygen-argon mixtures and an application to extend methane-air burning velocity measurements*, International Journal of Engine Reseach Volume 3, Number 2, p. 81-92, 2002

[91] **Rahmouni, C., Brecq, G., Tazerout, M., Le Corre, O.:** *Knock rating of gaseous fuels in a single cylinder spark ignition engine*, Fuel 83, p. 327-336, 2004

[92] **Rhodes, D., Keck, J.:** *Laminar Burning Speed Measurements of Indolene-Air-Diluent Mixtures at High Pressures and Temperatures*, SAE Paper 850047, 1985

[93] **Sakonji, T., Shoji, F.:** *Study on Improvement of Natural Gas Fueled Spark Ignition Engines - Effect of EGR Utilization*, SAE Paper 971714, 1997

[94] **Sazhin, S. S., E., Heikal, M., Marooney, C.:** *The Shell Autoignition Model: A New Mathematical Formulation*, Combustion and Flame 117, p. 529-540, 1999

[95] **Sazhina, E., Sazhin, S. , E., Heikal, M., Marooney, C.:** *The Shell autoignition model: application to gasoline and diesel fuels*, Fuel 78, p. 389-401, 1999

[96] **Schafer, A., Victor, D.:** *The future mobility of the world population*, Transportation Research Part A 34, p. 171-205, 2000

[97] **Schäpertöns, H., Lee, W.:** *Multidimensional Modelling of Knocking Combustion in SI Engines*, SAE Paper 850502, 1985

[98] **Schreiber, M., Sadat Sakak, A., Lingens, A.:** *A Reduced Thermokinetic Model for the Autoignition of Fuels with Variable Octane Ratings*, Twenty-Fifth Symposium (International) on Combustion, The Combustion Institute, p. 933-940, 1994

[99] **Schubiger, A., Boulouchos, K., Eberle, M.:** *Russbildung und Oxidation ber der dieselmotorischen Verbrennung*, MTZ 63 (5), 2002

[100] **Selim, M.:** *Sensitity of dual fuel engine combustion and knocking limits to gaseous fuel composition*, Energy Conversion and Management 45, p. 411-425, 2004

[101] **Soltic, P.:** *Part-Load Optimized SI Engine Systems*, Dissertation No 13942, ETH Zürich, 2000

[102] **Soylu, S., Van Gerpen, J.:** *Development of empirically based burning rate sub-models for a natural gas engine*, Energy Conversion and Management 45, p. 467-481, 2004

[103] **Soylu, S., Van Gerpen, J.:** *Development of an autoignition submodel for natural gas engines*, Fuel 82, p. 1699-1707, 2003

[104] **Soylu, S., Van Gerpen, J.:** *Fuel Effects on the Knocking Limit of a Heavy-Duty Natural Gas Engine*, SAE Paper 981401, 1998

[105] **Spadaccini, L., Colket, M.:** *Ignition Delay Characteristics of Methane Fuels*, Prog. Energy Combust Sci. Vol. 20, p. 431-460, 1994

[106] **Spicher, U., Kneifel, A., Rothe, M., Velji, A.:** *Methoden zur Erkennung und Analyse klopfender Verbrennung*, 1. Tagung Klopfregelung für Ottomotoren - Trends für Serienentwickler, 2003

[107] **Steiner, T., Boulouchos, K.:** *Near-Wall Unsteady Premixed Flame Propagation in S. I. Engines*, SAE Paper 951001, 1995

[108] **Stiebels, B.:** *Flammenausbreitung bei klopfender Verbrennung*, Fortschritt-Berichte VDI Reihe 12, Nr. 311, 1997

[109] **Sung, N., Song, J., Jeong, Y., Kim, Ch.:** *Flow Modeling for the Branched Intake Manifold Engine*, SAE Paper 960079, 1996

[110] **Syrimis, M., Assanis, D.:** *The Effect of the Location of Knock Initiation on Heat Flux Into an SI Combustion Chamber*, SAE Paper 972935, 1997

[111] **Tabaczynski, R., Ferguson, C., Radhakrishnan, K.:** *A Turbulent Entrainment Model for Spark-Ignition Engine Combustion*, SAE Paper 770647, 1977

[112] **Takagi, Y., Itoh, T., Lijima, T.:** *An Analytical Study on Knocking Heat Release and its Control in a Spark Ignition Engine*, SAE Paper 880196, 1988

[113] **The Mathworks, Inc.:** Matlab 7.1 - Documentation set, 2005

[114] **Thomas, J.-H., Dubuisson, B., Dillies-Peltier, M.-A.:** *Engine Knock Detection from Vibration Signals using Pattern Recognition*, Meccanica 32, p. 431-439, 1997

[115] **Veshagh, A., Chen, Ch.:** *A Simple Squish Model for Pentroof Combustion Chamber*, SAE Paper 911844, 1991

[116] **Warth, M., Obrecht, P., Bertola, A., Boulouchos, K.:** *Predictive Phenomenological C. I. Combustion Modeling - Optimization on the Basis of Bio-Inspired Algorithms*, SAE Paper 2005-01-1119, 2005

[117] **Warth, M., Obrecht, P., Boulouchos, K.:** *Vorausberechnung von Brennverlauf, No- und Russemissionen beim Dieselmotor - Optimierung und Validierung eines neuen Ansatzes*, 9. Tagung "Der Arbeitsprozess des Verbrennungsmotors", TU Graz, 2003

[118] **Wayne, W. S., Clark, N. N., Atkinson, Ch. M.:** *Numerical Prediction of Knock in a Bi-Fuel Engine*, SAE Paper 982533, 1998

[119] **Wayne, W. S., Clark, N. N., Atkinson, Ch. M.:** *A Parametric Study of Knock Control Strategies for a Bi-Fuel Engine*, SAE Paper 980895, 1998

[120] **Williams, F. A., Li, S. C.:** *Some Basic Considerations of Pollutant Emission and Knock in Internal Combustion Engines*, SAE Paper 2000-01-0647, 2000

[121] **Winkelhofer, E., Beidl, Ch., Hirsch, A., Piock, W.:** *Flammendiagnostik für die Leistungs- und Emissionsentwicklung*, MTZ 5, p. 362-369, 2004

[122] **Witt, A.:** *Analyse der thermodynamischen Verluste eines Ottomotors unter den Randbedingungen variabler Steuerzeiten*, Dissertation TU Graz, 1999

[123] **Witt, M., Griebel, P.:** *Numerische Untersuchung von laminaren Methan/Luft-Vormischflammen*, Interner Bericht, Paul Scherrer Institut, 2000

[124] **Worret, R.:** *Zylinderdruckbasierte Detektion und Simulation der Klopfgrenze mit einem verbesserten thermodynamischen Ansatz*, Dissertation TU Karlsruhe, 2002

[125] **Woschni, G., Anisitis, F.:** *Eine Methode zur Vorausberechnung der Änderung des Brennverlaufs mittelschnelllaufender Dieselmotoren bei geänderten Betriebsbedingungen*, MTZ 34 (4), p. 106-115, 1973

[126] **Zeilinger, K., Zitzler, G.:** *Vorausberechnung der Brennverläufe von Gasmotoren*, MTZ 64 (12), p. 1080-1089, 2003

[127] **Zeilinger, K., Zitzler, G.:** *Magerkonzept Gasmotoren - Entwicklung von Verfahren zur Vorausberechnung der Brennverläufe von Gasmotoren unter Berücksichtigung der Gasqualität und -zusammensetzung*, FVV Vorhaben Nr. 726, 2002

[128] **Zeldovich, Y. B.:** *Regime Classification of an Exothermic Reaction with Nonumiform Initial Conditions*, Combustion and Flame 39, p. 211-214, 1980

Appendix

A.1 Phenomenological Turbulence Model

The turbulence model has been built up using mean values (averaged over the entire combustion chamber) and no differentiation between burned and unburned zone has been applied.

For the turbulence production due to compression k_{comp} mass conservation for an eddy is assumed. This leads to

$$m = \rho \cdot V = \rho \cdot \frac{4}{3}\pi r^3 = const \rightarrow m \sim \rho \cdot d^3 = const \rightarrow d \sim \rho^{-1/3} \qquad \text{A.1.1}$$

Furthermore, conservation of angular momentum is assumed:

$$\frac{dD}{dt} = r \cdot F = r \cdot m \cdot \frac{dv}{dt} \rightarrow D = r \cdot m \cdot v = r \cdot m \cdot \omega \cdot r = m \cdot r^2 \cdot \omega \quad \text{A.1.2}$$

This means

$$m \cdot d^2 \cdot \omega = \rho V d^2 \omega = \rho \cdot \frac{4}{3}\pi \cdot \left(\frac{d}{2}\right)^3 \cdot d^2 \cdot \omega = const \qquad \text{A.1.3}$$

which leads to

$$\rho \cdot d^5 \cdot \omega = const \qquad \text{A.1.4}$$

The time one eddy needs to turn once can be approximated by

$$t_{Turn} = \frac{\pi \cdot d}{v} \approx \frac{\pi \cdot d}{u'} \qquad \text{A.1.5}$$

The rotary frequency can now be expressed by the time needed for one turn.

$$\omega \ = \ \frac{2\pi}{t_{Turn}} \ = \ \frac{2\pi \cdot u'}{\pi \cdot d} \sim \frac{u'}{d} \qquad\qquad \text{A.1.6}$$

By combining equation A.1.4 and A.1.6 the conservation of angular momentum can be written as

$$\rho \cdot d^5 \cdot \frac{u'}{d} \ = \ \rho \cdot d^4 \cdot u' = const \qquad\qquad \text{A.1.7}$$

Using equation 3.19, A.1.1 and A.1.7 the correlation between turbulent kinetic energy and density can be described as follows:

$$\rho^{-1/3} \cdot k^{1/2} \rightarrow k \sim \rho^{2/3} \qquad\qquad \text{A.1.8}$$

The production of turbulent kinetic energy due to compression can be derived from equation A.1.8 by logarithmise and taking the derivative.

$$\frac{dk_{comp}}{dt} \ = \ \frac{2}{3} k \cdot \frac{1}{\rho} \cdot \frac{d\rho}{dt} \qquad\qquad \text{A.1.9}$$

For the dissipation term it is assumed that one eddy dissipates within several turns. Using equation 3.19 and A.1.5 the change of kinetic energy can be described by

$$\frac{dk_{Diss}}{dt} \ = \ c_D \cdot \frac{u'^2 \cdot u'}{d} \ = \ c_D \cdot \frac{k^{3/2}}{l_I} \qquad\qquad \text{A.1.10}$$

For the squish-term a similar assumption is made. Therefore, the turbulence production due to the squish flow can be expressed as

$$\frac{dk_{squish}}{dt} \ = \ c_{sq} \cdot \frac{k_{sq}^{3/2}}{l_I} \qquad\qquad \text{A.1.11}$$

Here, c_D and c_{sq} were set to 0.09. For the determination of k_{sq} the radial and the axial velocities w_r and w_{ax} of the flow are considered [10] where a bowl-in piston combustion chamber design is assumed. The mass flow rate of the radial squish flow can be described as

$$\frac{dm_r}{dt} = \rho \, w_r A_{sq} \; and \; \frac{dm_r}{dt} = \frac{d}{dt}(\rho \cdot V_{sq}) = \rho \frac{dV_{sq}}{dt} + V_{sq}\frac{d\rho}{dt} \qquad \text{A.1.12}$$

leading to

$$w_r = \frac{1}{A_{sq}} \cdot \left[\frac{dV_{sq}}{dt} + \frac{V_{sq}}{\rho} \cdot \frac{d\rho}{dt}\right] \qquad \text{A.1.13}$$

If V_{sq} is replaced by $V_{sq}=A_r x_{pist}$ - where x_{pist} describes the piston position - the radial velocity can be written as

$$w_r = \frac{A_r}{A_{sq}} \cdot \left(\frac{dx_{pist}}{dt} + \frac{x_{pist}}{\rho} \cdot \frac{d\rho}{dt}\right) \qquad \text{A.1.14}$$
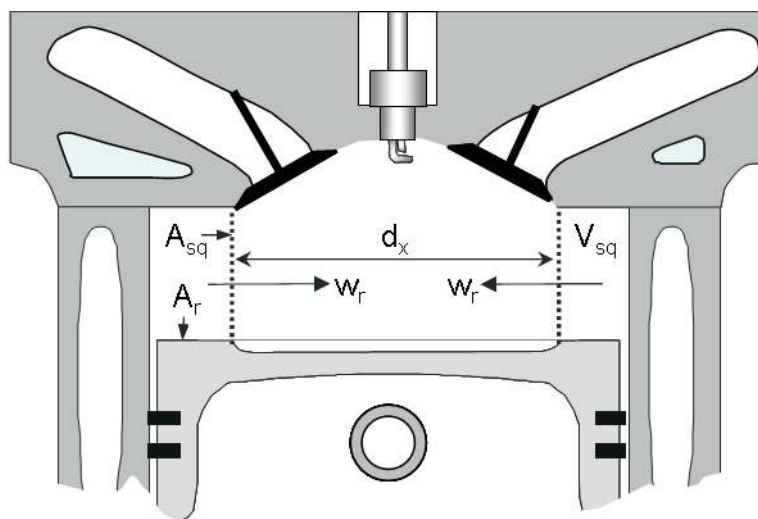
The following figure shows the radial velocity

Figure A.1: Defining the radial velocity of the squish flow

In the present engine the radial velocity will be small due to the small area A_r. The assumption of a bowl-in piston combustion chamber leads to further simplifications

$$w_r = \frac{B^2 - d^2_x}{4 \cdot d_x \cdot x_{pist}} \cdot \left(\frac{dx_{pist}}{dt} + \frac{x_{pist}}{\rho} \cdot \frac{d\rho}{dt}\right) \qquad \text{A.1.15}$$

where B is the bore of the engine.

For the derivation of the axial velocity it is assumed that there is one global velocity representing the global axial flow behaviour.
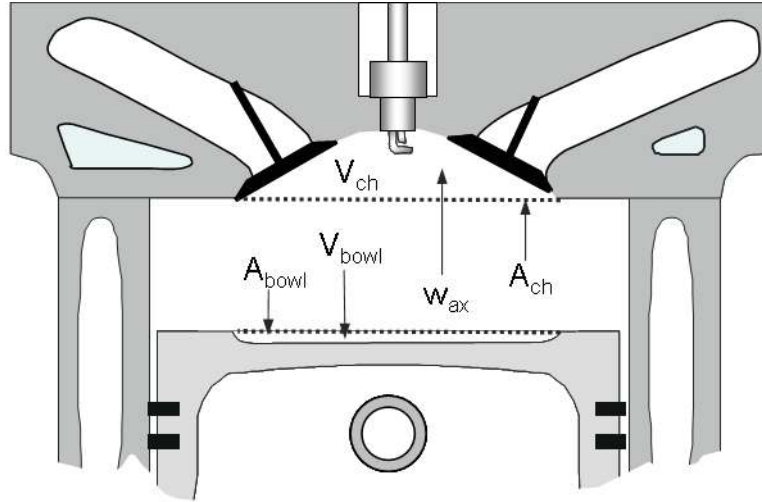

Figure A.2: Defining the axial velocity of the squish flow

Therefore, the axial velocity can be described as

$$\frac{dm_{ax}}{dt} = -\frac{dm_{bowl}}{dt} - \frac{dm_{ch}}{dt} \ and \ \frac{dm_{ax}}{dt} = \rho \cdot w_{ax} \cdot (A_{bowl} + A_{ch}) \qquad \text{A.1.16}$$

where the mass flow rate to the bowl dm_{bowl}/dt and the mass flow rate to the cylinder head dm_{ch}/dt are considered. By analysing the second part of equation A.1.16 it can be seen, that a simplification was made in the handling of the areas of the bowl A_{bowl} and the cylinder head A_{ch}, respectively. In this formulation an extended cylinder head area - or an extended bowl area - is assumed. After introducing

$$\frac{dm_{bowl}}{dt} = V_{bowl} \cdot \frac{d\rho}{dt} \ and \ \frac{dm_{ch}}{dt} = V_{ch} \cdot \frac{d\rho}{dt} \qquad \text{A.1.17}$$

the combination with equation A.1.16 leads to the the axial velocity

$$w_{ax} = -\frac{1}{\rho} \cdot \frac{d\rho}{dt} \cdot \left[\frac{V_{bowl} + V_{ch}}{A_{bowl} + A_{ch}}\right] \qquad \text{A.1.18}$$

The mean velocity due to the squish flow w_{sq} can be defined by the volumetric average of the radial and the axial velocity. A frustum defined by w_r and a cone defined by $(w_r - w_{ax})$ are considered.
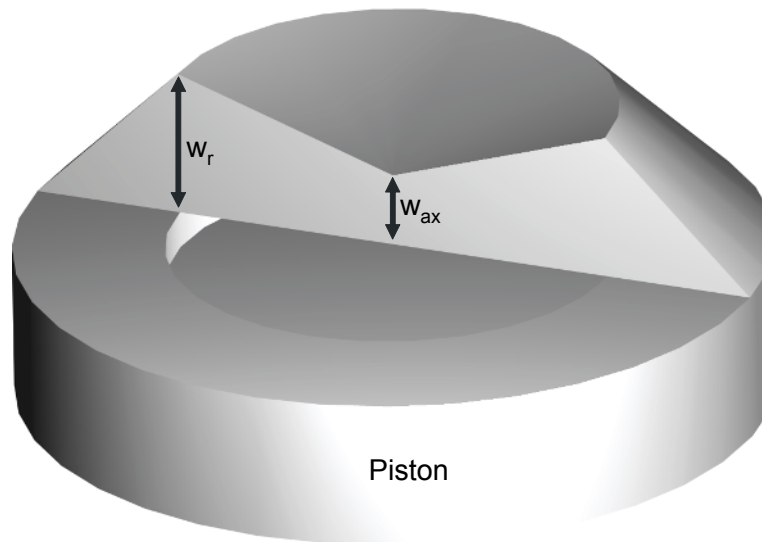

Figure A.3: Determination of the mean squish flow velocity based on the radial and the axial velocities of the squish flow

The volumes can be expressed as

$$V_{frustum} = \frac{\pi \cdot w_r}{3} \cdot ((B/2)^2 + (d_x/2) \cdot (B/2) + (d_x/2)^2)$$

$$V_{cone} = \frac{\pi \cdot (d_x/2)}{3} \cdot (w_r - w_{ax})$$

A.1.19

The mean squish velocity w_{sq} and the turbulent kinetic energy due to the squish flow k_{sq} result, if the volume $V = V_{frustum} - V_{cone}$ is divided by the area of the bore

$$w_{sq} = \frac{1}{3} \cdot \left[w_r \left(1 + \frac{d_x}{B} \right) + w_{ax} \left(\frac{d_x}{B} \right)^2 \right]$$

and

$$k_{sq} = \frac{1}{2} w_{sq}^{\ 2}$$

A.1.20

Finally, the turbulence production due to the intake flow has to be described. The kinetic energy of a moving part and its derivative with respect to time are defined by

$$E_{kin} = \frac{1}{2} m v^2 \ and \ \frac{dE_{kin}}{dt} = \frac{1}{2} \cdot \left(v^2 \cdot \frac{dm}{dt} + 2vm \cdot \frac{dv}{dt} \right) \qquad \text{A.1.21}$$

The second part in equation A.1.21 can be neglected. By dividing dE_{kin}/dt by the cylinder mass m_{cyl} and replacing v by v_{intake} the turbulent kinetic energy of the intake flow can be obtained

$$\frac{dk_{in}}{dt} = K_{in} \cdot \frac{v_{intake}^2}{m_{cyl}} \cdot \frac{dm_{intake}}{dt} \qquad \text{A.1.22}$$

with $K_{in} = 8 \cdot 10^{-4}$. For the determination of the flame front area based on experimentally determined burn rate curves the initial turbulence intensity k_{ivc} must be estimated because $m_{intake}=0$ (closed combustion chamber system).

$$k_{ivc} = K_{kivc} \cdot v_{intake}^2 \qquad \text{A.1.23}$$

with: $K_{kivc}=0.2$=constant and v_{intake}=mean intake velocity.

The mean intake mass flow rate from inlet valve open (ivo) to inlet valve close (ivc) can be estimated as

$$\dot{m}_{intake} = \frac{m_{cyl}}{\Delta t_{valve}} = \frac{\dot{m}_{totengine} \cdot 2}{z_{cylinder} \cdot n_{engine} \cdot \Delta t_{valve}} = \frac{\dot{m}_{totengine} \cdot 720}{z_{cylinder} \cdot \Delta \varphi_{valve}} \qquad \text{A.1.24}$$

where: m_{cyl}=total cylinder mass at ivc, $\dot{m}_{totengine} = \dot{m}_{air} + \dot{m}_{fuel} + \dot{m}_{egr}$=total mass flow rate, $\Delta t_{valve}=t_{ivc}-t_{ivo}$, $\Delta \varphi_{valve}=\varphi_{ivc}-\varphi_{ivo}$, $z_{cylinder}$=number of cylinders

Thus, the mean intake velocity can now be derived

$$\dot{m}_{intake} = \rho_{intake} v_{intake} A_{valve} \rightarrow v_{intake} = \frac{\dot{m}_{totengine} \cdot R_{intake} \cdot T_{intake} \cdot 720}{z_{cylinder} \cdot p_{intake} \cdot A_{valve} \cdot \Delta \varphi_{valve}} \qquad \text{A.1.25}$$

With: $R_{intake}, T_{intake}, p_{intake}$: Gas constant, temperature and pressure in the intake manifold, A_{valve}=Flow area through the valve

## A.2 Selected Operating Points to Test the Combustion Models

The following table gives on overview over the 30 operating points chosen to evaluate the combustion models for ε=13.5. The first ten operating points are without EGR where operating points eleven to thirty are with EGR.

Operating point	Engine speed [rpm]	BMEP [bar]	Spark timing [° BTDC]	EGR rate [%]
1	1000	2	13	0
2	1000	3	21.75	0
3	1500	1	36	0
4	2000	2	26.25	0
5	2000	2	40.5	0
6	2000	7	27.75	0
7	2500	1	39.75	0
8	3000	1	41.25	0
9	3000	7	30.75	0
10	3000	8.64 (FL)	29.25	0
11	1500	2	45	10.9
12	1500	3	40.5	11.5
13	1500	4	34.5	9.1
14	1500	5	31.5	7.3
15	2000	2	45.75	10.7
16	2000	3	46.5	10.8
17	2000	4	36.75	11
18	2000	5	36	9
19	2000	6	34.5	8.4
20	3000	2	54.75	8.7
21	3000	3	42	8.9

Operating point	Engine speed [rpm]	BMEP [bar]	Spark timing [° BTDC]	EGR rate [%]
22	3000	4	42.75	9.1
23	3000	5	39	9.7
24	3000	6	36.75	8
25	4000	2	57	8.2
26	4000	3	46.5	10.6
27	4000	4	45	11.5
28	4000	5	42	9.5
29	4000	6	39	8
30	4000	7	34.5	6.1

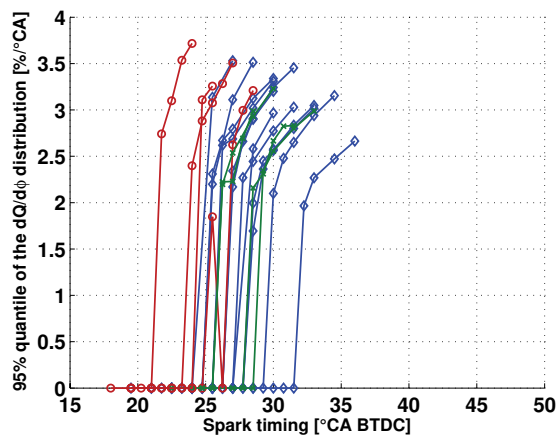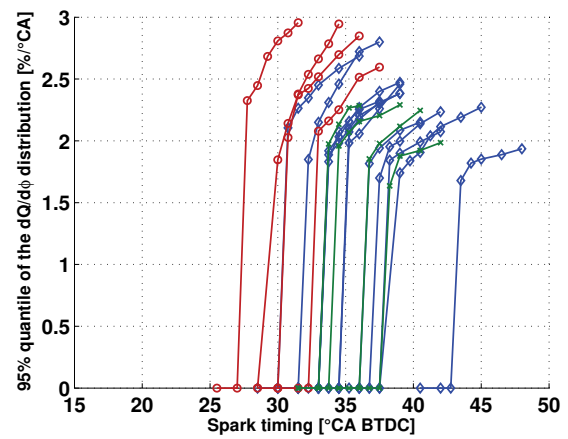# A.3 Evaluation of the Knock Detection Method for all Gas Compositions
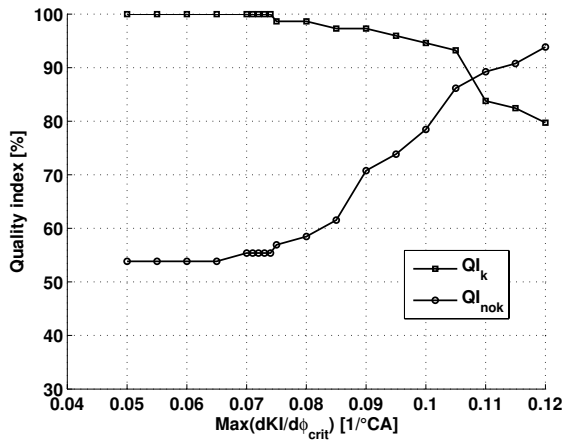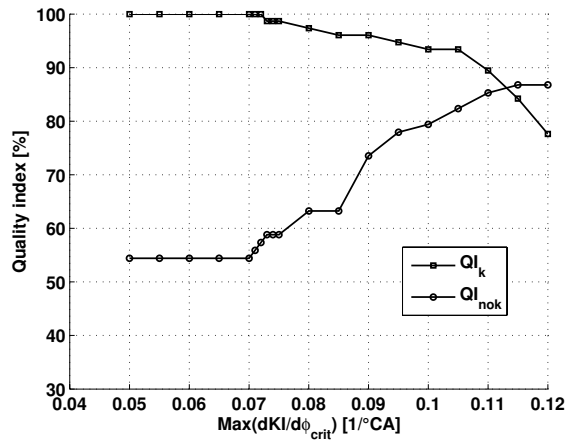
G4E
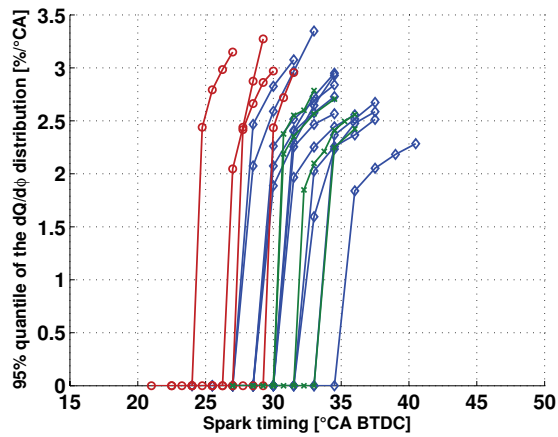
G8E
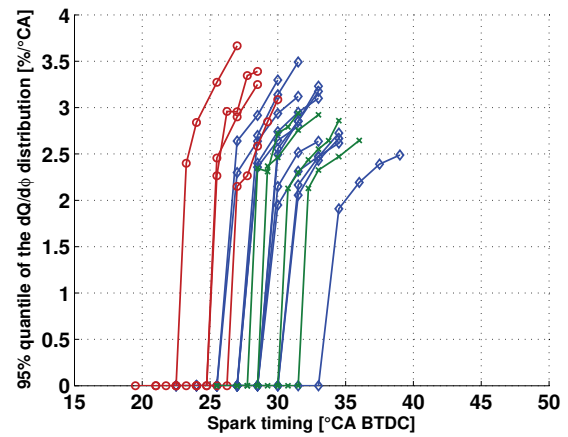
G44

G25
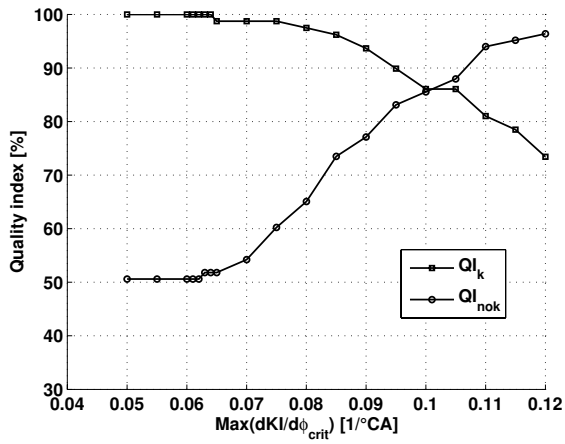
A.4 Quality Index for all Gas Compositions

G4E
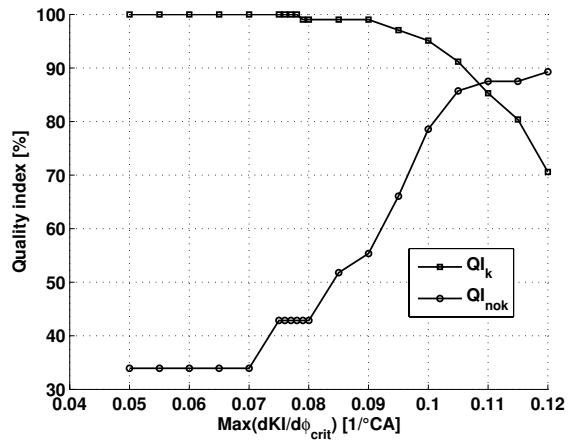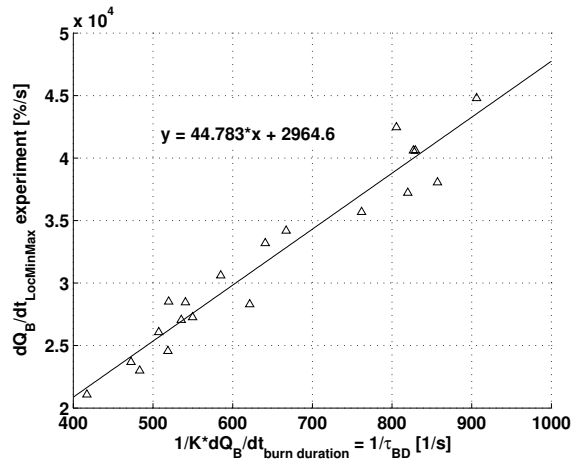

G8E

G44

G25

A.5   Knock Intensity Estimation for all Gas Compositions

G4E

G8E
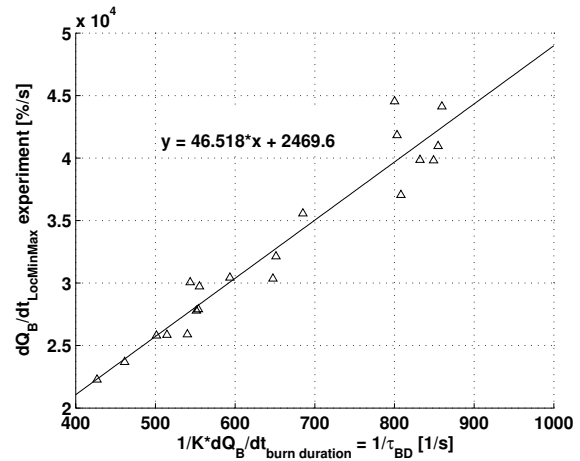
G44
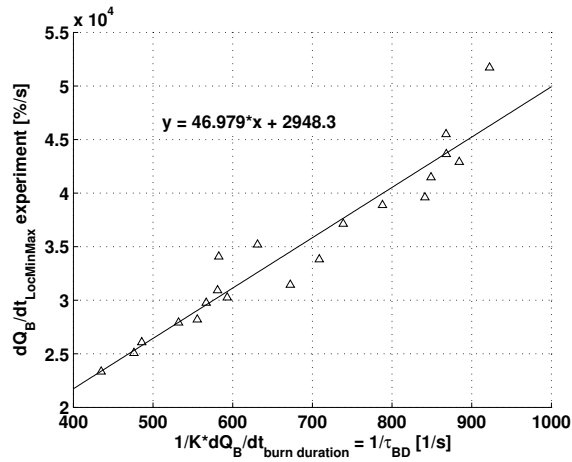
G25
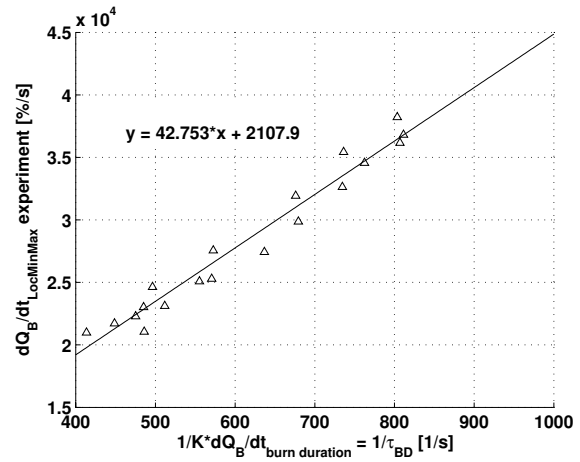
Nomenclature

Symbols

A_F	[m^2]	flame front area, parameter
A	[-]	Parameter
a	[-]	constant
AF	[-]	air-fuel ratio
B	[m]	bore
bmep	[bar]	brake mean effective pressure
c_i	[mol/m^3]	concentration of species i
cp	[J/kgK]	specific heat at constant pressure
cv	[J/kgK]	specific heat at constant volume
Ex	[-]	expansion factor
f	[-]	conversion function (ignition delay)
g	[-]	conversion function (burn duration)
h	[-], [mm]	conversion function (shape parameter), height
H	[J]	enthalpy, heating value
K	[-]	Constant
k	[m2/s2]	turbulent kinetic energy
KI	[-]	knock integral
l_i	[m]	integral length scale
m	[kg],[-]	mass, exponent
M	[kg/kmol]	Molecular weight

m_V	[-]	shape parameter
n	[rpm], [-]	engine speed, rounds per minute, exponent
p	[Pa]	pressure
Q	[J]	heat
r	[m]	radius
R	[J/kgK]	gas constant
s	[m/s]	flame speed, speed
S	[m]	stroke
T	[K]	temperature
t	[s]	time
TA	[K]	activation temperature
u	[J/kg]	specific internal energy
U	[J]	internal energy
u'	[m/s]	turbulence intensity
V	[m³]	volume
W	[J]	work
x	[-]	mass fraction, combustion progress variable

Greek Symbols

α	[-]	pressure exponent
β	[-]	exponent for combustion progress
δ	[m]	distance
ε	[-]	compression ratio
ϕ	[°]	crank angle
Φ	[-]	equivalence ratio
η	[Pa-s]	dynamic viscosity
η_e	[-]	efficiency
κ	[-]	ratio of specific heats
λ	[-]	excess air ratio
ρ	[kg/m³]	density
τ_{reac}	[s]	characteristic reaction time

Indices

B	burned
BL	boundary layer
CAKnock	crank angle of knock occurrence
Corr	correction
crit	critical
cyl	cylinder
disc	disc shaped flame
E	end
F	flame, fuel

FW	flame-wall
G	Gülder
i	component
k	number of species
L	laminar, low
l_i	integral length scale
LocMax	local maximum
LocMin	local minimum
Max	maximum
mean	mean value, mean curve
n	net
rg	residual gas
sphere	spherically shaped flame
S	start
st	spark timing
ST	stoichiometric, turbulent flame speed
T	turbulent
tot	total
U	unburned
Vol	volume
x	x-direction
y	y-direction
z	z-direction
0	reference
10.7	compression ratio 10.7
13.5	compression ratio 13.5

Abbreviations

ACEA	European Automobile Manufacturers Association
ATDC	After Top Dead Centre
BD	Burn Duration
BFE	Swiss Federal Office of Energy (Bundesamt für Energie)
BSFC	Brake Specific Fuel Consumption
BTDC	Before Top Dead Centre
C_2H_6	ethane
C_3H_8	propane
CA	Crank Angle
CEV	Clean Engine Vehicle
CH_4	methane
CNG	Compressed Natural Gas
CFRD	Computational Reactive Fluid Dynamics
DVGW	German Technical and Scientific Association for Gas and Water (Deutsche Vereinigung des Gas- und Wasserfaches e. V.)
ECU	Engine Control Unit
EGR	Exhaust Gas Recirculation
EMPA	Swiss Federal Laboratories for Materials Testing and Research (Eidgenössische Materialprüfungs- und Forschungsanstalt)
ETH	Swiss Federal Institut of Technology Zurich (Eidgenössische Technische Hochschule Zürich)
FL	Full Load
G20	Gas quality: 100% Methane
G4E	Gas quality: 96% methane, 4% ethane

G8E	Gas quality: 92% methane, 8% ethane
G44	Gas quality: 92% methane, 4% ethane, 4% propane
G25	Gas quality: 86% methane, 14% nitrogen
ID	Ignition Delay
IVC	Inlet Valve Close
LAV	Aerothermochemistry and Combustion Systems Laboratory (Laboratorium für Aerothermochemie und Verbrenungssyseme)
N_2	nitrogen
NECD	New European Driving Cycle
ÖVGW	Austrian Gas and Water Industry Association (Österreichischen Vereinigung für das Gas- und Wasserfach)
R&D	Research and Development
ST	Spark Timing
SULEV	Super-Ultra-Low-Emission-Vehicle
SVGW	Swiss Gas and Water Industry Association (Schweizerischer Verein des Gas- und Wasserfaches)
TC	Turbocharger
TDC	Top Dead Centre
VW	Volkswagen
WEG	Wärmeentwicklungsgesetz
2D	two dimensional
3D	three dimensional

Curriculum Vitae

Personal Data

Name	Christian Lämmle
Date of birth	21. November 1974
Place of birth	St. Gallen, Switzerland

Education

1981-1987	Primary school in Uster and Russikon, Switzerland
1987-1989	Secondary school in Russikon, Switzerland
1989-1994	Kantonsschule Zürcher Oberland in Wetzikon, Matura type C
1994-2000	Studies in Mechanical Engineering, Swiss Federal Institut of Technology (ETH), Zurich, Switzerland
2000-2005	Doctoral student and assistant at the Swiss Federal Laboratories for Materials Testing and Research, EMPA Dübendorf, and the Institut of Energy Technology, Aerothermochemistry and Combustion Systems Laboratory (LAV), ETH Zurich
March - November 2005	50. St. Galler Management Seminar, University of St. Gallen

Professional

June - September 1994	PANOLIN AG, Madetswil, Switzerland High Tech Lubricants, Various Jobs
March - April 1995	Huber+Suhner AG, Pfäffikon, Switzerland Workshop practice
March - August 1998	Porsche AG, Weissach, Germany Engine development group
March 1996 - March 1997, and winter semester 98/99,	Centre of Product-Development, ETH Zurich, Virtual Reality, Materials and Process Technologies
2000-2005	Doctoral student and assistant, EMPA Dübendorf and LAV, ETH Zurich